Université d'Ottawa • University of Ottawa

Optical Properties of GaAs-based Self-Assembled Quantum Dots and Quantum Dot Lasers

by
Karin Hinzer

Thesis submitted to the Faculty of Graduate and Postdoctoral Studies
in partial fulfillment of the requirements for the degree of
Doctor of Philosophy

Department of Physics
University of Ottawa
Ottawa-Carleton Institute for Physics
Ottawa, Canada
2001

Abstract

Three-dimensional confinement of carriers eliminates the problem of thermal spreading of carriers observed in higher-dimensional systems. Uniform self-assembled quantum dots (QDs) are obtained using the spontaneous islanding of highly strained III-V semiconductors grown with standard epitaxy. Visible stimulated emission has been obtained with red-emitting AlInAs QDs in AlGaAs barriers. Continuous (CW) threshold current densities below $100A/cm^2$ have been measured at low temperatures and QD material gain larger than 1.7×10^4 cm^{-1} demonstrate good material quality. Room temperature lasing has also been observed for higher threshold current densities.

For longer wavelengths where the thermionic emission problem is less important, InAs/GaAs lasers can operate at room temperature for current densities below $\sim 100A/cm^2$ for wavelengths around 950 nm. The zero-dimensional transitions between confined electrons and holes in artificial atoms allow the observation of state-filling at relatively low level of material excitation. Lasing is observed in the upper QD shells for small gain media, and progress towards the QD ground states for longer cavity lengths. Gain may also be increased by including multiple layers of QDs in the active region.

To understand the shell structure of AlInAs/AlGaAs QDs, we present results of interband spectroscopy of single $Al_{0.36}In_{0.64}As/Al_{0.33}Ga_{0.67}As$ self-assembled QDs. The single dot spectroscopy has been carried out at low temperature as a function of the excitation power and magnetic field up to 8 T. The emission spectra as a function of excitation power show two distinct groups of transitions which we associate with the recombination from ground and excited QD levels with a spacing of ~70 meV. The

application of magnetic field allows to identify the exciton emission as well as the emission from the bi-exciton, and charged exciton complexes with binding energies of ~5 meV. The binding energies compare favorably with results of calculations.

Artificial molecules are studied using coupled QD ensembles and single QD spectroscopy. The coupling between the zero-dimensional states is varied by changing the distance between two layers of stacked InAs/GaAs QDs. Energy level splitting larger than 30 meV of the symmetric and anti-symmetric states of the lowest confined shell are measured and are compared to theory.

À Bruno

Statement of Originality

Except where otherwise stated, the results presented in this thesis were obtained by the author during the period of her Ph. D. research project under the supervision of Dr. S. Fafard and the co-supervision of Dr. S. Charbonneau. They are to the best of her knowledge original. These include:

1. Gain and wavelength tuning measurements of AlInAs/AlGaAs QD laser.
2. Spectroscopy of QDs on AlInAs/AlGaAs QD lasers.
3. Wavelength tuning measurements of InAs/GaAs QD lasers at T = 77 K and 300 K.
4. Spectroscopy of single AlInAs/AlGaAs and InAs/GaAs QDs.
5. Spectroscopy of single pairs of coupled InAs/GaAs QDs.

All samples were produced by Dr. S. Fafard at the Institute for Microstructural Sciences, National Research Council, except for some of the AlInAs/AlGaAs QD laser samples which were produced by Dr. A. J. SpringThorpe, Nortel Networks. Single QD measurements of mesa samples where performed in a visit at Dr. M. Bayer's lab, Würzburg Universität, Germany. The mesas and their SEM micrographs were produced by M. Emmerling, Würzburg Universität. The metal masks and their SEM micrographs were produced by Dr. J. Lapointe, National Research Council. The cross-sectional TEM micrographs of AlInAs/AlGaAs QD laser samples were produced by Dr. E. M. Griswold, Nortel Networks. The cross-sectional TEM micrographs of the coupled InAs/GaAs QDs

were produced by Dr. J. P. McCaffrey, National Research Council. Laser samples were processed by Dr. Y. Feng, National Research Council. Modeling of the single QD emission and coupled QD splitting was done by Dr. P. Hawrylak and M. Korkusinski.

- The above work has led to the following papers:

1. K. Hinzer, P. Hawrylak, M. Korkusinski, S. Fafard, M. Bayer, O. Stern, A. Gorbunov, and A. Forchel, "Optical Spectroscopy of a single AlInAs/AlGaAs quantum dot", Phys. Rev. B **63**, 075314 (2001).

2. K. Hinzer, M. Bayer, J. P. McCaffrey, P. Hawrylak, M. Korkusinski, O. Stern, Z. R. Wasilewski, S. Fafard, and A. Forchel, "Optical spectroscopy of electronic states in a single pair of vertically coupled self-assembled quantum dots," Phys. Status Sol. (b) **224**, 385 (2001).

3. M. Bayer, P. Hawrylak, K. Hinzer, S. Fafard, M. Korkusinski, Z. R. Wasilewski, O. Stern, and A. Forchel, "Coupling and entangling of quantum states in quantum dot molecules," Science **297**, 451 (2001).

4. K. Hinzer, J. Lapointe, Y. Feng, A. J. SpringThorpe, and S. Fafard, "Photoluminescence mapping of single InAlAs/AlGaAs quantum dots in laser structures," Mat. Res. Soc. Symp. Proc. **642**, J5.6.1 (2001).

5. K. Hinzer, P. Hawrylak, M. Korkusinski, J. P. McCaffrey, Z. R. Wasilewski, S. Fafard, M. Bayer, O. Stern, and A. Forchel, "Spectroscopy and electronic states of coupled InAs/GaAs quantum dots with well-defined electronic shells," Proc. 25th Int. Conf. Phys. Semicond. 1169 (2001).

6. K. Hinzer, P. Hawrylak, J. Lapointe, J. P. McCaffrey, S. Fafard, M. Bayer, O. Stern, and A. Forchel, "Spectroscopy of single AlInAs self-assembled quantum dots in an AlGaAs matrix," Physics in Canada **56**, 191 (2000).

7. K. Hinzer, M. Bayer, O. Stern, A. Gorbunov, A. Forchel, P. Hawrylak, J. Lapointe, and S. Fafard, "Single dot spectroscopy of multi-excitons in AlInAs/AlGaAs quantum dots," Proc. of SPIE **4087**, 559 (2000).

8. K. Hinzer, J. Lapointe, Y. Feng, A. Delâge, S. Fafard, A. J. SpringThorpe, E. M. Griswold, "Short-wavelength laser diodes based on AlInAs/AlGaAs self-assembled quantum dots," J. Appl. Phys. **87**, 1496 (2000).

9. K. Hinzer, C. Ni Allen, J. Lapointe, D. Picard, Z. R. Wasilewski, A. J. SpringThorpe, S. Fafard, "Widely tunable self-assembled quantum dot lasers," J. Vac. Sci. Technol. A **18**, 578 (2000).

10. S. Fafard, H. C. Liu Z.R. Wasilewski, J. McCaffrey, M. Spanner, S. Raymond, C. Ni. Allen, K. Hinzer, J. Lapointe, C. Struby, M. Gao, P. Hawrylak, C. Gould, A. Sachrajda, P. Zawadzki, "Quantum Dot Devices," Proc. of SPIE **4078**, 100 (2000).

11. S. Raymond, K. Hinzer, S. Fafard, J. L. Merz, "Experimental determination of Auger capture coefficients in self-assembled quantum dots," Phys. Rev. B **61**, R16331 (2000).

12. S. Raymond, S. Fafard, K. Hinzer, S. Charbonneau, and J. L. Merz, "Temporal cross-section for carrier capture by self-assembled quantum dots," Microelectronic Engineering **53**, 241 (2000).

13. S. Fafard, Z. R. Wasilewski, C. Ni. Allen, K. Hinzer, J. P. McCaffrey, Y. Feng, "Lasing in quantum dot ensemble with sharp adjustable electronic shells," Appl. Phys. Lett. **75**, 986 (1999).

- Portions of the results in this thesis were presented in the following conferences:

1. K. Hinzer, "Spectroscopie de multi-excitons dans les points quantiques simples et dans les points quantiques couplés," oral presentation at the *69e congrès de l'Acfas*, Sherbrooke, Québec (2001).

2. K. Hinzer, Optical spectroscopy of single quantum dots, oral presentation at the Ottawa Carleton Institute for Physics Fall Graduate Student Seminar Day, Ottawa (2000).

3. K. Hinzer, M. Bayer, O. Stern, A. Gorbunov, A. Forchel, P. Hawrylak, J. Lapointe, Z. R. Wasilewski, S. Fafard. Spectroscopy of multi-excitons in single AlInAs/AlGaAs quantum dots, oral presentation at the *Fall Material Research Society* meeting, Boston (2000).

4. K. Hinzer, Self-assembled quantum dots, IMS lunch-time talks, Ottawa (2000).

5. K. Hinzer, P. Hawrylak, J. P. McCaffrey, S. Fafard, M. Bayer, O. Stern, A. Forchel. Spectroscopy of Vertically Coupled Self-Assembled Quantum Dots, oral presentation at *Photonics North ICAPT 2000*, Quebec City (2000).

6. K. Hinzer, P. Hawrylak, J. Lapointe, J. P. McCaffrey, S. Fafard, M. Bayer, O. Stern, A. Forchel. Spectroscopy of Single Self-Assembled Quantum Dots, oral presentation at the *Canadian Association of Physicists Congress*, Toronto (2000).

7. K. Hinzer, P. Hawrylak, J. P. McCaffrey, S. Fafard, M. Bayer, O. Stern, A. Forchel. Single dot spectroscopy of self-assembled quantum dots, poster presentation at the *11th International Winterschool on New Developments in Solid State Physics; Low-Dimensional Systems: Fundamentals and Applications*, Mauterndorf, Austria (2000).

8. K. Hinzer, S. Fafard, C. Ni. Allen, J. P. McCaffrey, J. Lapointe, Y. Feng, A. J. SpringThorpe, E. M. Griswold. Gain and lasing in several electronic shells in self-

assembled quantum dot lasers, presentation at the *Ninth Canadian Semiconductor Technology* (1999).

9. K. Hinzer, S. Fafard, F. Yang, C. Nì Allen, J. Lapointe, Y. Feng, J. McCaffrey, S. Charbonneau, A. J. SpringThorpe, E. M. Griswold. "Propriétés optiques de lasers semi-conducteurs à points quantiques auto-assemblés," oral presentation at the *67e congrès de l'Acfas*, Ottawa (1999).

- Contributions not directly related to this thesis:

1. B. J. Riel, K. Hinzer, S. Moisa, J. Fraser, K. St-Jean, P.Piercy, S. Fafard, and Z. Wasilewski, "Tuning self-assembled quantum dots using the arsenic pressure," *submitted 2001*.

Part of this work has been carried out under the Canadian European Research Initiative on Nanostructures supported by IMS, NRC, NSERC, and EC. I would like to thank NSERC and FCAR for financial support.

Acknowledgements

I would like to extend my deepest appreciation to my supervisor Dr. Simon Fafard, for his unfailing enthusiasm towards our research and his guidance all along the project. I thank him for the chance to work on such an interesting project, the tremendous help in the lab, the many discussions and also for all the samples he grew. I would also like to thank my co-supervisor Dr. Sylvain Charbonneau for his expert advice. I am grateful for the financial support that enabled me to engage in collaborations with other researchers and attend conferences.

I would like to thank Dr. Manfred Bayer and Dr. Alfred Forchel from Universität Würzburg for the opportunity of performing single QD photoluminescence in their group and for some financial support for the trip. I would like to thank Manfred Bayer, Omar Stern and Sasha Gorbunov for performing some of the single QD measurements together in addition to all their help and friendship during my stays in Würzburg.

On the theoretical side, I am grateful to Dr. Pawel Hawrylak for all his insight on low-dimensional systems. As well, I thank him and Marek Korkusinski for the single and coupled QD calculations.

I am grateful to Dr. Sylvain Raymond for all the help during my graduate studies, especially with the time-resolved experiments. I have received ongoing support from Dr. Jean Lapointe, Dr. Yan Feng, and a large part of the IMS-Microfabrication group in laser

processing. I thank Dr. John McCaffrey for the TEM micrographs essential for sample characterization. I am also grateful to André Delage for his help with waveguide analysis.

For the InAlAs/AlGaAs quantum dot lasers, I benefited from Dr. Tony SpringThorpe's sample growth and Dr. Ellen Griswold's TEM micrographs, who are both from Nortel Networks.

Thanks to the many students I shared office or lab space with at M-23a for all the great times: Joan, Paul, Claudine, Sunida, Jamie, and Murray.

Finally, I would like to thank Bruno for his immense support and both of our families for their encouragement over the past years.

Table of Contents

List of Figures

List of Tables

List of Abbreviations

CCD	Charged coupled device
CW	Continuous wave
DOS	Density of states
EL	Electroluminescence
FWHM	Full width at half maximum
I_{exc}	Excitation intensity
J_{th}	Threshold current density
MBE	Molecular beam epitaxy
ML	Monolayer
PL	Photoluminescence
PV	Photovoltage
QD	Quantum dot
QW	Quantum well
RIE	Reactive ion etching
SEM	Scanning electron microscope
SIMS	Secondary ion mass spectroscopy
TEM	Transmission electron microscopy
WL	Wetting layer

Chapter 1

Introduction

The energy band in a semiconductor crystal results from the periodic structure of an infinite lattice. When the crystal thickness is finite and thin enough to be comparable with the de Broglie wavelength of an electron in a semiconductor (≈ 10 nm), one obtains a structure with carriers confined in one-dimension known as a quantum well (QW). Perpendicular to the well plane (z-direction), electrons are confined by the potential well created by the double heterostructure, resulting in a structure having discrete quantized energy levels. Along the well plane (x-y plane), the crystal is assumed infinite. The density of states (DOS) of carriers in the QW is modified from the conventional $E^{1/2}$-dependence for bulk materials to a step-like dependence.[1] Such lower dimensional structures can be used as the active region of semiconductor lasers. It was first predicted theoretically, and subsequently confirmed experimentally, that this reduction in dimensionality of the active region results in superior lasing characteristics including lower threshold currents and improved temperature stability. Today, semiconductor laser diodes based on QWs are the key components in optoelectronic and photonic integrated circuits, and play an essential role in the expanding information technology and communication industry.[2] They are used in a wide range of applications from optical

fiber communication systems to barcode scanning, including optical storage, image recording, and displays for entertainment and instrumentation. These devices are capable of high powers and efficiencies at a variety of wavelengths in the visible and the infrared.

By increasing the confinement of carriers in the other directions (x and y), systems with lower dimensions can be obtained: quantum wires and quantum dots (QDs), in which carrier motion is confined to one and zero dimension respectively. Because of the 3D-quantum confinement, the energy spectra of electrons and holes in QDs can be considered discrete. This delta-function-like DOS of QD systems leads to an effective absence of carrier thermal distribution, independent of temperature, in contrast to QW and bulk structures. The main expected advantage in introducing QDs as the active medium of a semiconductor laser over conventional QW lasers is a lowering in threshold current density due to the discrete nature of the DOS.[3] Other predicted advantages include: higher modulation speed, reduced temperature sensitivity, higher optical gain, and wider spectral gain profiles.[3,4,5,6]

Prior to 1994, only one research group had reported light emission from QDs through current injection,[7] using standard lithographic techniques for the fabrication of QDs. An important advance in the fabrication of zero dimensional structures exploits one of the natural consequences in growth modes for dissimilar materials. Self-assembled QDs obtained in the Stranski-Krastanow growth mode made a breakthrough for nanostructures in 1993.[8] QDs grown in this manner are defect-free and make use of a mature epitaxy growth process without requiring any additional processing. As well, their ability to emit at a range of wavelengths by simply using the various well understood and characterized III-V alloy systems, make them ideal for basic physics studies, as well as for

immediate integration into practical devices. The samples characterized in this study were grown using this fabrication technique.

It is now possible to fabricate QD lasers with good performances.[9,10,11,12,13,14,15,16,17,18,19,20,21,22] Most studies so far concentrated on material systems such as InAs/GaAs and InGaAs/GaAs with emission in the infrared. For applications requiring visible emission such as higher-density optical storage, or display and illumination sources shorter wavelength systems[23,24,25,26] such as red-emitting AlInAs QDs imbedded in an AlGaAs matrix are desired.

The AlInAs/AlGaAs QD system features a variety of interesting characteristics of zero-dimensional systems such as extremely sharp homogeneous linewidths,[27] invariant linewidths and lifetimes for temperatures up to the onset of thermionic emission,[28] state-filling and excited-state emission,[9] and distinctive carrier dynamics and phonon interactions.[29] Typical emission spectra from a self-assembled QD ensemble has a Gaussian distribution line shape at low excitation intensity caused by small variations in the parameters of the different QDs probed, such as size, composition, and strain. AlInAs QDs often display a relatively large inhomogeneous broadening in their emission spectrum. This effect and/or an ensemble too dense to support clear zero-dimensional states caused by strain interactions or lateral coupling leads to a lack of well-defined excited states causing ambiguity in identifying which levels are contributing to the stimulated emission. This ambiguity is usually accentuated when using multiple stacked layers to increase the gain in the active region. Chapter 4 will present results of properties specific to QD lasers such as wavelength tuning and broadband lasing, as well as gain measurements. In order to understand the QD energy level structure in this ternary alloy,

we show photoluminescence (PL) spectra and imaging of specific QD by probing the facet of a QD laser structure using a sub-micron sized laser beam.

Chapter 4 also presents results for InAs/GaAs QD lasers. With the proper growth conditions, quantized electron and hole energy levels of QDs are clearly visible in the emission spectra from large ensembles as a function of excitation power, and hence, increasing the population of carriers.[29,30,31,32,33,34,35] It has been recently demonstrated that self-assembled growth can be controlled to fabricate QD structures with well-defined excited-state transitions, and to manipulate their energy levels to tailor the number of confined states and their intersublevel energy spacing.[36] By incorporating these QDs in the active region of a laser structure, we can clearly identify which zero-dimensional levels are involved in the lasing and contribute to the gain. To a greater extent than for AlInAs/AlGaAs QD lasers, we demonstrate wavelength tuning and broadband lasing by changing the gain media and injection current.

As mentioned above, the much larger inhomogeneous broadening of the emission spectra of ternary $Al_xIn_{1-x}As$ QDs imbedded in $Al_yGa_{1-y}As$ has prevented the demonstration of quantized 0D energy levels in these QDs. Nevertheless, techniques have been developed to permit the study of individual QDs and therefore to eliminate the inhomogeneous broadening problem.[23,27,28,37,38,39,40,41,42,43,44,45,46] In low dimensional semiconductors, the intersublevel energy spacings are approximately 10-100 meV, the exciton binding energy ~10-35 meV and the fine structure splitting is of the order of a few meV this includes exchange interaction and Zeeman splitting. When probing a large number of QDs, there are ~1-100 QDs per μm^2, broadened emission spectra prevents the

observation of the fine structure as well as the shell structure for the ternary system AlInAs/AlGaAs. The emission broadening disappears when probing single QDs.

There exists different ways to achieve single QD spectroscopy and they can be divided into four main categories according to the excitation source. The first is spatially localized micro-PL spectroscopy using either strong focusing and/or masking. The second technique is near-field optical microscopy to reach below the diffraction limitation of far-field optics, by either exciting, detecting, or both exciting and detecting in the near field. The third method is cathodoluminescence using focused energetic electrons in an electron microscope. The final technique is scanning tunneling luminescence, using low-energy electrons injected or extracted from the tip of a scanning tunneling microscope. Results on single QD spectroscopy presented in this thesis are obtained using the first technique by lithography of as-grown samples as well as using small openings in metal masks. Micro-PL is simple and straightforward, as well as nondestructive. A detailed review of the various techniques listed can be found in ref. 47.

In chapter 5, single QD spectroscopy is used to demonstrate the existence of quantized electron and hole energy levels in $Al_{0.36}In_{0.64}As$ QDs. The excited states and level spacing are obtained by measuring recombination from up to six exciton complexes. Magneto-optical studies yield values for the exciton g factor, and biexciton binding energy. The measured emission spectra are compared with calculated emission spectra from exact diagonalization studies of excitons, charged exciton, and biexciton complexes.

As previously stated, it is now possible to systematically and reproducibly grow single layers of self-assembled QDs which have well-defined excited-state transitions, but only recently has it been possible to observe well-resolved electronic shells in an ensemble of QDs having a number of correlated layers.[48] Coupling between nanostructures is of great interest, and the Stranski-Krastanow epitaxy permits strain-induced vertical self-alignment of QDs The variations in size, composition, and strain in the stacks often cause energy level variations in the adjacent QDs, leading to larger inhomogeneous broadening in ensembles of uncoupled QD stacks, and to charge transfer between asymmetric QDs instead of level splitting for the closely stacked QDs. The self-aligned uniform QDs obtained with the indium flush technique[49] leads to the opportunity of producing coupled QDs by reducing the spacer thickness to grow in close proximity two layers of QDs which are nearly identical.[50] Previous experimental[51,52,53,54,55,56,57] and theoretical work[58,59,60] on coupled QDs reported maximum coupling induced splitting of ~1 meV resulting in large sensitivity to thermal perturbations. These structures are therefore not very well suited for application to quantum information processing. In chapter 6, we present results on the effects of energy level coupling of adjacent QDs. In order to systematically study this effect, the coupling strength between the zero-dimensional states is varied by changing the distance between 2 layers of stacked InAs/GaAs QDs. Results of ensemble and single pair QD spectroscopy are shown and compared with models from the literature. QD energy level splitting larger than 30 meV are observed when the barrier width becomes smaller than 5 nm.

Chapter 2

Fundamental aspects of quantum dot structures

This chapter is intended to provide the reader with adequate background knowledge on the systems discussed in chapters 4-7. The chapter starts by describing some bulk properties of III-V semiconductors, then goes to evaluate the energy levels and DOS for idealized heterostructures. A more detailed model for the energy levels of a lens-shaped heterostructure; the shape generally taken by self-assembled QDs is also described. We also review the interband transition selection rules and the role of excitons in low-dimensional structures. A section is dedicated to the description of the basic growth method and optical properties of self-assembled QDs. The chapter concludes with an example of state filling spectroscopy of a QD sample.

2.1 Bulk III-V semiconductors

2.1.1 Crystal structure of GaAs, InAs, and AlAs

The compound semiconductors GaAs, InAs, and AlAs have the zincblende crystal structure illustrated in figure 2.1.[61] This structure consists of two interpenetrating face-centered-cubic anion and cation sublattices displaced from each other by $(\frac{1}{4}\frac{1}{4}\frac{1}{4})a$, where

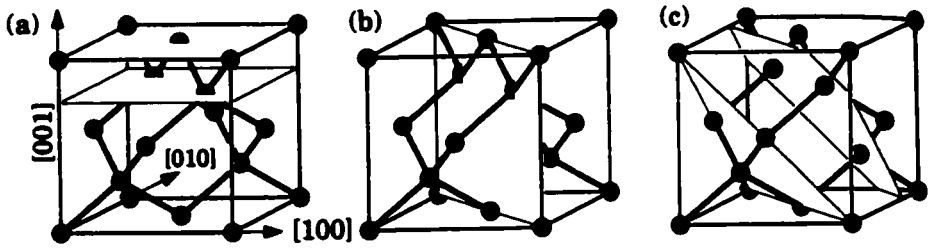

Figure 2.1 Important planes in the zincblende crystal structure of GaAs (a) GaAs(001), (b) GaAs(110), and (c) GaAs(111). From ref. [61].

a is the lattice constant. Heteroepitaxy of III-V semiconductors is commonly done on polar (001) GaAs surface. The {001} planes are separated by $\frac{1}{4}a$ and are alternately occupied by cations or anions. Each pair of (001) planes comprises a monolayer (ML), and there are thus two MLs per unit cell.

InAs, AlAs, and the ternary alloy $Al_xGa_{1-x}As$ have the zincblende crystal structure. The lattice parameter difference between GaAs and $Al_xGa_{1-x}As$ is very small (less than 0.15% at 300 K) which allows growth of heterostructures with almost no strain. The lattice parameter of $Al_xGa_{1-x}As$ can be written a_o (x) = 5.653 + 0.00809x in units of Å at 300 K.[62] However, InAs has a larger lattice parameter than GaAs (a_{InAs} = 6.058 Å and a_{GaAs} = 5.653 Å at room temperature), thus thin InAs films deposited on GaAs substrates are compressively strained. The strain in the overlayer of the thin film can be given by: $\delta = \frac{a_e - a_s}{a_e}$ where a_s and a_e are the unstrained lattice parameters of substrate and epitaxial layer.[63] Thus, in the plane, thin InAs layers on GaAs are compressively strained by 6.7%. Also, for each layer, the tetragonaly distorted InAs is expanded by 14.6% in the (001) growth direction compared to GaAs.

2.1.2 Band structure of GaAs, InAs, and AlAs

GaAs and InAs are direct-gap semiconductors, while AlAs has an indirect bandgap. The band structures of these III-V semiconductors are illustrated in figure 2.2.[64,65] The maxima of the uppermost (heavy and light hole) valence bands of all III-V semiconductors are situated at the Γ point; however there are three conduction band minima (at the Γ, *L*, and *X* points). The relative arrangement of these minima determines

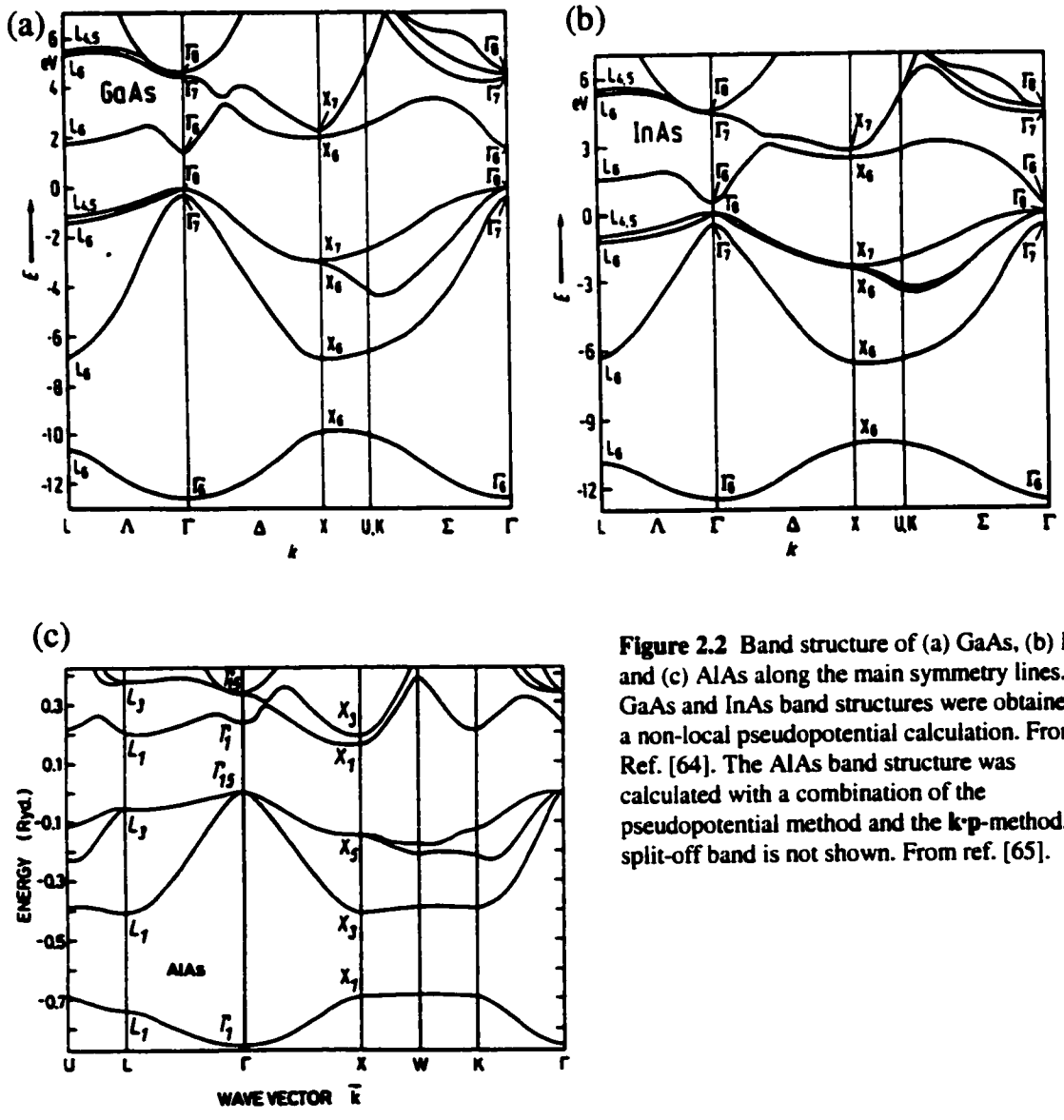

Figure 2.2 Band structure of (a) GaAs, (b) InAs and (c) AlAs along the main symmetry lines. The GaAs and InAs band structures were obtained by a non-local pseudopotential calculation. From Ref. [64]. The AlAs band structure was calculated with a combination of the pseudopotential method and the **k·p**-method, split-off band is not shown. From ref. [65].

the nature of the bandgap. The bottom of the conduction band is located at the Γ point for GaAs and InAs, hence these semiconductors have a direct band gap. In AlAs, the lowest minima in the conduction band is near the *X* point along the [001] direction. AlAs therefore has an indirect bandgap: optical transitions across the gap must be assisted by phonons to satisfy the requirement of momentum conservation. In these bulk materials, the heavy and light hole valence bands are degenerate at the Γ point; however this degeneracy is lifted in strained materials. This degeneracy is also lifted in low-dimensional structures such as QWs and QDs due to the effect of carrier confinement.

For direct-gap semiconductors, near the conduction band edge, the energy-momentum relation is given by a parabolic equation:

$$E(\mathbf{k}) = E_c + \frac{\hbar^2 \mathbf{k}^2}{2m^*} \tag{2-1}$$

where E_c is the conduction band edge, and m^* is the effective mass of the electrons. In general, the effective mass of the carriers is given by the second derivative of the energy E, with crystal momentum $\mathbf{p} = \hbar\mathbf{k}$.

$$\frac{1}{m^*} = \frac{d^2E}{dp^2} = \frac{1}{\hbar^2}\frac{d^2E}{dk^2} \tag{2-2}$$

The effective mass for a narrow parabola at the band edge, therefore, would be smaller in comparison to a wide parabola. Table 2.1 lists the known effective masses for the materials of interest. The effective masses for the holes along the growth axis are:

$$m_{hh}^*(z) = \frac{m_0}{(\gamma_1 - 2\gamma_2)} \tag{2-3}$$

$$m_{lh}^*(z) = \frac{m_0}{(\gamma_1 + 2\gamma_2)} \tag{2-4}$$

where m_0 is the free electron mass and γ_i are the Luttinger-Kohn parameters.

The dependence of the energy gaps of a number of III-V semiconductors on composition (lattice parameter) is displayed in figure 2.3.[66] Direct and indirect energy gaps are plotted with full and broken lines respectively. $Al_xGa_{1-x}As$ has a direct bandgap for $x < 0.46$, and an indirect one at higher aluminium composition. The temperature variation of the bandgap can be described by:

$$E_g(T) = E_g(0) - \alpha T^2/(T+\beta) \qquad (2\text{-}5)$$

where α and β are material dependent constants.[67] The dependence of the bandgap energy on composition and temperature has been determined for a number of III-V semiconductors, including $Al_xGa_{1-x}As$,[68] and $In_xGa_{1-x}As$.[69]

	$Al_xGa_{1-x}As$ bulk parameters	$In_xGa_{1-x}As$ bulk parameters
Electron mass(m_0)	$m_e^* = 0.067 + 0.083\ x$	$m_e^* = 0.067 + 0.04\ x$
Luttinger-Kohn parameters $\left(\frac{\hbar^2}{2m_0}\right)$	$\gamma_1 = 6.85\ (1-x) + 3.45\ x$ $\gamma_2 = 2.1\ (1-x) + 0.68\ x$ $\gamma_3 = 2.9\ (1-x) + 1.29\ x$	$\gamma_1 = 6.85\ (1-x) + 19.67\ x$ $\gamma_2 = 2.1\ (1-x) + 8.37\ x$ $\gamma_3 = 2.9\ (1-x) + 9.29\ x$

Table 2.1 Bulk parameters for AlGaAs and InGaAs.

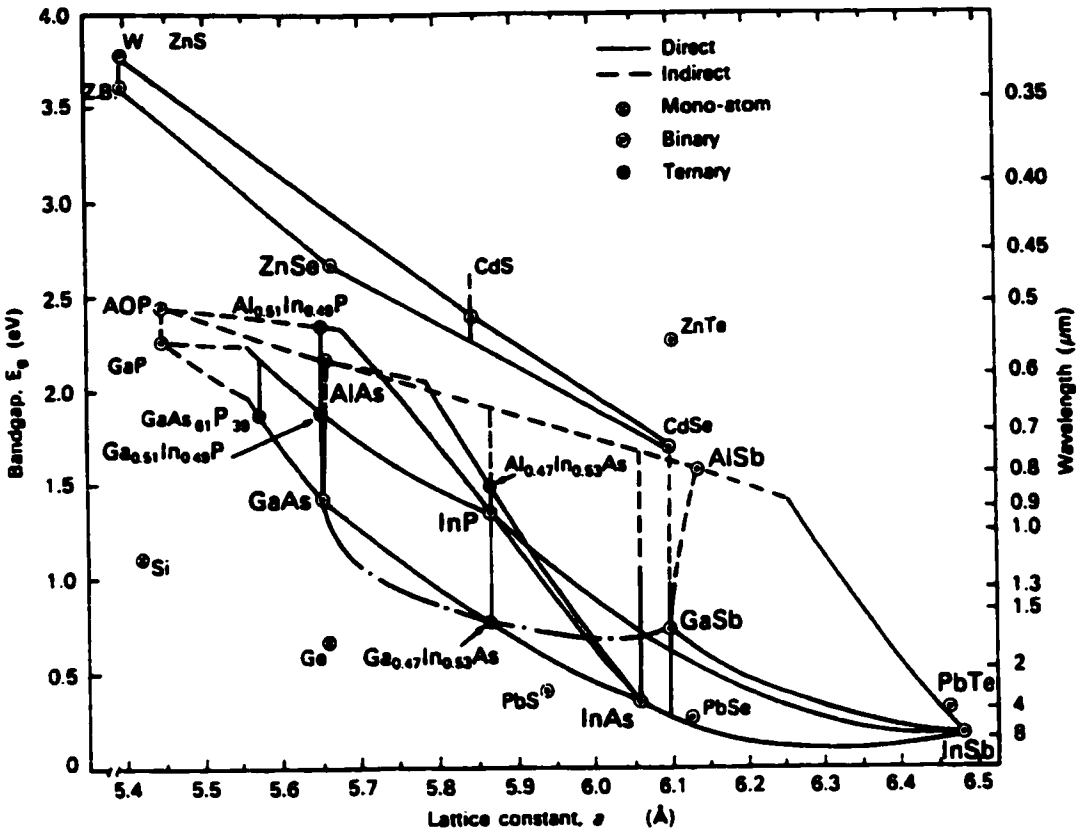

Figure 2.3 Bandgap of common compound semiconductors as a function of composition (lattice constant). From ref. [66].

2.2 Energy levels and density of states for idealized quantum wells and quantum dots

Electrons and holes in bulk semiconductors are free to propagate in all three spatial dimensions. However, it is possible to fabricate structures with reduced dimensionality, in which the electrons and/or holes are confined to a well-defined region of space in one or more directions. Such 'low-dimensional' structures, in which carriers are confined in one, two or all three spatial dimensions are termed QWs, quantum wires

or dots (QDs) respectively.

Confinement of the electrons and/or holes in a given direction can be achieved by trapping them within a potential well of width L of the order of the de Broglie wavelength of the electron $\lambda = h/p$ ($\approx$ 50 nm in GaAs).[70] Such confinement increases the minimum kinetic energy of the carriers and causes their energies to become quantized. Quantum confinement of carriers leads to a drastic modification of the DOS and resultant optical properties. In bulk semiconductors, the lateral and vertical structural dimensions are larger than the de Broglie wavelength. The DOS for electrons and holes in basic systems are calculated using Schrödinger's equation: [1,61]

$$-\frac{\hbar^2}{2m^*}\nabla^2\Psi + V\Psi = E\Psi \quad , \tag{2-6}$$

where m^* is the particle effective mass and E represents the energy of the particle from the band edge. The hard-wall approximation for the potential is used, i.e. the potential V is zero inside the structure and the barriers are infinite. In the case of a cubic potential, separation of variables is applied to solve equation 2-6. For free-particles, the wavefunctions have the form of a travelling plane wave

$$\Psi_\nu = e^{ik_\nu x_\nu} \quad , \tag{2-7}$$

where k_ν is the particle wavevector with the allowed values $k_\nu = \pi n_\nu / L$ and $n_\nu = \pm 1, \pm 2, \ldots$ In Cartesian coordinates, ν can be replaced by x, y or z and L represents a macroscopic length. In the case of particles confined to a microscopic dimension, the particle energy levels are quantized and the wavefunction becomes

$$\Psi_v = \sqrt{\frac{2}{l}} \sin(k_v x_v) \quad , \tag{2-8}$$

where l_v is a microscopic length and $k_v = \pi n_v / l_v$ with $n_v = 1, 2, \ldots$ The total energy is given by:

$$E = \frac{\hbar^2}{2m^*}\left(k_x^2 + k_y^2 + k_z^2\right) \; . \tag{2-9}$$

For a two-dimensional QW, the motion along the growth direction (z) is quantized, so the allowed energies in the z-direction are

$$E_{n_z} = \frac{\hbar^2}{2m^*}\left(\frac{n_z \pi}{l_z}\right)^2 \; . \tag{2-10}$$

The particle wavefunction Ψ is confined to the well width l_z. The DOS up to and including those of energy E is equal to:

$$\rho^{2D}(E) = \frac{m^*}{\pi \hbar^2} \sum_{n_z} \theta\left(E - E_{n_z}\right), \tag{2-11}$$

where $\theta(E)$ is the unit step function and n_z is the subband quantum number. Therefore, the two-dimensional DOS has a staircase shape, as shown in figure 2.4a.

For QDs, quantization occurs in all three directions and the allowed energies are

$$E_{n_x n_y n_z} = \frac{\hbar^2 \pi^2}{2m^*}\left(\frac{n_x^2}{l_x^2} + \frac{n_y^2}{l_y^2} + \frac{n_z^2}{l_z^2}\right), \tag{2-12}$$

with a zero-dimensional DOS expressed as:

$$\rho^{0D}(E) = 2 \sum_{n_x, n_y, n_z} \delta\left(E - E_{n_x n_y n_z}\right), \tag{2-13}$$

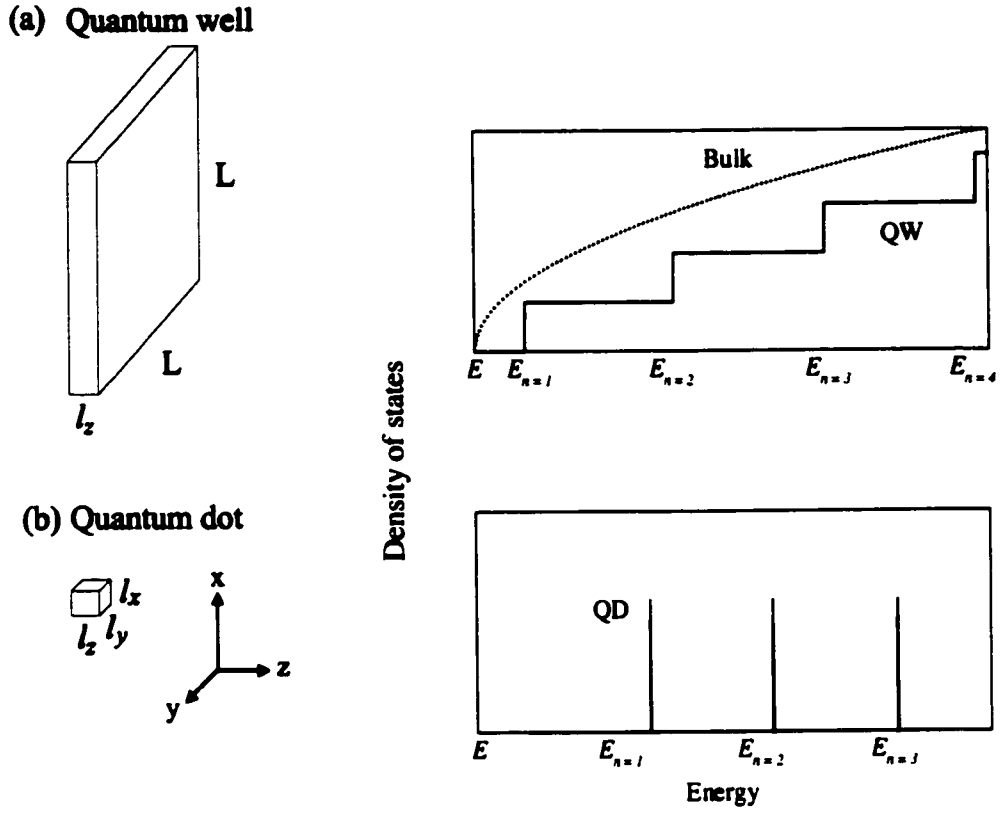

Figure 2.4 DOS for particles confined in (a) two dimensions (the bulk DOS is shown for comparison), and in (b) zero dimensions.

where n_x, n_y, and n_z are the quantum numbers for the allowed energies in the respective directions. This DOS has discrete values as can be observed in figure 2.4b.

As the dimensionality of the structure is decreased, the DOS becomes increasingly discontinuous and the onset of energy levels shifts towards higher values. These effects are independent of the shape of the structure studied, as long as comparison is done between structures of macroscopic and microscopic dimensions.

In the case of QD ensembles, the DOS calculation must take additional factors into account, the most important being the size/composition inhomogeneity of the dot population. The allowed carrier energy level positions and intersublevel spacings in the

QDs will then vary slightly for dots of different size/composition. This will result in a state distribution having a certain width: the larger the population inhomogeneity, the wider the distribution.

2.3 Energy levels in a lens shaped quantum dot

In the (Al)InAs/(Al)GaAs self-assembled system, the QDs can be modeled as lens-shaped (see figure 2.5). Such modeling has been done previously with numerical results for QDs in the InGaAs/GaAs system.[71,72] The disk includes a narrow QW, also

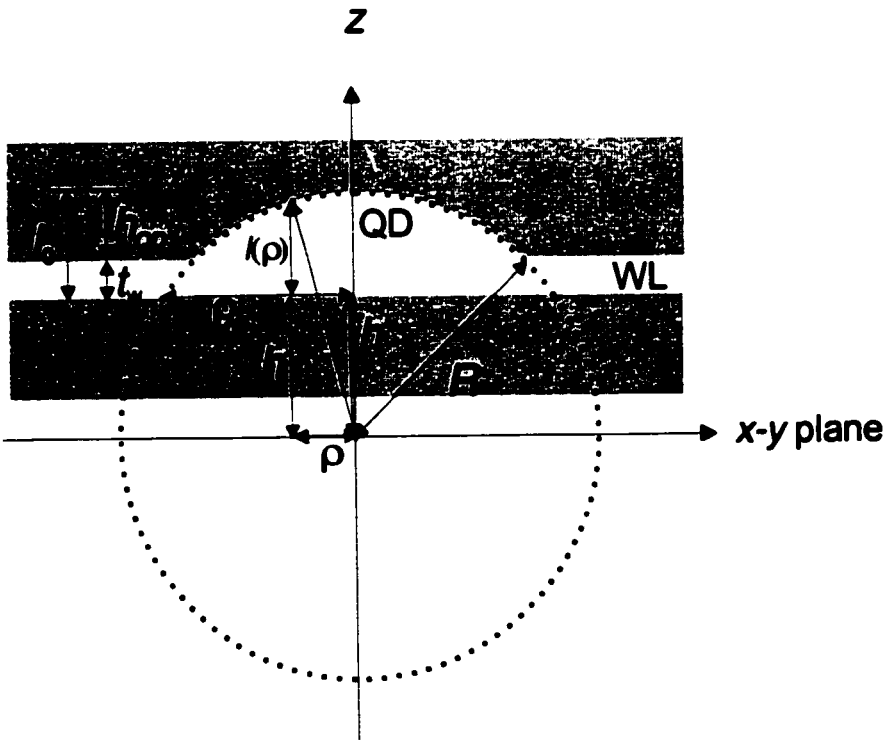

Figure 2.5 Cross section view of an ideal lens-shaped QD. In gray is the barrier material sandwiching the WL and QD shown in white. From ref. [71].

known as the wetting layer (WL), of thickness t_w, and can be modeled as part of a sphere of fixed total height l_0 and base radius ρ_0 as shown in figure 2.5. The bottom of the conduction band of the WL and QD material is below the bottom of the conduction band of the surrounding material. The carriers, confined to a thin QW, are further localized in the area of the dot due to the effectively increased thickness of the layer at these points. The dots have a base diameter in the nanometer range, so that lateral confinement is not negligible.

If an electron-hole pair is trapped in a lens-shaped dot, the effective Hamiltonian can be expressed as:

$$H = \frac{P_e^2}{2m_e} + \frac{P_h^2}{2m_h} - \frac{e^2}{\varepsilon |r_e - r_h|} + V(\mathbf{r}_e) + V(\mathbf{r}_h) \ , \qquad (2\text{-}14)$$

where the subscripts e and h stand for electron and hole, $V(\boldsymbol{r}_e)$ and $V(\boldsymbol{r}_h)$ are the carrier confining potentials due to the dot shape and the middle term is the Coulomb interaction inside the dot. ε is the dielectric constant. For QD sizes $R >> a_B$, where R is the base radius of the QD and a_B is the excitonic Bohr radius, the problem can be solved in analogy to the particle-in-a-box problem if one considers the electron-hole pair, i.e. the exciton, as a single particle with the confining potential acting only on the center-of-mass motion.[73] The problem therefore simplifies to the one-particle effective-mass Schrödinger equation (equation 2-6).

The confining potential $V(\boldsymbol{r})$ must be consistent with the shape of the lens-shaped QD. As shown in figure 2.5, a QW of thickness l_0 can become a lens-shaped QD of similar thickness at the center with a radius at the base of ρ_0. The difference in

confinement comes from an extra lateral confinement which allows the potential $V(\boldsymbol{r})$ to be written as $V(\boldsymbol{r}) = V(z) + V(\rho)$, where $V(z)$ is simply the potential profile of a QW of thickness l_0. To obtain an explicit form for $V(\rho)$, the adiabatic approximation is used. This method states that the potential a particle feels, when moving in the x-y plane, is given at each point by the ground state energy of a QW of equivalent thickness $l(\rho)$. The confining potential is zero inside the dot and WL, but finite outside, this way equation 2.-10 for E_z can be used replacing l by $l(\rho)$. The potential is then:[71]

$$V(\rho) = E_{QW}(l(\rho)) - E_{QW}(l_0) = \frac{\hbar^2\pi^2}{2m^* l^2(\rho)} - \frac{\hbar^2\pi^2}{2m^* l_0^2} \qquad (2\text{-}15)$$

and $l(\rho)$ can be written as $l(\rho) = \left(R^2 - \rho^2\right)^{1/2} - h$ based on geometry shown in figure 2.5. $V(\rho)$ can be written as:

$$V(\rho) = \frac{\hbar^2\pi^2}{2m^*}\left(\frac{1}{\left[\left(R^2-\rho^2\right)^{1/2} - h\right]^2} - \frac{1}{l_0^2}\right). \qquad (2\text{-}16)$$

The Schrödinger equation with the Hamiltonian of equation 2.14 and a potential of the shape of equation 2-16 can be solved numerically. Alternatively, a harmonic approximation can be obtained from a Taylor series expansion of $V(\rho)$:[72]

$$V(\rho) = \frac{\hbar^2\pi^2}{2m^* R^2}\left(\frac{1}{\left(1 - h/R\right)^3}\left(\frac{\rho}{R}\right)^2 + \frac{1}{4}\frac{4 - h/R}{\left(1 - h/R\right)^3}\left(\frac{\rho}{R}\right)^4 + O(\rho^6)\right) \qquad (2\text{-}17)$$

and setting the ratio $A = l_0/\rho_0 \sim 0.2$ for self-assembled QDs. In this case, equation 2-6 reduces to

$$\frac{\hbar^2}{2m^*}\nabla^2\Psi + \left(V(z) + \frac{1}{2}m^*\omega^2\left(x^2 + y^2\right)\right)\Psi = E\Psi \qquad (2\text{-}18)$$

where

$$\omega^2 = \frac{4A^2}{(1+A^2)} \frac{\pi^2 \hbar^2}{m^{*2} l_0^4} . \tag{2-19}$$

Equation 2-18 is separable into a square QW in the z-direction and harmonic oscillators in the x and y directions. In the z direction, only the ground state energy is needed for InAs/GaAs since the QDs are thin:

$$E_z = \frac{\hbar^2 \pi^2}{2m^* l_0^2} \tag{2-20}$$

The solution of the harmonic oscillator can be found in the literature:[74]

$$E_x + E_y = (n_x + n_y + 1)\hbar\omega = (n_x + n_y + 1)\frac{2}{\pi}\sqrt{\frac{2A^2}{(1+A^2)}}\frac{\hbar^2 \pi^2}{2m^* l_0^2} \tag{2-21}$$

where n_x, n_y = 0, 1, 2, ... The results apply for both electrons and holes when using the appropriate effective mass and frequency (ω).

The resulting spectrum consists only of discrete bound state energies. The shells are spaced evenly (intershell spacing of the order of tens of meV), and the intershell spacing decreases with increasing dot size. The first bound state is filled up with two particles; the second bound state is filled after four particles and so on when including level and spin degeneracy. This model does not take the effects of strain into account but has been shown to correspond well with experimental results; more detailed models have been developed for lens-shaped dots[71] and for pyramidal dots.[75] The conclusions hold for structures with finite potential barriers. In this case, the energy levels of a finite square QW of thickness l can be obtained numerically from:[76]

$$l\left(E_{n_z}^{QW}\right)=\frac{2\hbar}{\sqrt{m_w^* E_{n_z}^{QW}}}\left[\tan^{-1}\left\{(-1)^{(n_z+1)}\left(\sqrt{\frac{m_w^*}{m_b^*}\left(\frac{V_0}{E_{n_z}^{QW}}-1\right)}\right)^{(-1)^{(n_z+1)}}\right\}+\pi\times\mathrm{int}\left(\frac{n_z}{2}\right)\right]. \quad (2\text{-}22)$$

The lateral confinement remains strong and qualitative results can be obtained by fitting the obtained form of $V(\rho)$ to the closest harmonic function, or simply by solving the radial potential numerically.[71]

The QDs obtained through the Stranski-Krastanow growth mode have potential barriers with finite heights, and therefore, at elevated temperatures carriers can escape the confined region by thermionic emission into the barrier material.[77] This important carrier-loss process is especially significant in structures with shallow barriers.[78] The carrier distribution between the active region (QD) and the confining layers (barrier and WL) is controlled by carrier thermalization/capture processes in the QD and the escape processes from QD to WL or barrier through thermionic emission. The probability per unit time for a carrier to absorb phonons and be emitted above the barrier is greatly enhanced at high temperatures due to a large phonon population in the lattice. Consequently, quenching of the emitted light intensity is observed at higher temperatures according to an exponential law of the form

$$I(T)=\frac{c}{1+\alpha\exp\left(-E_A/k_BT\right)}, \quad (2\text{-}23)$$

where c and α can be fitted to experiment, k_BT is the thermal energy, and E_A is the activation energy which corresponds to the minimal energy necessary to promote carriers to unbound energy levels. The onset of thermionic emission depends on the values of α and E_A.

2.4 Interband transition selection rules

Due to their discrete energy states, the transitions between the electron and hole levels in QDs are analogous to those between the discrete levels of an atom. The band-to-band transition probability per unit time is given by Fermi's golden rule. In the case of the creation of a photon:[79]

$$P_{i,f} = \frac{2\pi}{\hbar}\frac{e^2 F^2}{4m_0^2\omega^2}\sum_{i,f}\left|\langle f|\mathbf{e}\cdot\hat{\mathbf{p}}|i\rangle\right|^2 \delta\left(E_i - E_f - \hbar\omega\right), \tag{2-24}$$

where $\mathbf{e}$ is the light polarization vector and $\hat{\mathbf{p}}$ is the momentum operator. The sum is over all the levels in the conduction and valence bands (initial states $|i\rangle$ and final states $|f\rangle$). E_i and E_f represent the energies of the initial and final states, $\langle f|\mathbf{e}\cdot\hat{\mathbf{p}}|i\rangle$ is the optical matrix element expressing the coupling between the initial and final states with the light polarization, and the term preceding the sum represents a constant of the system. Conservation of momentum and energy accompany emission and absorption of photons.

The reduced DOS observed in low-dimensional systems (compared to the usual bulk probability transitions) is introduced in the summation over initial and final states to account for dimensionality in the wavefunctions and the joint DOS. The electron and hole wavefunctions $\Psi_{i,f}(\mathbf{r})$ in low-dimensional systems are a product of the envelope function $\chi(\mathbf{r})$ and the appropriate Bloch function $u_{n\mathbf{k}=0}(\mathbf{r})$ at the Γ point, $\Psi(\mathbf{r}) \propto \chi(\mathbf{r})\, u_{n\mathbf{k}=0}(\mathbf{r})$. The matrix element in (2-24) can be factorized into the integral over the unit cell of the fast varying part of the wavefunction (the Bloch function) and a

sum at the cell centers $\mathbf{R_i}$ of the slowly varying functions (the envelope function).

The optical matrix element for transitions that involve an electron from a conduction band and a hole from a valence band is:

$$\langle f|\mathbf{e}\cdot\hat{\mathbf{p}}|i\rangle \approx \sum_{R_i} \chi_e(\mathbf{R_i}) e^{-i\mathbf{k_e}\cdot\mathbf{R_i}} \chi_h(\mathbf{R_i}) e^{i\mathbf{k_h}\cdot\mathbf{R_i}} \int_{\text{cell}} u_{ck_e}(\mathbf{r})(\mathbf{e}\cdot\hat{\mathbf{p}}) u_{vk_h}(\mathbf{r})\, d\mathbf{r} \quad , (2\text{-}25)$$

where e and h represent electrons and holes and the integral is over unit cells. The electron and hole wave vectors are designated as $\mathbf{k_e}$ and $\mathbf{k_h}$. The exponential factors give a null contribution unless $k_e = k_h$, which is the vertical transition rule since light has negligible momentum. When factorizing the electric-dipole matrix element in equation 2-24, the change in parity of electric-dipole transitions appears in the Bloch integral matrix element; this is just the same as in bulk systems.

2.4.1 Selection rules on the envelope function quantum numbers

The other selection rules have two origins: the overlap integral between envelope functions selects the quantum numbers of the initial and final level and the atomic-like dipole matrix element imposes the selection rules on polarization of the light wave. The atomic-like part of the Bloch wavefunction is similar for all III-V materials and the polarization selection rules are not dimensionality dependent.

The matrix elements for the envelope functions are integrals over their product with no polarization dependence. If the electron and hole QD potentials are symmetric, the envelope functions could be symmetric or anti-symmetric and their matrix elements will vanish unless both have the same parity. If the potential in both conduction and

valence bands can be modeled as a quantum box with infinite potential walls, then the two sets of envelope functions are identical and only transitions between levels with the same index are allowed, this is the "$\Delta n = n - m = 0$" rule, where m is a valence-band state and n is a conduction-band state. In the case of lens-shaped dots, QD wavefunctions have to be used, which for the first few levels can be approximated by in-plane harmonic functions.[71] The envelope functions are not exactly orthogonal since the effective depth of the confining potential is different for electrons and holes. This can lead to observations of transitions between $n \neq m$ states. These transitions will have weak intensities, and in order to conserve parity, $n - m = odd\ integer$ will only appear in the case of highly asymmetric potentials.[1]

2.4.2 Oscillator strength

The oscillator strength f characterizes the strength of optical transitions and is defined as:

$$f_{fi} = \frac{2}{m\hbar\omega_{fi}} \left| \langle f | \mathbf{e} \cdot \hat{\mathbf{p}} | i \rangle \right|^2 \tag{2-26}$$

where m is the free electron mass. This oscillator strength in semiconductors relies on the distribution of quantum states in k-space of a solid: due to k-conservation in optical transitions, very few states are coupled within a given energy range, i.e., only a very small fraction of the total number of electrons of the solid participate in the transition. The low-dimensionality of confined systems compared with bulk does not increase the oscillator strength per electron-hole. But when comparing bulk and low-dimensional systems,

quantum confinement leads to a better matching of electron and hole wavefunctions: for QDs, all electrons and holes in a same quantized subband have the same k-wavevector, which leads to a stronger oscillator strength compared with transitions in bulk or two-dimensional structures.

2.4.3 Polarization selection rules

Selection rules for the electromagnetic wave polarization can be obtained using the parabolic band approximation, and examining the periodic parts of the Bloch functions of the electrons, and different types of holes. The periodic parts of the Bloch functions are obtained from the $k \cdot p$ method. The conduction band has s-like symmetry, i.e. spherical symmetry, while the heavy hole band has p-like symmetry, i.e. the form of a butterfly rotating in the plane perpendicular to the wavevector k, the light hole band also has this p symmetry. The angular momentum of the Bloch functions are $m_j = \pm 3/2$ for the heavy hole level at $k = 0$, and $m_j = \pm 1/2$ for the electron and light hole levels. The various allowed transitions can be calculated as in the atomic physics case of transitions between ground and excited levels. In the case of $\Delta m_j = 0$, the emitted or absorbed photons are linearly polarized, while for $\Delta m_j = \pm 1$ photons are circularly polarized. These selection rules will be discussed in more detail in chapter 5 for QDs.

2.4.4 Excitonic effects

The optical properties of semiconductors are greatly influenced by the formation of excitons. An exciton is an electron-hole pair in which the Coulomb attraction between

the electron and the hole causes their motion to be correlated. In semiconductors, the attraction extends over a large number of unit cells, and the electron and hole are weakly bound (Wannier-Mott excitons).

The attraction between the electron and the hole leads to bound levels in bulk crystal, as in the case of the hydrogen atom. The energies of the bound states are given by:

$$E_n^{3D} = E_g - \frac{R_{eh}}{n^2} \tag{2-27}$$

where $R_{eh} = \frac{m_{red}}{m_0}\frac{1}{\varepsilon_r^2}R_y$ is the Rydberg energy (R_y = 13.6 eV) scaled by the dielectric constant of the host and the reduced mass of the electron-hole pair ($1/m_{red} = 1/m_e + 1/m_h$). The exciton Bohr radius is given by $a_{eh} = \varepsilon_r \frac{m_0}{m_{red}} a_B$ where a_B = 0.0529 nm).

Excitons give rise to a series of discrete absorption lines below the semiconductor band edge. These linesares broadened as the temperature increases due to the interaction of excitons with optical phonons. The lowest bound state or exciton binding is approximately 5 meV in bulk GaAs.[80] The weak binding energy means that excitons are ionized at room temperature, and exciton emission lines are only observable at low temperature. In III-V semiconductors, usually only the first exciton line (n = 1) is seen since the oscillator strength of these transitions scale as n^{-3}.[81]

Excitonic effects increase in importance as the dimensionality of a structure decreases due to an increase in the exciton binding energy. For example, the binding energy of a heavy-hole exciton rises from about 5 up to 10 meV in GaAs based QWs.[1] This increase in binding energy means that the excitons are visible in the optical

absorption spectra of QWs up to room temperature. The exciton binding energy in self-assembled GaAs-based QDs is evaluated at ~30-40 meV.[22] The solutions for the exciton matrix elements have the same results as the interband selection rules.[20]

2.5 Growth of self-assembled quantum dots

Zero-dimensional semiconductor structures may be obtained through numerous growth techniques. The most straight forward technique is to grow two-dimensional layered structures (QWs) and following this by a lateral patterning through a combination of high-resolution electron beam lithography and dry or wet chemical etching, to produce QDs with diameters down to ~ 25 nm.[82,83,84,85,86] Other fabrication techniques used in production of QDs include intermixing where a focussed ion beam having a diameter of 50 nm was used to modify the lateral bandgap profile,[87] gate modulation of patterned confining layer,[88] overgrowth on vicinal surfaces,[89] and selective growth on a patterned substrate.[90] It has been shown that the etching techniques required in the fabrication of QDs through pattern transfer onto semiconductors introduce additional damage forming a depletion layer at the surface of the patterned device, and thus affects the electronic properties of the materials. This damage manifests itself on a microscopic level in the form of nonradiative defects such as dislocations and vacancies.[1] In the case of gate modulation devices and intermixing techniques, small carrier confinement are obtained, making the observation of quantum effects possible only at very low temperatures. Further, there are serious problems in the fabricated structures themselves such as low

density, and size irregularity making them difficult to use in device applications. Dots may also be obtained by growth of nanocrystals in glass matrices, and in organic materials and related matrices.[73,91] These systems allow for large QD densities, although a major draw back is difficult electrical injection of carriers in these systems.

Epitaxial growth utilizing self-organized island formation in highly mismatched epilayer/substrate systems is now being welcomed as a serious technique to overcome the problems stated above. Strain induced self-assembled growth leads to the formation of small dots (about 10 - 30 nm diameter) having good size uniformity, and a high density (between 10^8 to 10^{11} dots/cm^2). In the past eight years, QDs have been grown in a variety of III-V semiconductor systems including InAs/GaAs,[37,92,93,94] InAlAs/AlGaAs,[27] and InAs/InP,[95] in II-IV materials like CdSe/GaAs,[96] and in the indirect bandgap group-IV system SiGe/Si.[97] Since the fabrication of dots is intrinsic to the growth method used, this technique is attractive for device applications mostly through its compatibility with commercial growth systems as well as the availability of ultrapure elements needed for growth. The QDs used in this study were obtained through spontaneous island formation.

The crystal growth on a bulk substrate occurs in one of three distinct modes, schematically shown in figure 2.6:[97,98] Frank-van der Merve mechanism or layer-by-layer growth,[99] Stranski-Krastanow mechanism or layer-by-layer growth followed by 3D island formation,[100] and Volmer-Weber mechanism or island growth.[101] The selection of one growth mode over another depends on the epitaxial layer and the substrate on which it is to be grown. In fact, it was shown that, owing to the difference in nature and strength of the chemical bonds, and the lattice parameters, the three growth modes could be covered.[102] Because of these fundamental parameters (bond strength and lattice

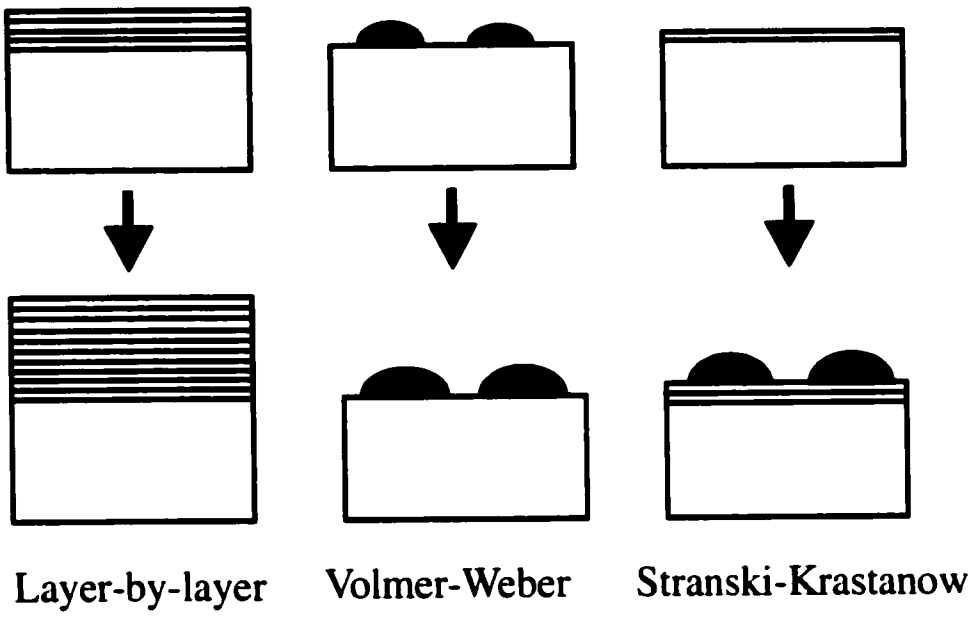

Figure 2.6 Schematic representation of the three possible growth mechanisms of thin epitaxial films.

parameters), the chemical potential of the overgrowth differs from that of an infinitely large crystal. Across the interface, the atoms of the deposit can be bound more loosely (or tightly) to the substrate atoms than to the atoms of the same crystal. Consequently, the chemical potential of the first layers of the deposit could be higher (or lower) than the chemical potential of the infinitely large deposit crystal. The Volmer-Weber growth mode occurs when the interfacial bonding is weaker than the bonding in the deposit itself, that is, the adatoms will have a tendency to form islands on the surface to minimize the interface area. In systems having strong interfacial bonding, layer-by-layer growth occurs; the atoms "wet" the entire surface. At this point, the lattice misfit plays a prominent role in determining the growth mode. The larger the misfit, the greater the tendency towards island growth. Generally, layer-by-layer growth occurs if the misfit is small. If the misfit is substantial, coherently strained islands grow on top of the WL until they reach the dislocation-formation critical thickness. This is known as the Stranski-

Krastanow growth mode. The size and shape dispersion of these islands is very small at the onset of island growth. If the growth is allowed to proceed above the critical thickness with the same lattice mismatched material, generation of dislocations at the interface between the layer and the substrate will occur, producing strain relaxation. Once formed, these incoherent, strain-relaxed islands, continue to grow with little restriction until a complete two-dimensional film has been developed. If, on the other hand, before reaching the critical thickness for dislocation, the defect-free dots are capped with a material having the same lattice constant as the substrate, the growth proceeds epitaxially without introduction of dislocations. The QDs are then sandwiched between two similar epilayers.

2.6 Basic optical properties of GaAs-based self-assembled quantum dots

2.6.1 Zero-dimensional properties

Control of the QD energy levels is possible by varying the growth conditions. For example, S.-Z. Chang, T.-C. Chang, and S.-C. Li have observed that for systems with low lattice mismatch (1-2 %), the QD density is high and the QD sizes are small; for larger lattice mismatch (> 2 %), the QD density is lower and the QD sizes are larger.[103] To obtain good-quality QDs with well-resolved excited state emission in the InAs/GaAs system, it has been found that there are five main parameters to control during the growth: (1) the substrate temperature is selected to control the size of the QDs, and thus, to obtain

the desired intersublevel energy spacing.[36.104] (2) The amount of strained material deposited (here InAs) has to be precisely determined for the chosen growth temperature to control the density of the QDs, and thus, obtain well-resolved excited states.[36.105] For an optimized density, in addition to a number of QD states, the WL PL is typically observed in state-filling spectroscopy. (3) The indium diffusion length during growth can be controlled using the arsenic pressure, this is an additional parameter that controls the size and QD density.[106] (4) Depending on the growth rate chosen for the strained material, a growth interrupt (anneal) must be used to let the QDs evolve to their equilibrium shape and obtain good ensemble uniformity.[36.107] (5) An indium–flush technique can be used during the capping of the QDs for additional size and shape engineering.[36.49]

The optical excitation of self-assembled QD systems yields bright luminescence and generally reveals a Gaussian line shape distribution (figure 2.7a). In the case where nonresonant excitation is used, PL data display smooth and structureless spectra. Typically for such PL experiments, the spot size is of the order of 100 μm diameter, and therefore for characteristic dot densities of 200 μm^{-2}, a large number of QDs are probed (~ 10^6 dots). The PL data therefore reflects the statistical distribution of the ground state energy levels of the individual dots that arises from the slightly different zero dimensional confining potentials. Since the QDs have a deep confining potential and a relatively small height-to-diameter ratio, this distribution should arise mainly from the additional atoms along the growth direction. Other parameters, such as small variations in the diameter, in the alloy composition, or in partial (defect-free) strain relaxation, can also contribute to the observed inhomogeneous broadening in the emission spectrum.

A smaller number of QDs can be probed through the use of mesas, etched from the QD structure, of different sizes[27] or simply by performing micro-PL, where the probing laser spot size is reduced to the diffraction limit (~ 1 μm). Figure 2.7b shows the results obtained on mesas of different sizes (3, 7 and 13 μm^2) obtained from the same sample as in figure 2.7a, having a dot density estimated at 200 per μm^2 (from TEM plane view measurements). The corresponding number of dots probed is estimated at N ~ 600, 1400, and 2500 dots respectively. For the small mesas containing only a few hundred dots, the PL spectrum displays distinct, very narrow lines (full with at half maximum (FWHM) ~ 100 μeV). As the number of dots probed increases, the spectra become smooth, as expected, by considering the statistics of large number of added lines. The appearance of the sharp spectral lines is an indication of the zero-dimensional nature of the DOS.

Temperature-independent emission linewidth was predicted theoretically and is simply a consequence of the δ-function like DOS due to the zero-dimensional nature of the dots. Exciton lifetime measurements done on these sharp spectral features were shown to be constant with temperature[108] up to the onset of thermionic emission; a further evidence of the zero-dimensional nature of these self-assembled dots.

The atomic-like discrete energy spectrum of each QD state can easily lead to a state-filling effect at higher optical excitation, due to the exclusion principle when only a few carriers can populate the lower states. In fact, theoretical calculations emphasized that only two electrons can occupy the ground state level of a dot (spin up and spin

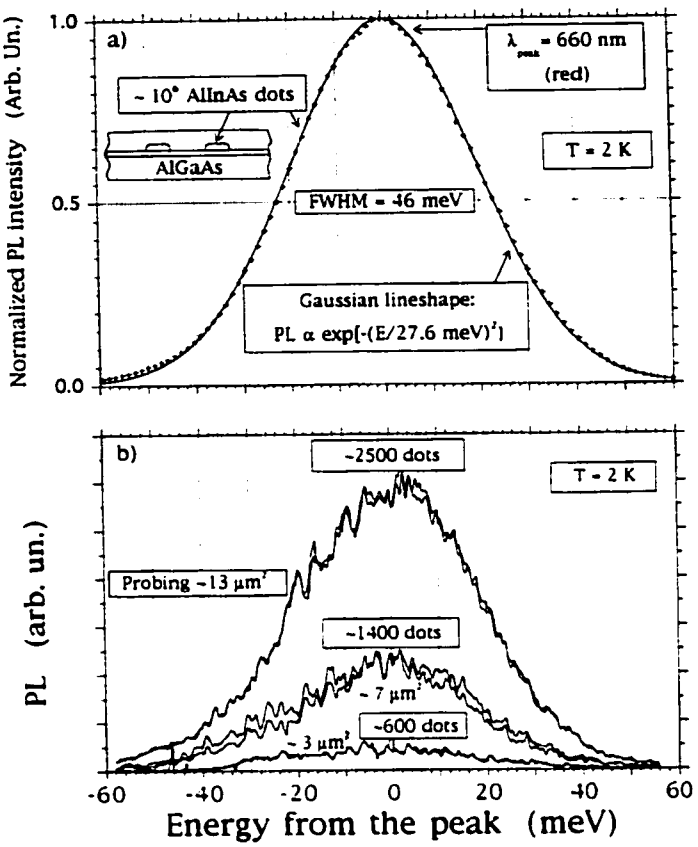

Figure 2.7 (a) Low-temperature PL spectra obtained with an InAlAs/AlGaAs QD sample, probing a large ensemble (~10^6) of 17-nm diameter dots under the excitation spot, and a Gaussian distribution fit. (b) PL of *N*-dot ensembles delineated with μm-size mesas, displaying statistical fluctuations. Two scans are shown for each mesa to evaluate the reproducibility of the sharp features. The peak position for the InAlAs/AlGaAs QD ensembles is $\lambda = 660$ nm. From ref. [27].

down), four electrons in the first excited state (n = 2) and so on. This causes observation of excited state interband transitions as the excitation intensity is increased. State-filling will show clear saturation effects as well. At low excitation intensities, only the (inhomogeneously broadened) ground state levels are generally observed because of the fast inter-sublevel relaxation process taking place. As the intensity is increased, a progressive saturation of the lower energy transitions is combined with the emergence of new emission peaks originating from the excited state interband radiative transitions. These effects can also be observed as the inter-sublevel carrier relaxation towards the

lower levels is slowed due to the reduced number of available final states.[34,35,95]

An example of state-filling effect, where the intersublevel spacing is larger than the inhomogeneous broadening, is depicted in figure 2.8 for the InAs/GaAs system. The sample has a single layer of InAs QDs located 100 nm from the sample surface. Continuous wave (CW) or steady state PL of the sample is done using the 532 nm line of a Nd:YVO_4 laser and the sample luminescence is detected using a charge-coupled-

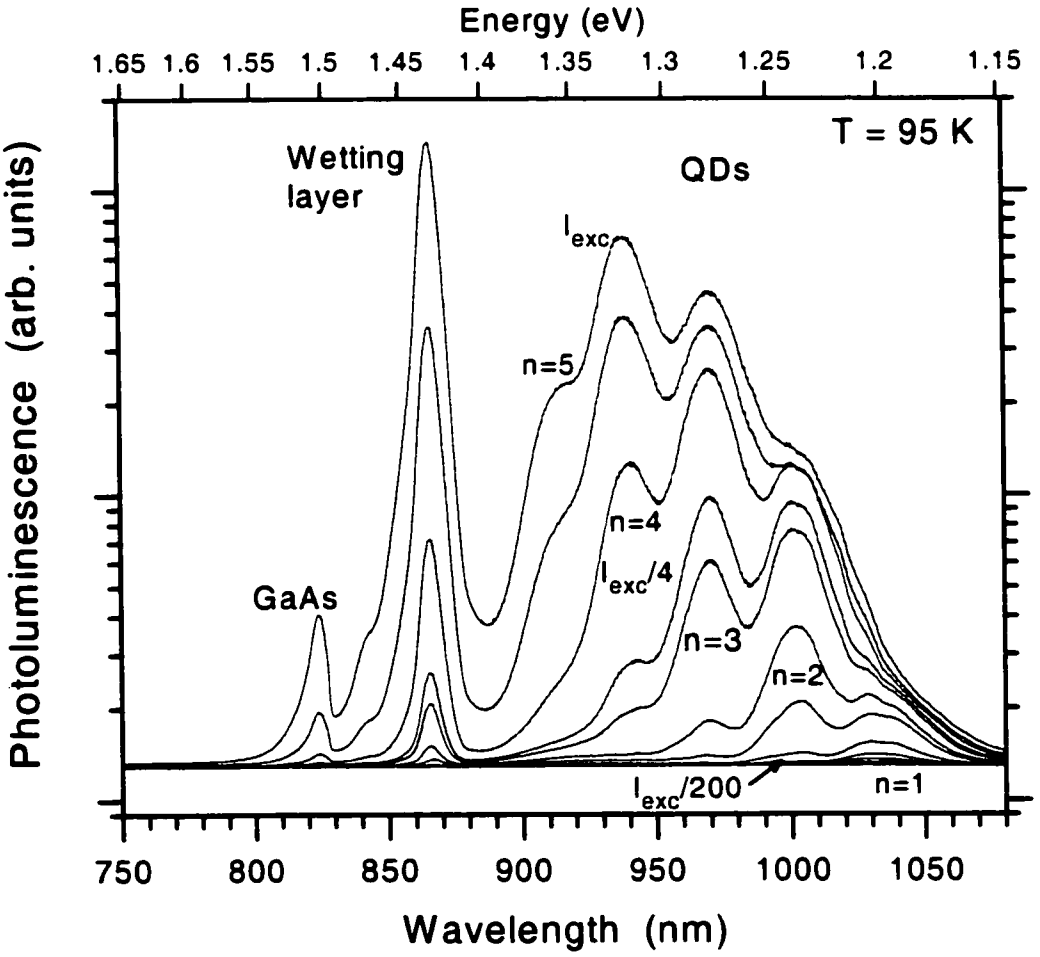

Figure 2.8 PL spectra obtained at $T = 95$ K with different excitation intensities (I_{ex}) of InAs/GaAs QDs, displaying strong level filling and emission from the excited states and saturation of the ground states with increasing excitation intensities. $I_{ex} \sim 1500$ W/cm^2.

devices (CCD). The five QD levels can be filled with up to 30 electrons per QD. The n =1 level is completely saturated at the higher excitation intensities. The WL, the thin QW below the QDs, is visible at 865 nm, as well as emission from bulk GaAs at 825 nm. Figure 2.9 is a schematic of the position of the energy levels for this sample. The five QD energy levels are spaced 40 meV one from another, and the WL shows only one confined subband.

Assuming a density of 50 QD/μm^2, the number of states available is given by equation 2-13 for the five energy levels found experimentally and results in 100 μm^{-2} for the lowest energy level QD(1), 200 μm^{-2} for QD(2), 300 μm^{-2} for QD(3), 400 μm^{-2} for QD(4), and 500 μm^{-2} for QD(5) assuming orbital degeneracy.[109] The number of available states in the thin WL is obtained using the DOS of equation 2-11 where it has been found that only one bound state is supported for the electrons and for the holes for a QW of the thickness of the WL using equation 2-22. The electron effective mass $m^* = 0.067m_0$, as stated in table 2.1, and the WL electron DOS is therefore 2.8 x 10^{10} meV^{-1} cm^{-2}. The

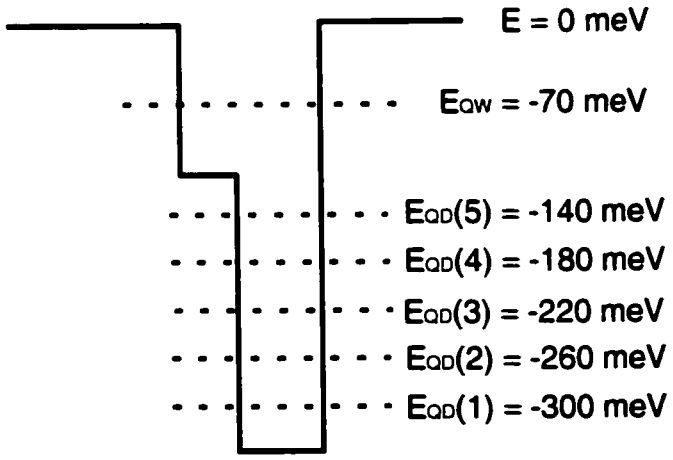

Figure 2.9 Schematic of the position of the energy levels for sample 2159 from figure 2.8. The GaAs barrier is set as the reference ($E = 0$ meV)

number of states available is thus 19600 μm^{-2} for the WL between E = -70 meV (the two dimensional continuum) and E = 0 meV (the onset of the three dimensional continuum).

The incoming laser beam is directed toward the top of the sample perpendicular to the strained layer. Let f be the proportion of carriers captured in the layer. For low excitation intensity f can be approximated using known optical constants.[63] The laser excitation energy is 2.33 eV, the real and imaginary parts of the refractive index for GaAs are n = 4.1 and k = 0.37. These values indicate that 37 % of the laser beam is reflected at the surface. The QD layer is located 100 nm from the surface. Using an absorption coefficient $\alpha \sim 1 \times 10^5$ cm^{-1} for GaAs, and assuming efficient carrier capture of the carriers by the strained layer based on the relative peak intensities of bulk GaAs compared with InAs peaks, ~30% of the incident intensity is transformed into captured carriers in the InAs layer, so f = 0.30.

The average number of electron-hole pairs N in a given QD at any time, can be calculated by first evaluating the average surface carrier density σ present in the strained layer. The average surface carrier density can be written as $\sigma = \frac{P_{exc}}{E_{photon}} f \tau$, where P_{exc} is the power of the incident laser beam, E_{photon} is the energy of incident photons, and τ is the carrier lifetime in the QDs.[72] The carrier lifetime is set at 1.0 ns.[109] Lets suppose the 50 QDs are evenly spaced over a 1 μm^2 area so that they each have the same capture coefficients. In order to saturate the first QD energy level, an excitation power

$$P_{exc}(n=1) = (100\ \mu m^{-2})\ (3.7 \times 10^{-19}\ J/photons) / (0.3)\ (1 \times 10^{-9}\ s) = 12\ W/cm^2$$

is needed. To saturate the n = 2 energy level,

$$P_{exc}(n=2) = (12 + 24)\ W/cm^2 = 36\ W/cm^2,$$

the n = 3 energy level,

$$P_{exc}(n=3) = (36 + 36)\ W/cm^2 = 72\ W/cm^2,$$

the n = 4 energy level,

$$P_{exc}(n=4) = (72 + 48)\ W/cm^2 = 120\ W/cm^2,$$

and for the n = 5 energy level,

$$P_{exc}(n=5) = (120 + 60)\ W/cm^2 = 180\ W/cm^2.$$

To saturate the WL,

$$P_{exc}(WL) = (180 + 2400)\ W/cm^2 = 2580\ W/cm^2$$

is needed.

Let us now compare these excitation intensities with the results observed in figure 2.8. For the lowest curve in figure 2.8, the excitation power is 0.02 W/cm^2, so the average surface carrier density σ = (0.02 W/cm^2) (0.3) (1 x 10^{-9} s) / (3.7 x 10^{-19} J/photons) = 1.6 x 10^7 cm^{-2} = 0.16 μm^{-2} and the average number of carriers in a given QD at any time is ~ 0.003. The lowest QD shell intensity saturates at $P_{exc}(n=1)$ = 150 W/cm^2 equivalent to having on average N = 24 electron-hole pairs per QD, and the n = 2 level saturates at $P_{exc}(n=2)$ = 375 W/cm^2 in figure 2.8. These values are an order larger than the calculated values. At the point were the lowest energy level is filled in figure 2.8, one observes that the second, third, fourth and even fifth level are partially filled, the same scenario is present for the saturation of n = 2. This is mainly due to a non-uniform Gaussian excitation profile.[109] This could also be due in part to the statistics of carrier trapping by the different QDs, and also to the different rate of carrier relaxation, and recombination times of the different QD levels.

Most of the carriers are created in the barrier levels when exciting at energies higher than the barrier energy, and will subsequently relax to the zero-dimensional QD ground state. There are two main possible carrier relaxation mechanisms: phonon scattering and Auger scattering. After excitation in the barrier material, carriers can relax to the QD levels, this can be achieved by simultaneous emission of multiple phonons, or sequential emission of phonons, so the carriers can relax to the WL band edge, at which point multi-phonon emission is likely required for the carriers to relax in the QD ground state. Auger scattering can either occur by direct or sequential trapping. For direct trapping, a single collision takes place in which the carrier falls to the QD ground state. For sequential trapping, the first collision helps the carrier to relax in the WL states, while a subsequent collision will help the carrier to relax to the QD ground state. Recent papers have shown that Auger-type processes dominate at higher excitation intensities.[110,111] As well, even if the laser spot used in the experiment was slightly defocussed, the laser beam intensity has a Gaussian lineshape with the center having the highest intensity. This allows for uneven carrier excitation of the QDs over the probe area. At higher excitation intensities, the relation between P_{exc} and f, the proportion of carriers captured in the layer, ceases to be linear. The value of f decreased at higher intensity and could in part be due to bleaching of the states resonant with the laser energy in the bulk material.[72] Carrier bleaching is another factor that can affect carrier trapping, but is unlikely to be important here because the intensities are not high enough.

2.6.2 Indium flush technique

The number of QDs in a sample can be increased by having multiple layers of them. In order to obtain uniform layers in a stack, a technique called the indium flush can be applied during growth. Figure 2.10 demonstrates the effects of the indium flush on the QD energy levels. During the indium flush, the growth is interrupted and the substrate temperature rapidly raised to ~610°C to eliminate any indium from the growth front. The wafer temperature can then be ramped back to the lower QD growth temperature for the case of stacks with multiple layers, or kept at the higher temperature during the completion of the GaAs cap. For the indium flush executed after, between 2.5 and ~5.5 nm, the QDs can be continuously adjusted from having a more disk-like shape to the more standard lens shape (see figure 2.10a and 2.10b).

In the case of stacks where the spacer between the QD layers is small enough to lead to vertical self-alignement (<~20 nm),[19,48] but thick enough to have little wave-function coupling between QDs in adjacent layers (>~8 nm), the vertical self-alignment commonly leads to a reduced QD uniformity, and consequently, to larger emission linewidths. This is demonstrated in figure 2.10 for correlated stacks of seven layers separated with 10 nm spacers of GaAs, grown with and without the indium flush. In figure 2.10d for no indium flush, no sharp excited-state transitions can be observed because of the change in the QD size from one layer to the next, as observed from the transmission electron microscopy (TEM) images (figure 2.10a). The uniformity problem with correlated stacks can be circumvented with the indium-flush technique, as illustrated

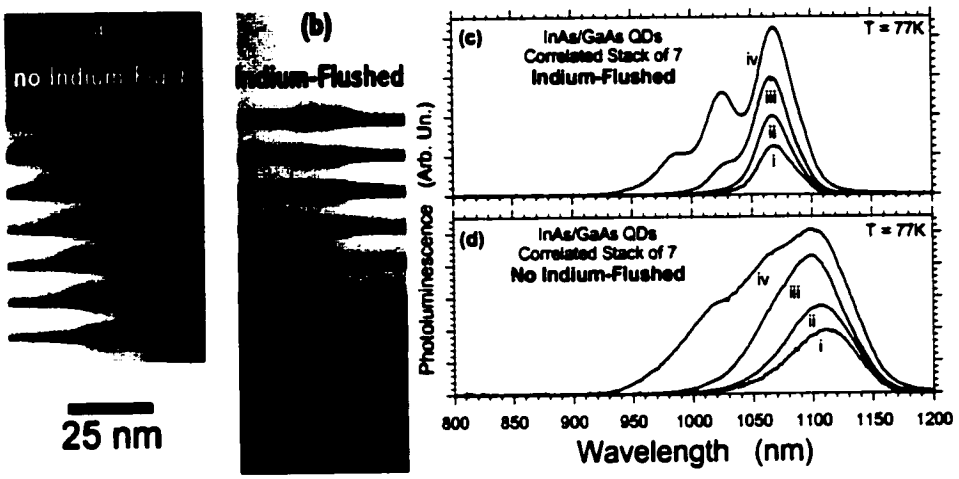

Figure 2.10 Using the indium-flush to make InAs/GaAs QD stacks more uniform: (a) and (b) are cross-section TEM images of shape-engineered InAs/GaAs QDs grown at 515°C, and the corresponding state-filling spectroscopies are in (c) and (d) for stacks of indium-flushed at 5.0 nm (b) and (c) showing better uniformity, and for stacks with no indium flush (a) and (d). The GaAs spacers are 10 nm, and the PL is excited with various intensities up to a few kW/cm^2 (from curve i to iv). From ref. [48].

in figures 2.10b and 2.10c, which is a sample grown under the same conditions but with an indium flush executed at 5.0 nm in the middle of the GaAs barrier. The number of stacked layers can be further increased while preserving the well-resolved electronic shell structure.

Chapter 3

Experimental Techniques

This chapter details the experimental techniques applied. The growth method by MBE is described briefly. This is followed by information on the fabrication and characterization of mesas and mask used to delimitate one or a few QDs. The other sections present the fundamental theory and experimental implementation of the optical characterization employed: PL and EL.

The section on PL starts with a description of a typical macro-PL setup, followed with the additional requirements needed to be satisfied in order to achieve successful measurements using mesas and masks. The section concludes with a description and discussion on micro-PL mapping. The chosen technique to obtain maps is by scanning the sample with a laser spot having ~0.8 μm diameter and recording the intensity at a specific wavelength. Imaging of the sample using a white light source helps with the sample positioning. Maps can be obtained at room temperature and at 95 K.

The section on EL describes the experimental setup and the equations used in the laser characterization of chapter 4.

3.1 Sample growth by molecular beam epitaxy

All samples studied here were grown by molecular beam epitaxy (MBE) on GaAs (100) substrate. The basic mechanism in MBE growth of III-V semiconductors consists of a co-evaporation of the constituent molecular species of the epitaxial layer and of dopants on a heated substrate in ultra high vacuum conditions. The ultra high vacuum environment is necessary to maintain the partial pressure of unwanted species as low as possible and ensure collision-free molecular beams from various sources to interact chemically on the substrate surface to form a high purity epitaxial film. A schematic

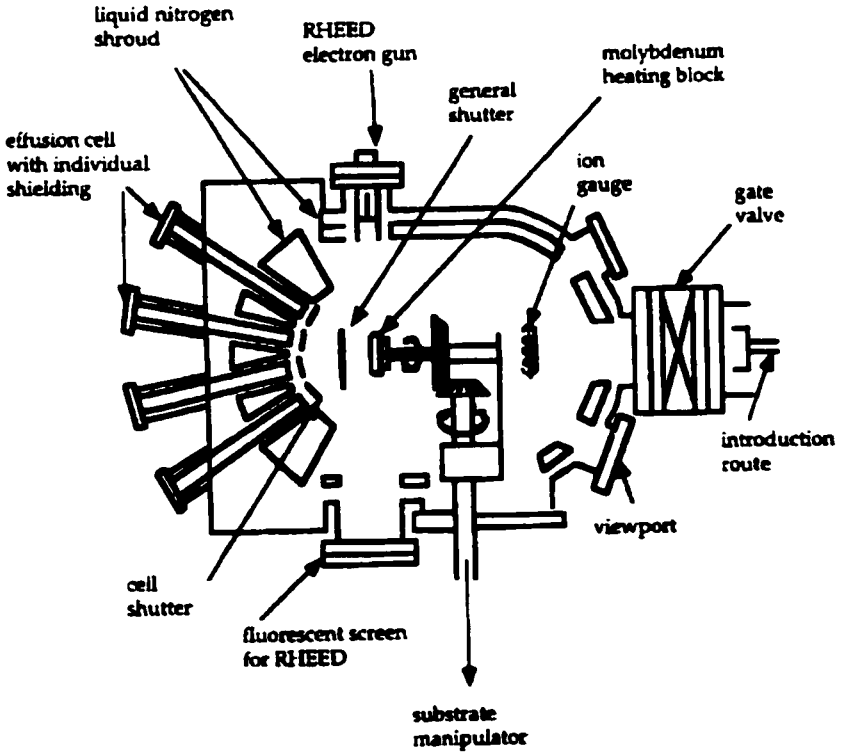

Figure 3.1 Schematic view of a MBE growth chamber. Not shown is the pump which insures ultra-high vacuum. From ref. [112]

diagram of the growth chamber in a conventional MBE machine is shown in figure 3.1.[112]

In MBE, the crystal growth occurs in two steps. First, the incident atoms stick to the crystal then, they move on the surface to the point of incorporation into the crystal. A slow growth rate (~1 μm/h) ensures the dissociation and migration of the impinging species on the crystal surface without incorporation of defects.

All growths were done in modified V80H VG-Semicon MBE systems with metallic In, Ga, and Al, as well as a solid As source set to produce As_2, as source materials. The dopants used were Si for n-type and Be for p-type doping. The group IV element Si is primarily incorporated on group III sites. The doping level is proportional to the dopant arrival rate. Unless stated otherwise, the samples were grown at the National Research Council (NRC) Canada by Dr. Simon Fafard.

The substrates were (001)-oriented GaAs. They were semi-insulating for the single and coupled QD samples, and in the case of laser structures, the substrates were n-doped. Before growth, the substrates werethermally cleaned by heating them at 500°C in vacuum for one hour. This was followed by heating at about 670°C for ten minutes under arsenic pressure to remove any oxide on the surface. The arsenic pressure in the chamber during the growth was around 2×10^{-7} Torr. The Stranski-Krastanow growth mode was used to produce between one and eleven layers of QDs in each sample. Details of the different growths will be given at the beginning of their respective chapters. The GaAs and AlGaAs layers were grown in the 630 to 660°C range, this range gives good material quality, i.e. free from deep level defects while limiting the desorption of gallium from the surface. Since indium desorption occurs at temperatures ~150 °C below that of gallium, the InAs and InAlAs layers where grown in the 510 to 530°C range. The temperatures

were measured with a calibrated optical pyrometer. The deposition rate for GaAs was ~0.2 nm/sec, this rate increased to ~0.3 nm/sec for AlGaAs. In order to allow good control of the amount deposited for the QDs, the growth rate was reduced to 0.02 nm/sec for strained InAs layers and 0.031 nm/s for strained $In_{0.64}Al_{0.36}As$ layers.

3.2 Design and fabrication of mesas and masks

3.2.1 Mesas

When probing QDs using PL, a simple way to increase spatial resolution is to use a mask on the sample with submicron-sized holes, or to etch away most of the semiconductor material and leave submicron sized mesas. This approach has a disadvantage in the lack of control of the positions of the holes or mesa, with respect to features of interest in the sample. However, there are no effect of drift and no ambiguity as to the position of excitation. It is also possible to return to the same spot for further measurements.

The mesas were obtained through lithographic techniques. Figure 3.2 shows the different steps used to obtain the mesas on the sample. In the first step, a 100 nm thick layer of polymethylmetacrylate (PMMA) is spun on the surface of the sample, this organic material acts as a positive resist layer.[113,114] In the second step, the sample is placed in a scanning electron microscope (SEM), and the resist is then selectively exposed to an electron beam. The SEM is interfaced to an external pattern generator, which was used to expose arrays of squares of varying dimensions as shown in step three.

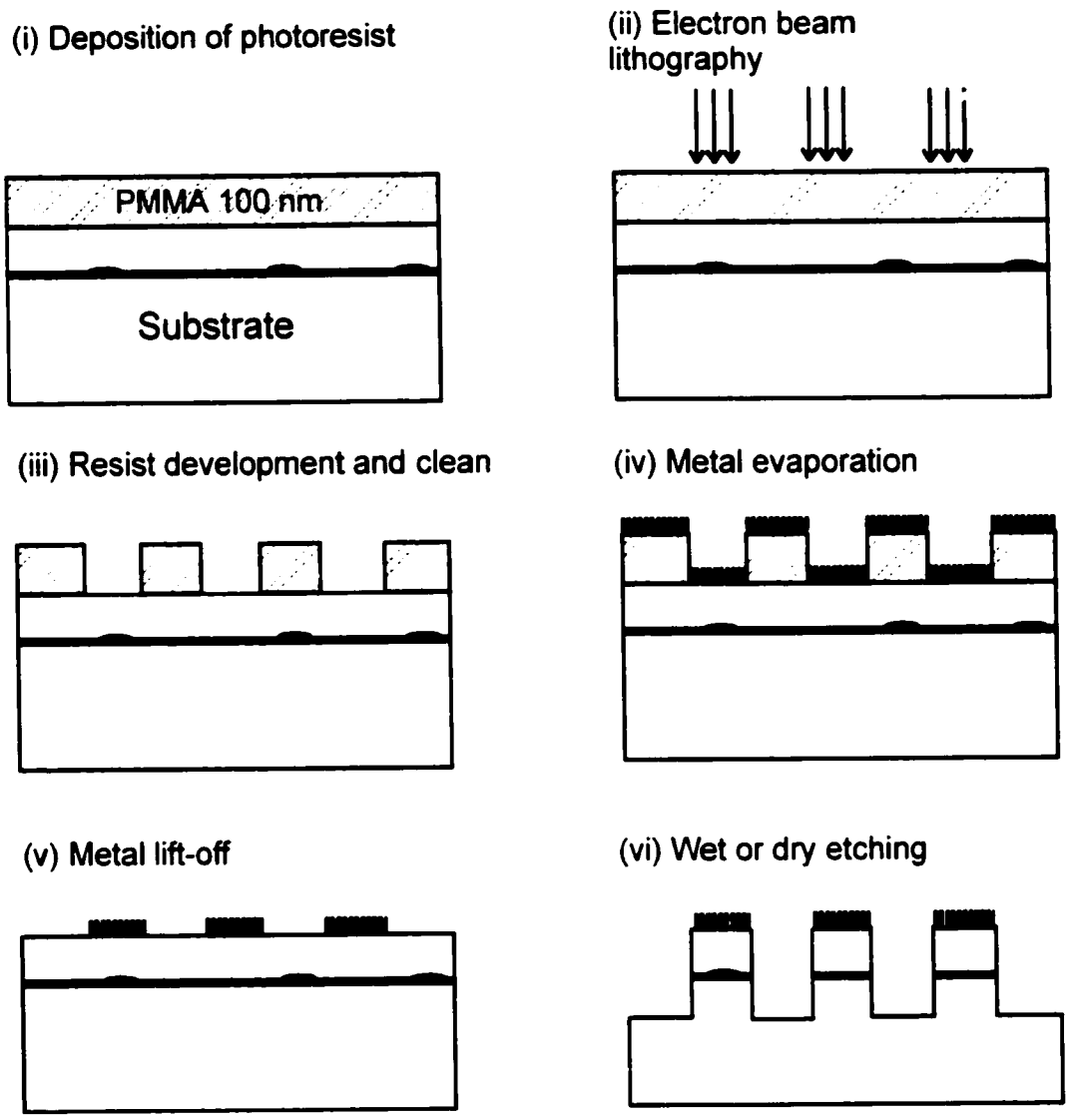

Figure 3.2 Steps to fabricate mesas using electron beam lithography.

This is followed by thermal evaporation of 10 nm of aluminium which acts as etching masks. In step five, the PMMA, and the metal covering it, are lifted-off using acetone. The last step defines the mesas and consists of using an isotropically etching H_3PO_4:H_2O_2:CH_3OH solution that will etch away a certain thickness of material except the material located below the metal masks. This type of etch has been shown to leave

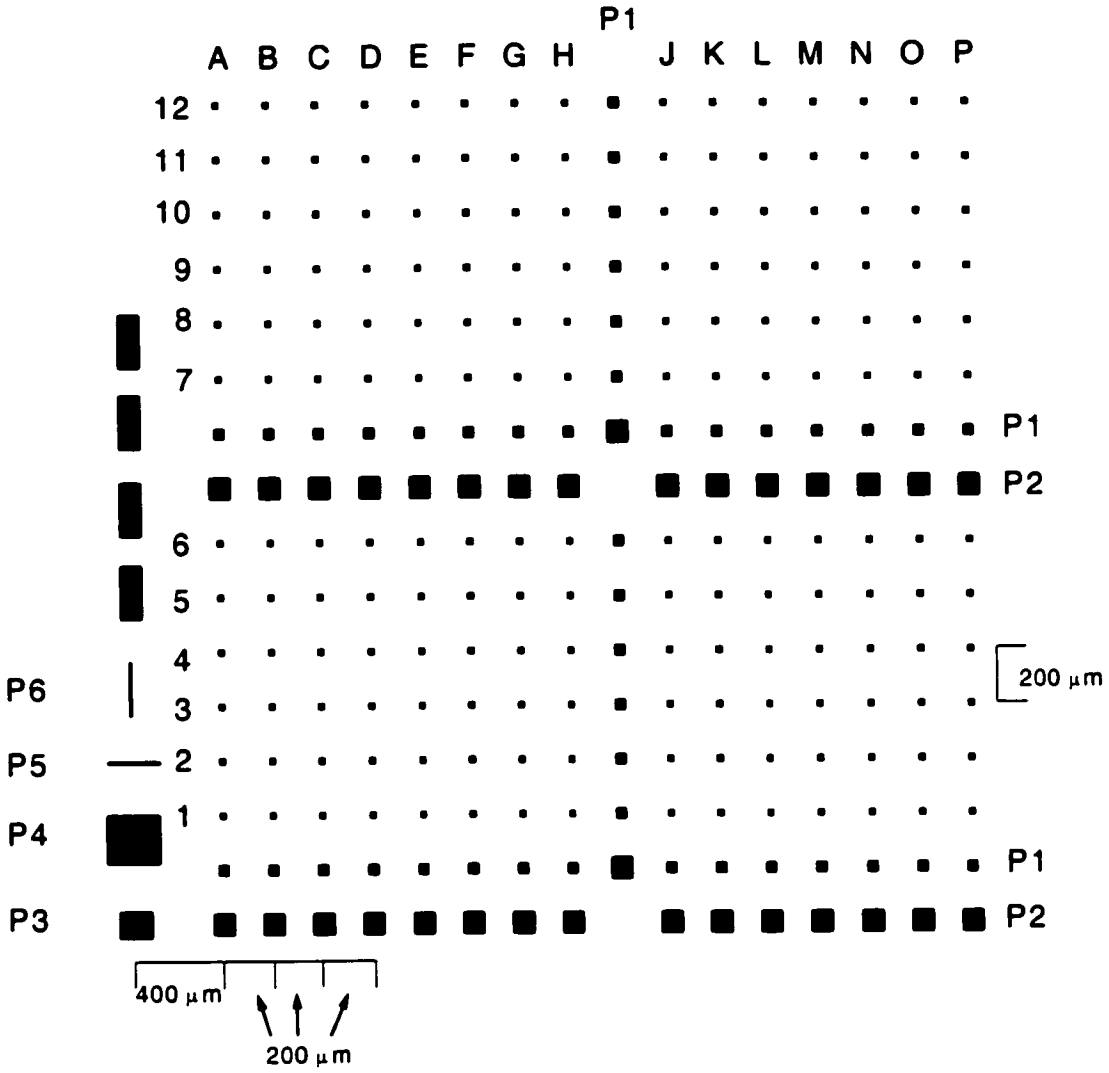

Figure 3.3 Mesa pattern etched on samples for single QD spectroscopy.

smooth surfaces and sidewalls so that the QD luminescence remains high.[115]

Figure 3.3 shows an example of a map of the etched pattern which was used on some of the samples.[114] The dark areas represent the parts of the sample that have been left unetched. The different mesas are spaced 200 µm one from another. Large reference mesas were named P1 to P6. The P1 and P2 type are numerous and are placed in a well defined order along the smaller mesas located in columns A to O, and rows 1 to 12. All the mesas located in a particular column have the same dimensions, and the sizes of the

mesas diminish from A to O (see table 3.1 for the dimensions).

Mesa type	Mesa dimensions (μm)		Mesa type	Lateral dimensions of the aluminium squares on top of the mesas (nm)
P1	5 x 5		A	600
P2	20 x 20		B	400
P3	40 x 40		C	304
P4	100 x 100		D	272
P5	100 x 10		E	256
P6	10 x 100		F	240
			G	224
			H	208
			I	
			J	192
			K	176
			L	160
			M	144
			N	128
			O	112

Table 3.1 Mesa sizes.

Figure 3.4 displays SEM micrographs of some of the resultant mesas. The top 10 nm of each mesa is the thin metal deposited during lithography, below that one observes the curved and smooth sidewalls characteristic of wet etching. The thin metal film will at most transmit 10% of the incident light since Al has an absorption coefficient $\alpha \sim 1 \times 10^5$ cm^{-1} in the near infrared, this should not significantly affect the PL excitation and collection. The curved walls do not have much effect on the size of larger mesas as shown in figure 3.4a, but for smaller mesas such as the ones shown in figure 3.4b and

3.4c, this reduces the semiconductor area compared with the dimensions stated in table 3.1. As shown in the SEM, the samples have been etched ~150 nm deep. The QDs are located 100 nm from the top surface so this positions the WL and possible QDs at one-third the total height of the mesa, where the arrow points in figure 3.4c. For the mesa shown in figure 3.4c, we measure a side length of ~200 nm for the mesa at the height of

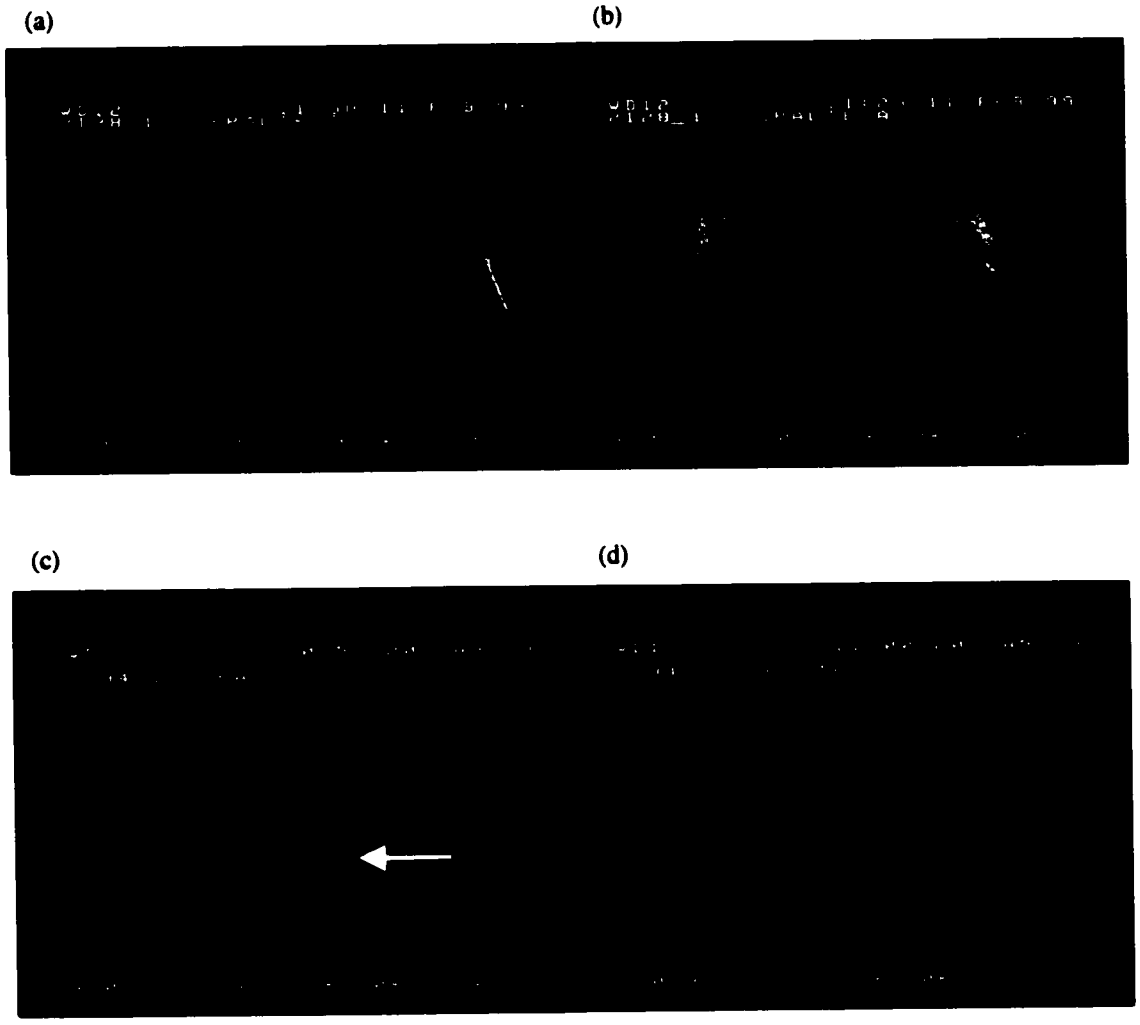

Figure 3.4 Scanning electron micrographs of the mesa structures. On the top of each structure is the 10 nm thick aluminium mask, below is the remaining semiconductor material. (a) shows a P1 structure, (b) is a mesa from column A of sample 2128, (c) and (d) are a mesa from column C and column G of sample 2134, respectively. The strained layer is located where the arrow points in (c). Etching and SEM pictures by M. Emmerling, Universität Würzburg.

the strained layer, the top mask measures 300 nm in side length. For a mesa of type H, the sidewall width is ~100 nm, while the top mask measures 300 nm. In the rest of the text, the measured mesa sizes at the strained layer level will be used.

3.2.2 Masks

An example of masks deposited on transparent substrates is shown below. This

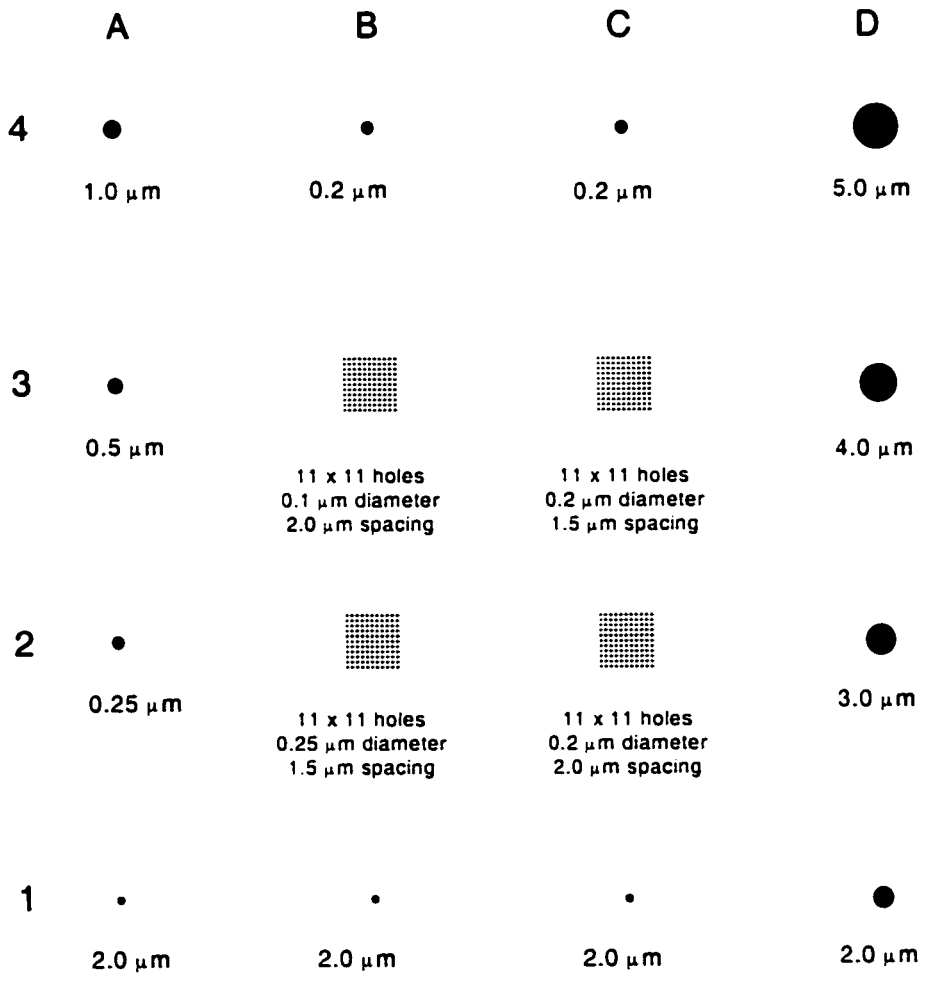

Figure 3.5 Nanomask pattern shown with the substrate on top and the pattern in metal underneath. Holes vary from columns A to D, and rows 1 to 4. The sizes indicated below the holes represent the diameters. The holes are spaced 150 μm one from another unless stated otherwise.

technique allowed us to reuse the mask on many samples. A film of 20-nm thick titanium and 100-nm thick gold was deposited on the substrate surface in which a large number of holes with sizes between 5.0 μm and 0.1 μm were made using electron beam lithography, metallization, and lift-off. Three masks were made this way, they all have the same basic pattern shown in figure 3.5. This pattern is 450 μm x 450 μm, and for the first mask, it was repeated 8 x 8 times; the repeats are spaced every 600 μm. This mask and the one that followed where done on 500-μm thick quartz. The second mask had the pattern repeat 9 x 9 times and large 550 μm long and 25 μm wide windows separated by 150 μm were added as reference along the mask, they were spaced 500 μm from the patterns. The third mask was made on a 125 μm thick glass substrate so that focussing on the QD sample could be done with a lens having a shorter focal length. The pattern shown in figure 3.5 was repeated 11 x 11 times. Figure 3.6 shows SEM micrographs of mask 2 with the metal layer on top. Figure 3.6a shows a C3 ensemble of very small windows, were they are all open except for five of them. Figure 3.6b displays a B3 ensemble of windows where all the holes are open but for many the lift-off procedure left the gold very near its respective hole. For these very small windows, the holes are not completely symmetric but they have the right dimensions.

Unfortunately none of the experiments using the rigid mask technique resulted in the observation of single QD spectra. A challenge with these windows is that at higher pump intensities, not just the QDs within the window opening are excited, but other QDs located below the metal and very close to the window are excited as well and can contribute to the spectrum. This cannot happen with spectroscopy on mesas.

(a)

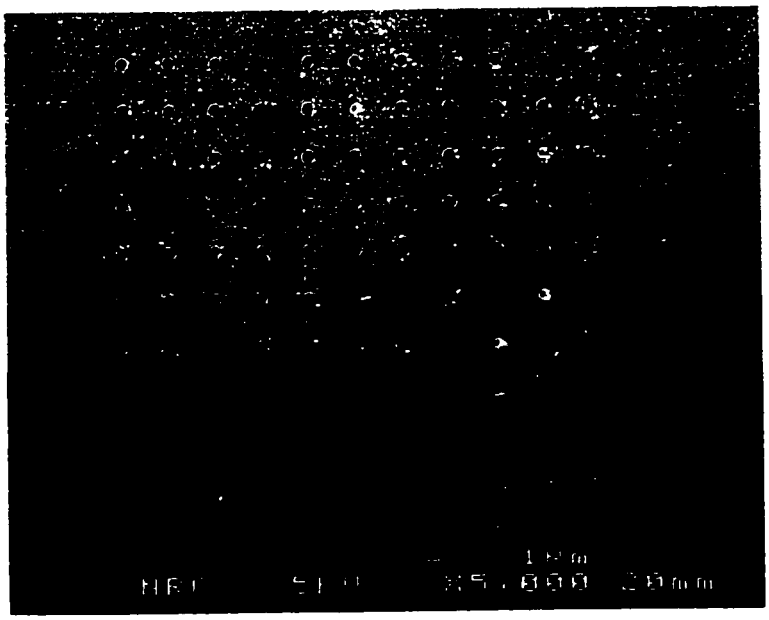

(b)

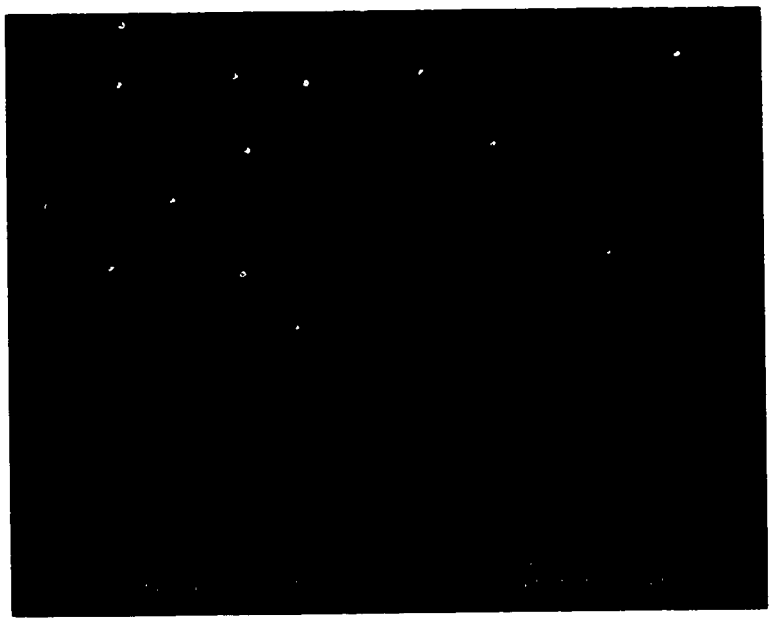

Figure 3.6 Scanning electon micrographs of holes in a mask. In (a) is shown a series of round holes 200 nm in diameter separated by 1.5 μm one from another, in (b) is shown a series of round holes of 100 nm diameter separated by 2 μm one from another. Masks and SEM pictures by J. Lapointe, NRC.

3.3 Photoluminescence

PL is the process by which a material emits a photon after recombination of thermalized photo-created electron-hole pairs. According to the selection rules presented in chapter 2, if an electron is in the conduction band, it can recombine with a hole state in the valence band. If enough recombination events occur in a given layer, important information can be obtained by mapping the luminescence intensity as a function of energy (or wavelength).

3.3.1 Macro-photoluminescence

Figure 3.7a shows a schematic of a modern PL set-up. Under the perturbation caused by the impinging light beam (usually a laser), the sample produces luminescence that is collected and steered to the entrance slit of a spectrometer. The light spectrum is then dispersed by a grating and each wavelength is subsequently focused onto a different position on the detector surface. If the detector is position sensitive, a spectrum is acquired in parallel by simply feeding the intensity detected as a function of position to a computer, this is called parallel detection PL. If the detector is position insensitive, an exit slit is used to select a narrow wavelength range. The intensity of emission at this wavelength is measured and fed to a computer. The gratings of the spectrometer are then rotated to select a new wavelength and the process is repeated until the desired spectrum is obtained. This type of PL experiment is called scanning spectrometer PL.

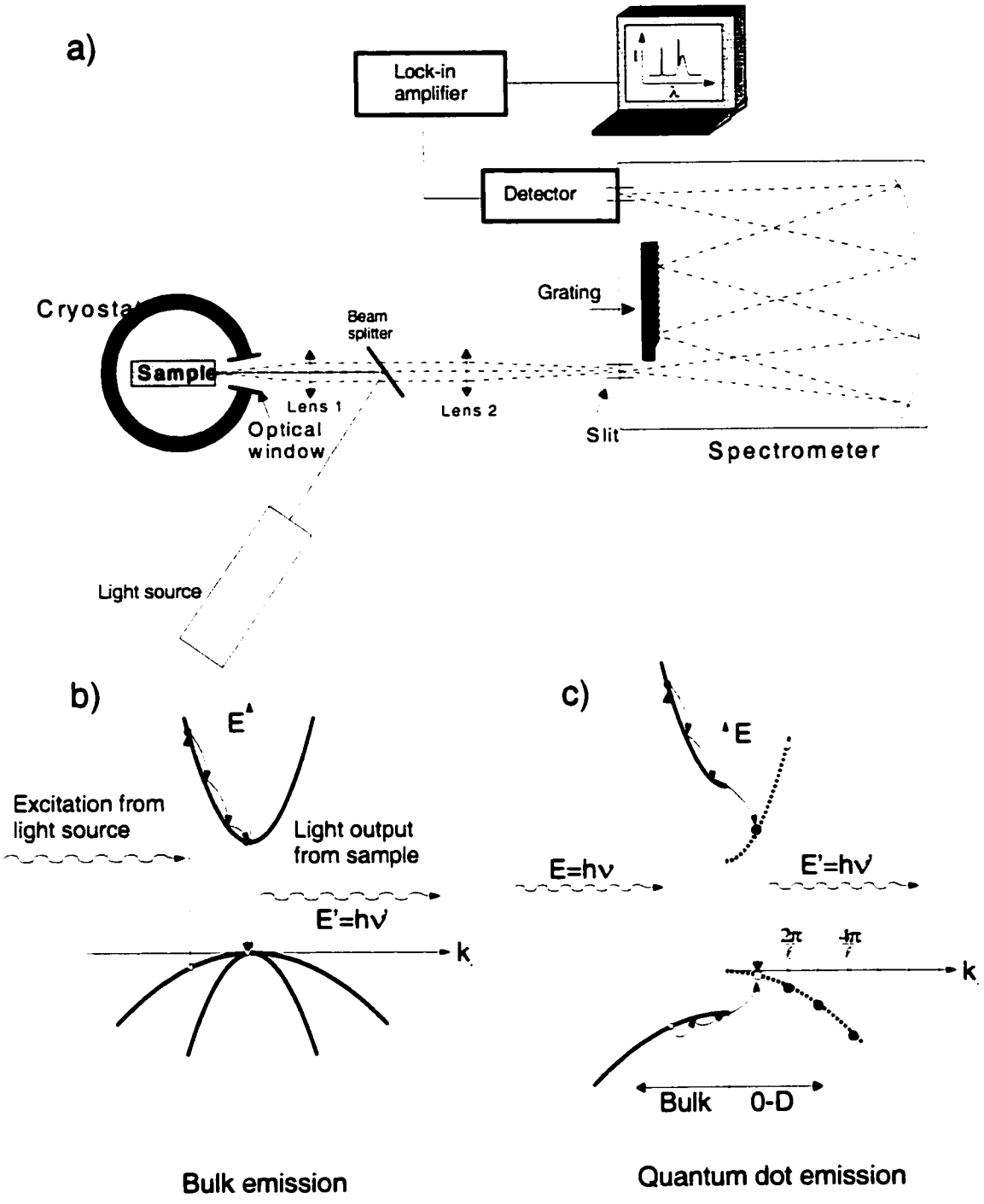

Figure 3.7 Standard far-field PL experiment. (a) Experimental layout of a PL setup. (b) and (c) Bulk and QD sample reaction under the action of the excitation source.

Figure 3.7b shows, in k-space, the series of events triggered by the absorption of a

photon in a bulk structure. First, an electron is promoted to the conduction band at the instant of absorption. If the energy of the photon absorbed is higher than the bandgap, the electrons and holes are created with some excess kinetic energy, they will relax to the band edge by optical phonon emission, and/or carrier energy transfer and subsequently recombine radiatively to emit a photon of lower energy.[116] The resultant spectrum will show an emission line at an energy roughly equal to the bandgap with a FWHM strongly dependent on temperature and excitation intensity because of the continuous dispersion relationship.

In a QD sample, for non-resonant excitation, the carriers are created in the barrier material, usually a bulk structure. The carriers diffuse near a QD; at this point they must relax from a continuum to the discrete states of the QD. Figure 3.2c shows in k-space the course of events produced by non-resonant excitation in a QD sample. The luminescence resulting from transitions between discrete energy states should have an extremely narrow linewidth.

The typical apparatus for routine sample characterisation consisted of a liquid nitrogen-cooled optical cryostat for measurements at T = 77 K. The 532 nm line of a Millennia V Nd:YVO_4 laser by Spectra-Physics was used as the excitation source, the light beam was then modulated by a chopper, and focussed to a circular spot on the sample surface with a diameter of 50 μm. The spot size and shape was verified using an imaging CCD camera system. A CVI DK240 ¼-m double-grating monochromator equipped with 600-(or 1200) grooves/mm gratings dispersed the light onto a Hamamatsu

636 photomultiplier tube for detection between 200-950 nm, or a EO-817L North Coast Scientific nitrogen-cooled Ge photodetector for detection between 700-1800 nm. This spectrometer has a dispersion of 3.2 nm/mm for the 600 grooves/mm gratings and a dispersion of 1.6 nm/mm for the 1200 grooves/mm gratings. The slits where usually open to a width of 1 mm. The detected signal is then amplified with the help of a Stanford Research Systems SR810 DSP lock-in amplifier. The uncertainty of the detected signal can be determined by evaluating the intensity changes in a part of the spectrum that has no features.

3.3.2 Photoluminescence using mesas and masks

To isolate a single QD, small mesas and masks were fabricated by electron beam lithography and wet chemical etching on an unpatterned sample as described earlier. The lateral sizes of the mesas and mask holes ranged from 100 μm down to 100 nm. The samples were optically probed with the 488 nm line of a cw Stabilite 2016 Ar^+ laser by Spectra-Physics. In order to reduce the probe spot size, the laser beam was first expanded up to ~1 cm in diameter, and than focussed down to a diameter of ~20 μm, since the focussed spot diameter is inversely proportional to the collimated beam diameter.[117] This last focus lens was mounted on a set of x-y-z translation stages in order for the laser beam to travel across the sample located in the cryostat. To reduce sample heating under optical excitation, the structures were held in superfluid helium at about 1.2 K in an optical cryostat. A filter reflecting the laser line is placed before the spectrometer. The sample emission was dispersed by a double monochromator (f = 0.6 m), measurements where

done with a 600 grooves/mm grating using the second or third order of dispersion and detected with a Instruments SA Spectrum One LN_2-cooled Si CCD camera for 60 s accumulation times. For magneto-optical measurements, the sample was placed into a top loading cryostat with optical windows and superconducting magnets provided fields from 0 to 8 T. The magnetic field was aligned in the growth direction. The polarization of the luminescence was analyzed using a quarter-wave retarder and a linear polarizer.

When performing the PL experiments using mesas, one starts with the P3 to P6 mesas described in section 3.2. The 20 μm laser spot can be easily placed over one of these mesas to obtain a large signal, then by moving the focus lens using the translation stages, one can move the probe beam from one mesa to the next. The P1 and P2 mesas are used as reference positions and an excited P2 mesa emits a factor ~15 higher than a P1 mesa. Then at probe intensities ~10 times higher than the recorded spectra shown in chapters 5 and 6, one scans the various smaller mesas for a PL signal originating from QDs with 1-2 s accumulation time on the CCD. When a mesa of interest is found, state filling measurements are done for that mesa.

When performing PL experiments using a mask, the mask is glued with the metal side facing the unetched samples, this way the holes in the metal are directly over the sample and the incoming laser light is not allowed to diverge before reaching the sample. Similarly to the case of the mesas, the larger holes are used as reference points, from there one scans the various smaller windows for signal. The sets of small holes located very close to one another (1 μm) could not be used in this experiment.

Spatial stability is extremely important in this type of measurement, and unfortunately, after 60 s accumulation times, the focus lens usually had to be readjusted.

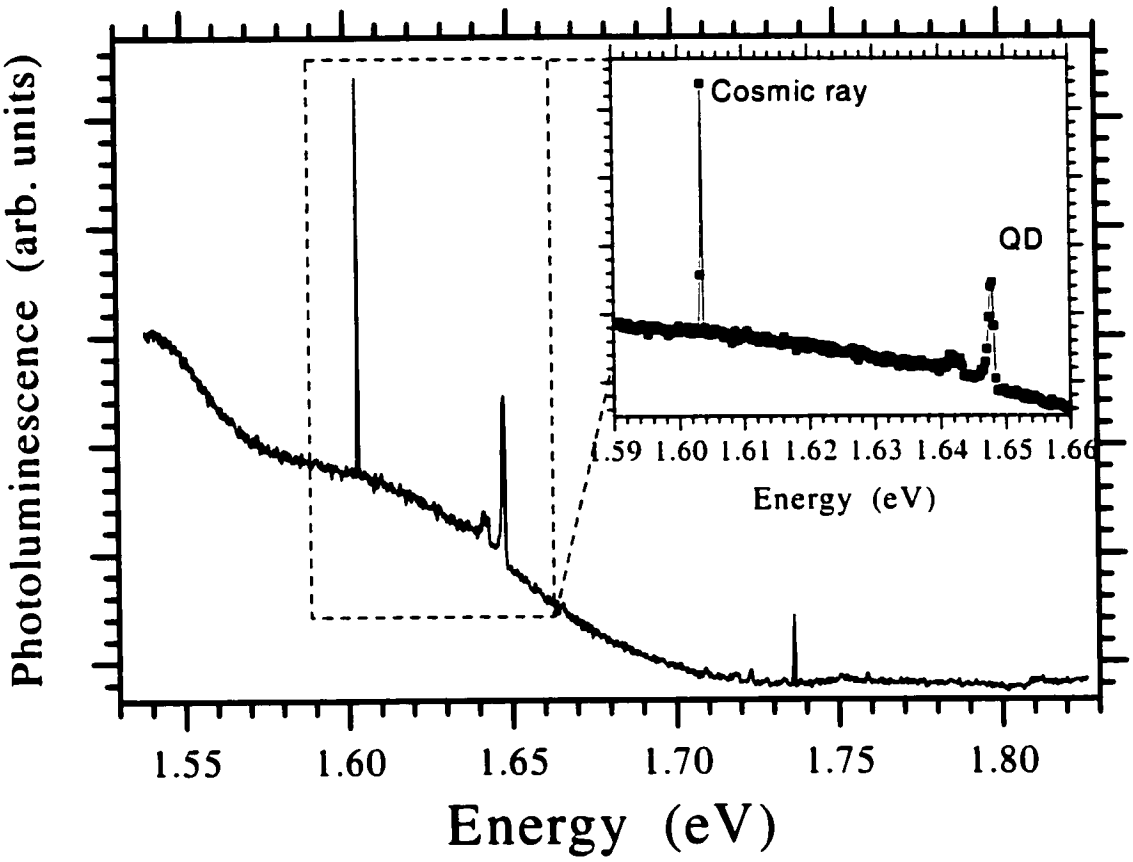

Figure 3.8 Example of a PL spectrum obtained on a small mesa with 60s accumulation on the CCD. Two cosmic rays are present in the spectrum, one at 1.603 eV and another at 1.737 eV. A single QD emitting two lines is observed at 1.64 eV. An area of interest has been blown-up on the right.

This was mainly due to small oscillations of the 1-m long tail of the cryostat caused by air currents from the ventilation system and vibrations of the building.

The spectrometer and CCD detector are calibrated before use with a HeNe laser emitting at 632.8 nm. When the slits are at 100 μm, the resolution is better than three pixels. Figure 3.8 shows a PL spectrum taken from a small mesa with one InAlAs QD in AlGaAs. The CCD detector has 1024 channels, therefore each pixel represents 0.3 μeV in the case of the spectra shown. When accumulation data using the CCD detector additional features can appear in the spectra due to detection of cosmic rays. This is usually not a problem since they cause highly localized spikes in the detector and can be removed

during acquisition using software. But since they are confined to 1-4 pixels, they could be mistaken with emission of single QDs. In the inset of figure 3.8, one observes a peak 2 pixels wide on the left at 1.603 eV and a 7-pixel wide peak on the right at 1.647 eV. The left peak originates from a cosmic ray, while the right peak originates from a single QD; the QD peak is a few pixels wider. Another way to recognize a cosmic ray is that the event is extremely unlikely to occur during acquisition of a second spectra at the same pixel position with the same intensity. The cosmic ray peaks present in the data collected were subsequently removed during analysis. Another problem during data collection occurs when the PL probe laser is an Ar^+ laser. This laser emits very faint plasma discharge lines in the 650-750 nm range that are usually lost in the noise when performing PL on a large amount of QDs. When observing a few to a single QD, these lines where detected by the sensitive CCD. Because they always occur at the same energies, they can be removed during analysis afterwards. This problem is easily solved by adding a band pass (interferential) filter in the laser beam's path that only lets the 488 ± 10 nm line through.

3.3.3 Micro-photoluminescence mapping

One of the most direct ways to obtain local luminescence in the form of a spot-mode spectra and intensity maps is by spatially resolved PL. This technique is simple and straightforward, the resolution however is limited to ~1 μm in III-V semiconductors.[118] The resolution is determined by the size of the excitation spot and by exciton diffusion. There are mainly two ways of obtaining maps of the luminescence, either by direct

imaging[119] or by scanning either the excitation spot or the sample.[120,121] The highest spectral resolution is obtained using the scanning method.

The simplest is to focus the excitation source on the sample and to record the intensity at a specific wavelength (or a complete spectrum) as a function of excitation position. The positioning is done by keeping the excitation position fixed and scanning the sample. This is combined with a reflectivity setup as well as a white light imaging system with a CCD/video camera. The excitation source is a laser that is introduced into the parallel beam path of the microscope objective by a beam splitter for local excitation. There are several possible excitation sources: An Ar^+ laser (457.9, 488 and 514 nm), a Nd:YVO_4 laser (532 nm), a tunable Ti:sapphire (from 700 nm to 950 nm), and a HeNe laser (632.8 nm). The emission is detected by a photomultiplier tube, a CCD camera or a Ge detector.

The room-temperature scanning setup is shown in figure 3.9. The sample imaging is done using an Oriel tungsten-halogen source. The white light is collimated using lens 3, and than almost focussed using lens 1. The slightly defocussed spot illuminates a small area of the sample. The white light reflected off the sample is captured by lens 1 which has a 10 X to 60 X magnification, the almost collimated beam is then directed to a Panasonic BD400 CCD camera and screen. When using a 60 X objective for lens 1, the on screen magnification is ~1 x 10^4.

Reflectivity measurements are done using the focussed spot of the 488 nm line of an Ar^+ laser. The reflected beam is directed to a grating and a UTD Si detector is positioned to detect 488 nm in the first order of diffraction. The signal is than amplified using an EG&G Princeton 5210 lock-in amplifier. Calibration is done using a GaAs

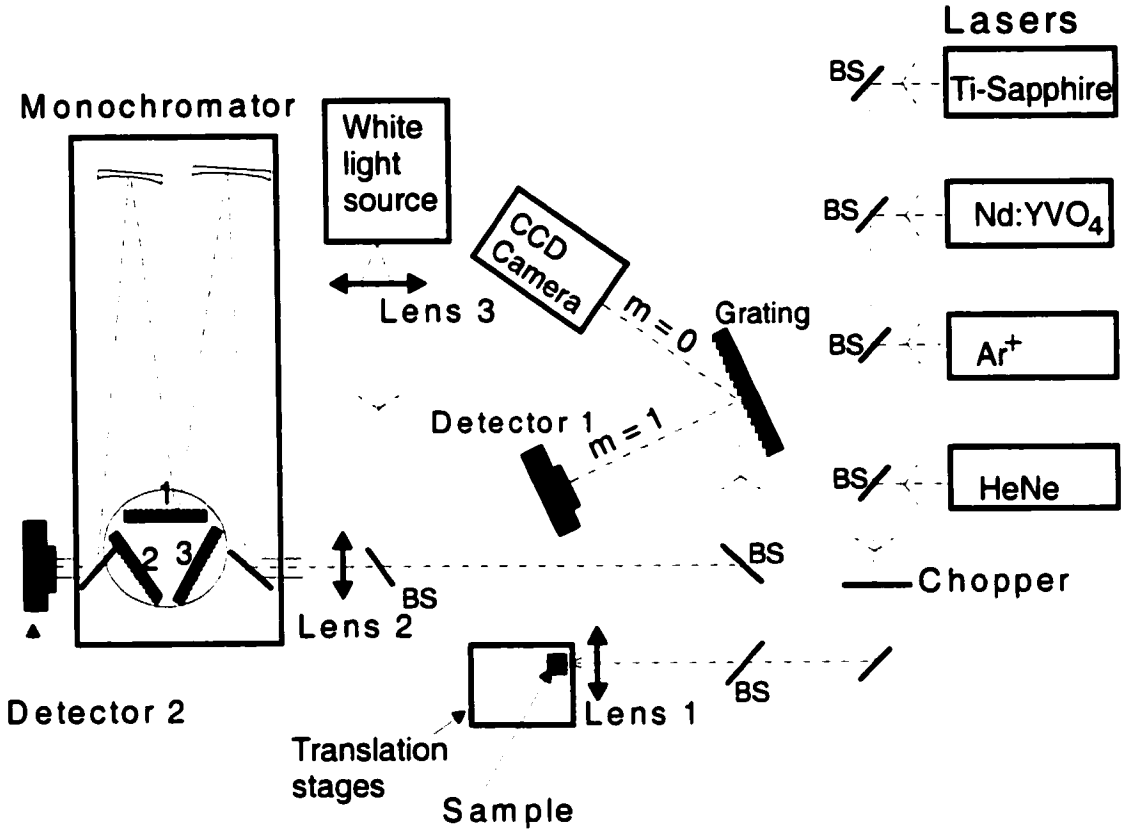

Figure 3.9 Room-temperature scanning micro-PL setup. Beamsplitters are represented by BS.

sample.

In micro-PL measurements, the laser spot is focussed using a microscope lens, the most often used being a Newport M - 60 X microscope objective with a 2.9 mm focal length, a numerical aperture of 0.80 and a working distance of 0.3 mm. The numerical aperture (NA) for small cones of light can be written as:

$$\mathrm{NA} \approx 2f/\# = \frac{D}{F}, \tag{3-1}$$

where $f/\#$ is the f-number of the system, F is the len's focal length, and D is the beam diameter. The focussed spot as observed on the CCD camera is ~0.8 μm in diameter. The light emitted from the sample is collected by the same lens and is collimated to lens 2

which is then focussed at the entrance split of a CVI DK480 ½-m single-grating monochromator. The monochromator has a three-grating turret with automatic grating change. Grating 1 has 1200 grooves/mm blazed at 500 nm, grating 2 has 600 grooves/mm blazed at 1000 nm, and grating 3 has 150 grooves/mm blazed at 500 nm. One of these gratings disperses the light onto a Hamamatsu 636 photomultiplier tube for detection between 200-950 nm, a EO-817L North Coast Scientific nitrogen-cooled Ge photodiode for detection between 700-1800 nm, or a Spec-10:100B CCD detector by Princeton Instruments for detection between 200-1100 nm. The liquid-nitrogen cooled CCD has a 1340 x 400 imaging array with 20 μm x 20 μm pixels.

The samples are mounted on a high-precision 3-axis piezoelectric translation stage. For room-temperature measurements, the samples were mounted on a Melles-Griot N17 ANC series NanoBlock 3 axis scanning stage. This piezo-flexure stage offers 20 μm scanning in the x-y-z directions with manual adjustements over 4 mm on all axes. A Melles Griot 17 PCZ piezoelectric controller with feedback controls the piezoelectric actuators with a resolution of 5 nm. The piezoelectric scanning is voltage controlled from a computer. Mapping a sample surface can be done using a program written by S. Fafard. This program also collects the data from detectors 1 and 2 of figure 3.9. Figure 3.10 displays an example of scanning micro-PL done on a 1 μm wide mesa from a sample of InAs QDs having 4 MLs barriers of GaAs and bulk $Al_{0.33}Ga_{0.67}As$. The QD ground state for this sample emits at 885 nm at room temperature. The sample was scanned using an ~0.8 μm diameter spot size with 0.1 μm steps over a 4 μm x 4 μm area. Figure 3.10a shows the reflectivity as a function of intensity, on the right is the false color chart where white represents high intensity and black represents low intensity. The lowest reflectivity

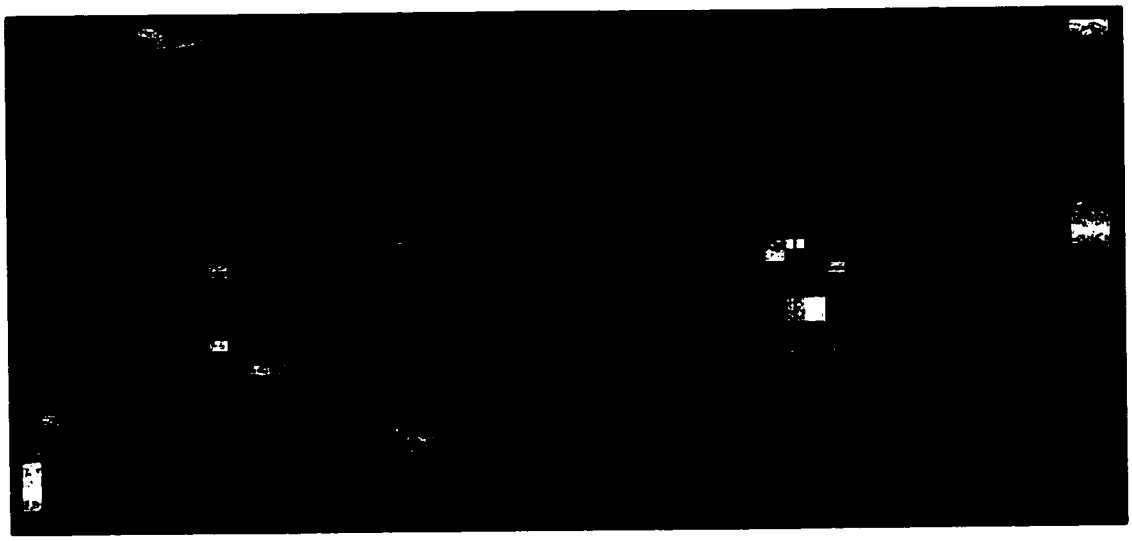

Figure 3.10 (a) Reflectivity and (b) QD emission from a 1 μm long square mesa at room temperature of an InAs/GaAs/$Al_{0.33}Ga_{0.67}As$ QD sample grown on a GaAs wafer (sample 2048) with detection set at 885 nm. One rectangle represents a 1 μm x 1 μm area.

is confined to an ~1 μm^2 area, which corresponds to the position of the mesa when viewed using the white light source imaging. The high reflectivity red-magenta surrounding the mesa is from $Al_{0.33}Ga_{0.67}As$. In figure 3.10b, PL emission at 885 nm is shown, this wavelength represents ground state emission from the QDs. The high intensity white represents localized emission from ~50 QDs contained in the mesa. The surrounding blue-green represents low level detection of the low-energy shoulder of bulk GaAs. For long maps (a few hours), some drift of the sample position can be observed due to changes in room temperature and building vibrations.

In order to perform low temperature measurements, a cryostat was designed to incorporate the NanoBlock as well as a set of stepper motors for larger movement range. The NanoBlock was set on top of a set of x-y-z Melles Griot Nanomover micropositioners having 25-mm travel range in the plane and 20-mm vertically. The

resolution is 10 nm and the accuracy is ± 1 μm. The Nanomovers are operated directly from a personal computer. These positioners can only operate in a limited temperature range and therefore cannot be cooled down. A system employing a copper bellows was designed so that only a small copper plate and the sample would cool down, the rest of the cryostat remains at room temperature. This cryostat is shown in figure 3.11. At ambient pressure, the bellows sits above the copper plate in thermal contact with the nitrogen reservoir located on the top half of the cryostat. As the pressure drops to 1×10^{-3} Torr in the cryostat, so that cooling will take place without condensation, the bellows expands and makes a good thermal contact with the copper plate. When air is allowed in again, the bellows compresses itself to its original dimensions.

In order to incorporate all of these stages, the cryostat is a 32-cm diameter and 34-cm high stainless steel cylinder, with four 2" optical windows positioned 90° one from another. Eight additional windows are placed lower, they are mostly used as electrical connectors and one is for vacuum pump access. Sample temperature is obtained from a platinum resistance temperature detector (RTD) sensor placed next to the sample on the copper plate. The vertical Nanomover would not operate properly when the bellows put its full weight on the copper plate. It was replaced with a DC motor attached to the z-axis differential drive of the NanoBlock stage using a belt. The motor was controlled using a DC power supply.

As shown in figure 3.11b, the focussing lens is also located inside the cryostat. The advantage of having the focussing lens inside the cryostat is to still be able to focus the laser spot down to its diffraction limit, since microscope lenses do not typically have a very long working distance (1 mm or less). The cryostat takes the place of the translation

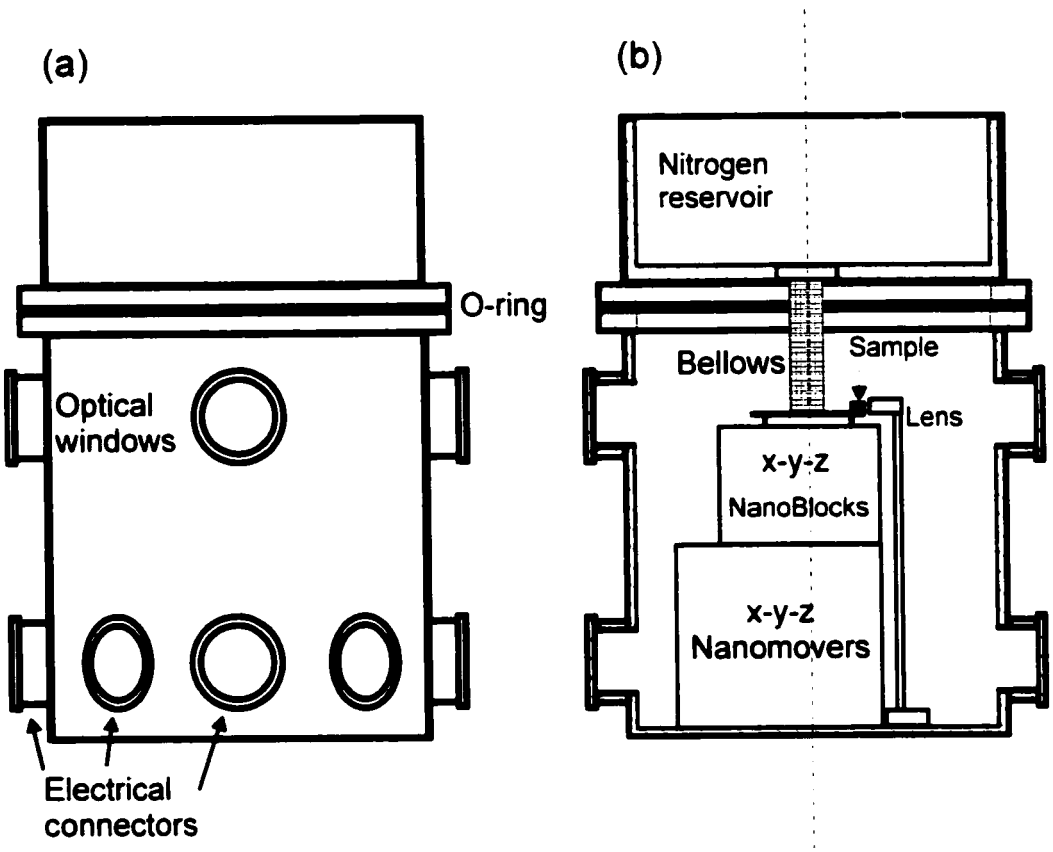

Figure 3.11 Schematic side view of (a) outside, and (b) inside the home made cryostat used for scanning micro-PL.

stages and lens 1 in figure 3.9 for low temperature measurements. This allows for imaging of the sample as well as reflectivity and PL collection at ~95 K.

This system operated well for ~4 hours, after this, condensation took place on the few parts that were at 95 K: the bellows, the copper plate and the sample. This was caused by small residual leaks and some outgassing from the large inner area of the cryostat with many nooks and crannies for humidity to be locked in and released at a later time, combined with the small amount of parts kept at a cold temperature. As well, the system drifted ~0.2 μm per hour caused by the change in pressure on the bellows as the liquid nitrogen reservoir slowly emptied itself.

3.4 Electroluminescence

In EL, electrons and holes are injected electrically into a sample and emit a photon after recombination. In a QD laser structure, the carriers are injected into the barrier material, and diffuse to the vicinity of the QDs (see figure 3.12). At this point, capture of the carriers occur through phonon emission and/or carrier-carrier (Auger) interaction from a continuum of barrier states, to the WL, and subsequently to the discrete states of the QDs where they eventually recombine radiatively. Band-to-band recombination follows the selection rules stated in chapter 2. The radiation originating from the recombination of carriers can interact with valence electrons and be re-absorbed, or interact with electrons in the conduction band to stimulate an identical photon. When the injected carrier concentration becomes large enough, the stimulated emission can exceed the absorption

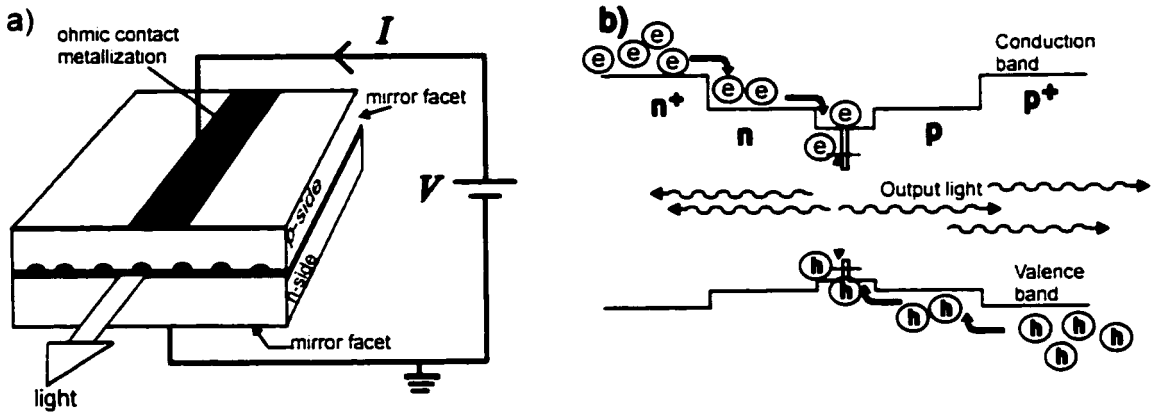

Figure 3.12 Schematics of (a) the geometry and (b) the diagram of the conduction and valence band of a heterostructure laser diode based on self-assembled QDs. The electrons (e and holes (h) are injected in the active region with a forward bias voltage (V) and current (I), they recombine and generate photons.

so that optical gain can occur. In order to sustain stimulated emission, a portion of the radiation must be reflected back to the laser medium. This way, the power gain due to amplification is at least equal to the total losses, including that of the oscillator output.

For the lasers studied here, separate confinement heterostructures are used to provide optical confinement and localized gain. The inner junctions or heterojunctions are used for carrier confinement and the outer heterojunctions are used for optical confinement. In Fabry-Perot laser cavities, cleaved facets act as a pair of reflectors and thus form the resonant cavity. A stripe electrode is used in order to restrict the injected current to a given width.

3.4.1 Experimental setup

Figure 3.13 illustrates an EL set-up. The sample was placed in an optical cryostat that kept its temperature constant and allowed for electrical contacts. Under forward bias, electrons and holes were injected electrically into the semiconductor laser where they recombined in the active region producing photons. The luminescence was collimated and focussed by a lens system into the entrance slit of a spectrometer. The emitted light spectrum was then dispersed by a grating and detected with an appropriate photodetector. The detected signal was digitized and stored in a computer.

The typical apparatus consisted of a liquid nitrogen-cooled optical cryostat for measurements from T = 77 K up to T = 300 K with an uncertainty of + 5 K. The QD lasers were excited using a Hewlett Packard 214B pulsed power supply driven at a

frequency of 100 Hz and having 10 μsec square pulse widths so as not to generate significant heat. Voltages were measured using a Tektronix TDS 320 oscilloscope. At the bottom of figure 3.13 is the electrical circuit employed to measure the potential difference. The samples in the cryostats were mounted on a cold finger in thermal contact with the cooling liquid.

With the liquid nitrogen-cooled cryostat, a double grating 0.5-m CVI Digikrom monochromator was used for light dispersion. For detection from the visible wavelengths up to 1 μm, a United Detector Technology PIN 10D Si photodiode for strong luminescence signals was used, and a Hamamatsu R928 photomultiplier tube for weaker

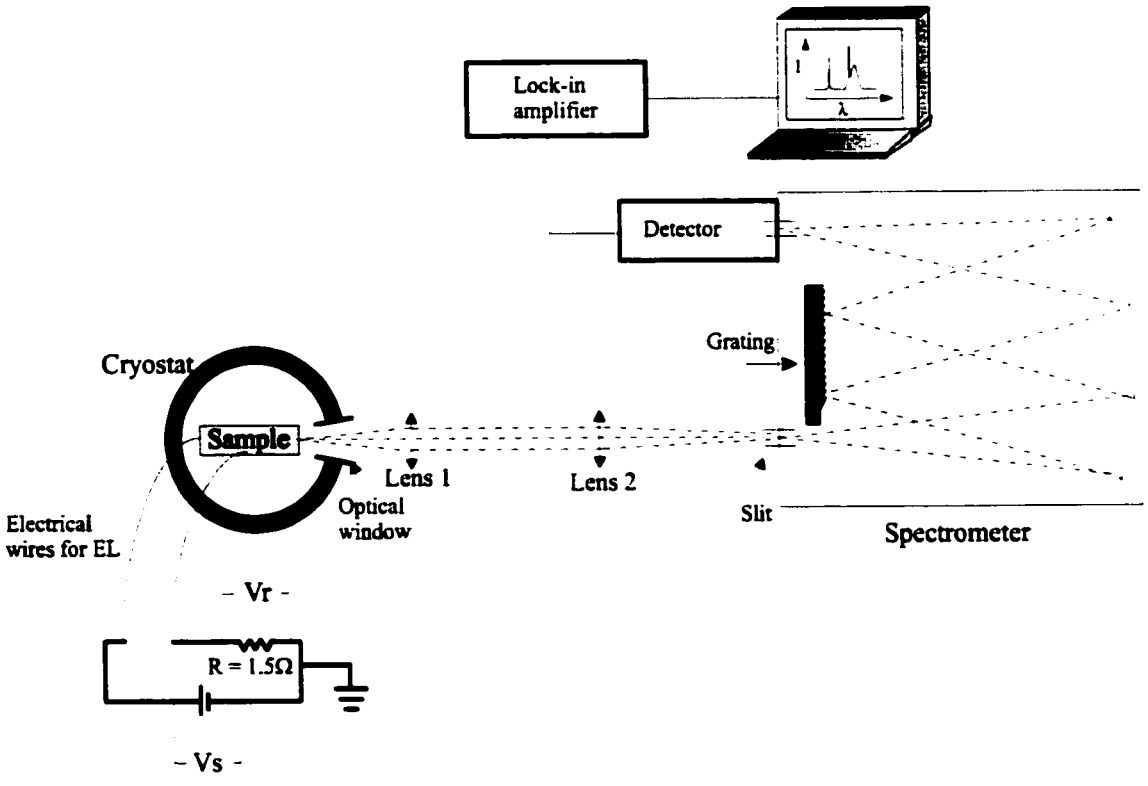

Figure 3.13 Experimental set-up for EL. Shown at the bottom of the figure is the electrical circuit used for powering the QD lasers.

signals. A dispersion of ~ 1.2 nm/mm was obtained with a 1200 grooves/mm grating, giving an energy resolution of 3 meV at 700 nm. A cooled EO-817 North Coast Ge detector was used for detection between 850 nm up to 1.7 μm. For these wavelengths, a dispersion of 2.5 nm/mm was obtained with a 600 grooves/mm grating, giving an energy resolution of 3 meV at 1100nm. The signal was analyzed with the help of a Stanford Research Systems SR810 DSP lock-in amplifier. The uncertainty on the detected signal can be determined by evaluating the intensity changes in a part of the spectrum that has no features. This would correspond to a random uncertainty of 5 % on noisy spectrum for very low injection currents and to values equivalent to the trace width in lasing spectra.

3.4.2 Laser characterization

This section states the equations used for the characterization of laser properties presented in chapter 4.

The electrical input power P_{elec} provided to a laser structure is measured as $P_{elec} = IV_S$. Part of P_{elec} is lost in generating Joule heating in the contact resistance: $P_{heat} = R_s I^2$, where R_s is the contact resistance and I is the current delivered to the device. This resistance can be determined from a linear regression on a current-voltage (I-V) plot just above threshold

$$R_s = \frac{dV_s}{dI} . \tag{3-2}$$

The device external quantum efficiency η_{ext} for stimulated emission is defined as the ratio of the rate of photons leaving from one exit interfaces (P_s) to the rate of carriers crossing

the junction,[122] that is

$$\eta_{ext} = \frac{P}{IV_s} , \tag{3-3}$$

where P is the optical output power from one facet of a laser. When one includes the power losses from the residual contact resistance, the above equation becomes

$$\eta_{ext} = \frac{P}{IV_s - I^2 R_s} . \tag{3-4}$$

For current values above the threshold, many emission lines may be observed in the laser spectrum. These lines belong to the various longitudinal modes of the device, which can be amplified simultaneously. The basic mode selection in the y-direction (longitudinal direction) arises from the requirement that only an integral number m of half-wavelengths fits between the reflection plane. Thus

$$m\lambda = 2L_d n_r , \tag{3-5}$$

where L_d is the device length and n_r is the refractive index. The separation $\Delta\lambda$ between these allowed modes in the y direction is the difference in the wavelengths corresponding to m and $m + 1$. Differentiating the above equation with respect to λ, one obtains

$$\Delta\lambda = \frac{-\lambda^2 \Delta m}{2n_r L_d \left[1-(\lambda/n_r)(\mathrm{d}n_r/\mathrm{d}\lambda)\right]} \tag{3-6}$$

for large m. The term in brackets arises from dispersion.

For the lasing output characteristics of the devices, a Newport 840 optical power meter was placed at the exit window of the cryostat. This allowed the measurement of

the total output power as a function of the current injected into the device. A systematic measurement uncertainty of ~ 10 % arises from a partial light reflection in the cryostat window and from a small clipping of the laser beam due to the large divergence of the laser beam in the growth direction and the relatively small window diameter of the cryostat. This uncertainty is not taken into account in the calculations. The residual contact resistance has an uncertainty of ~ 10 %. This value is obtained from the linear regression of the lasers I-V plots just above lasing threshold. The measurement uncertainty combined with the residual contact uncertainty results in systematic uncertainties of ~ 15 % on external efficiency values. The curve shape is still valid since random uncertainties due to electronic instruments such as oscilloscope, multimeters and power meter are less than 2-3 % total.

The uncertainty on the threshold current density is dominated by a possible current spreading along the lateral direction (x-y) of the metal gate and the effective laser width becomes greater than the actual gate width.[123] This systematic uncertainty can be estimated to be ~ 10 % and is not taken into account in the calculations. The random uncertainty due to electronic instrumentation can be estimated at less than 5 %.

Chapter 4

Zero-dimensional properties of quantum dot lasers

We present results on two material systems. The structures of the samples of these two systems are very similar one to the other. The differences lie in the choice of cladding layer and the materials in the active region, and the fact that the indium flush is used on the InAs/GaAs QDs. The first part treats $In_{0.64}Al_{0.36}As$ QDs in an AlGaAs heterostructure. These lasers emit in the 700-750 nm range,[9,19,124] the red part of the electromagnetic spectrum. Properties specific to QD lasers will be presented such as wavelength tuning and broadband lasing, as well as results on gain. In order to understand the QD energy level structure, results from micro-PL mapping measurements of the laser facet will be shown. The second part of the chapter is dedicated to InAs/GaAs lasers, these emit in the near infrared part of the spectrum (875-1300 nm).[11,13,14,15,16,17,18] By using the Indium flush technique, we obtain uniform self-aligned stacks, this yields well-defined excited state emission. Furthermore, we are able to show wavelength tuning and broadband lasing from QDs. As well, results on threshold current density as a function of cavity length and temperature will be presented.

4.1 AlInAs/AlGaAs quantum dot laser diodes

4.1.1 Sample growth

The Stranski-Krastanow growth mode was used to produce between one and five layers of QDs in the active region of a two-step separate confinement heterostructure (figure 4.1). The structures generally consisted of a thick (~2 μm) $Al_{0.7}Ga_{0.3}As$ contact layer doped $n^+ \sim 6\times10^{17}$ cm^{-3}, followed by a bottom cladding layer of $n \sim 3\times10^{16}$ cm^{-3}

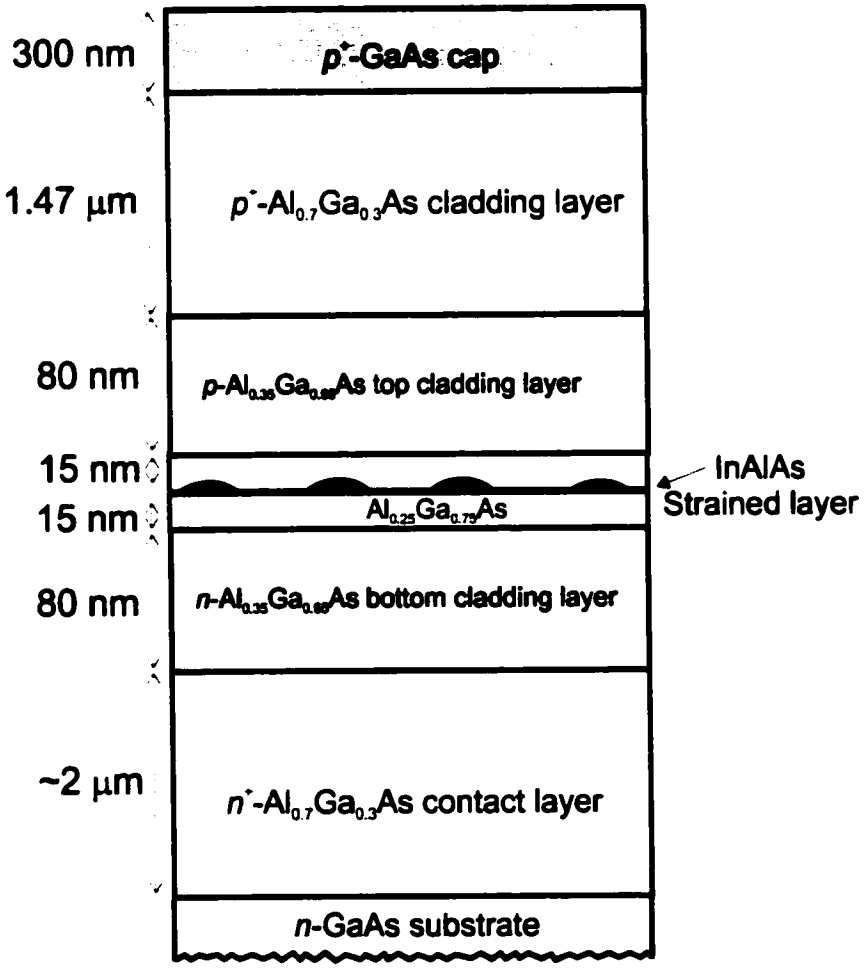

Figure 4.1 Schematic cross-sectional view of sample NT-5, a single layer InAlAs/AlGaAs QD laser

doped $Al_{0.35}Ga_{0.65}As$. The active region is composed of 15 nm undoped $Al_{0.25}Ga_{0.75}As$ barriers on each side of the $In_{0.64}Al_{0.36}As$ QD layer. The active region is followed by a symmetric *p*-doped step-graded cladding and contact layers with corresponding doping and material concentrations follow, and a 300 nm p^+-GaAs cap ($p \sim 3\times10^{19}$ cm^{-3}) terminates the structure. The entire structures were deposited at ~630°C with the exception of the QD section deposited at ~530°C. The growth was interrupted for 150 s after the deposition of the QD layer to allow the QD evolution to reach an equilibrium.[36,103] Some of these samples were grown at BNR (now Nortel Networks) using a V80H VG-Semicon MBE system.

4.1.2 Structural characterization

Figure 4.2b displays the confining potentials for this structure.[68,125,126] The bandgap energies of the different materials contained in the heterostructures are given in table 4.1. It should be noted that the energies are for unstrained materials. The conduction band offsets correspond to ~65% for AlGaAs/GaAs based systems and ~60-70% for InAs/GaAs systems.[127,128,129] The lattice mismatch between $In_{0.64}Al_{0.36}As$ and $Al_{0.25}Ga_{0.75}As$ is ~3.2%;[130] this compressive strain produces a increase in the bandgap compared with unstrained materials. As well, shown in figure 4.2a is the confining potentials for InAs/GaAs based QD lasers. This system has a larger lattice mismatch (~7.1% compressive strain) than for the $In_{0.64}Al_{0.36}As/Al_{0.25}Ga_{0.75}As$ system producing a larger increase in bandgap. The dotted lines show the relative positions of the energy levels.

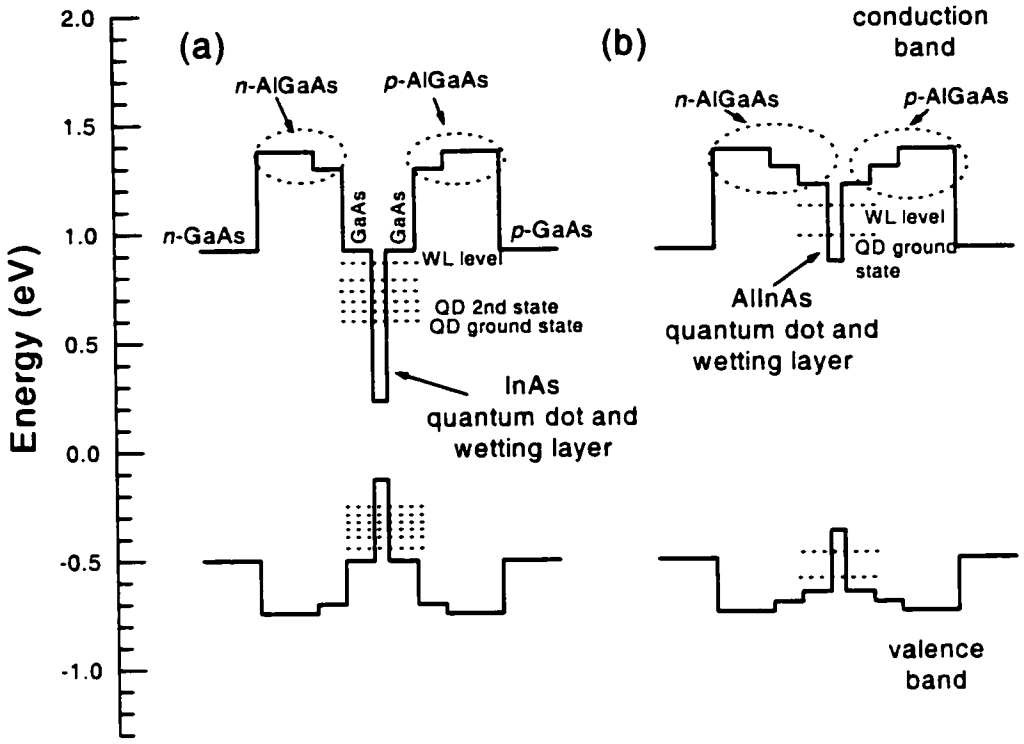

Figure 4.2 Schematic energy band diagram of (a) the InAs/AlGaAs, and (b) the AlInAs/AlGaAs QD laser structures.

Material	Bandgap T = 293 K
$Al_{0.36}In_{0.64}As$	1.24 eV
$Al_{0.25}Ga_{0.75}As$	1.87 eV
$Al_{0.35}Ga_{0.65}As$	2.00 eV
$Al_{0.7}Ga_{0.3}As$	2.12 eV
GaAs	1.424 eV
InAs	0.36 eV

Table 4.1 Material bandgaps at room temperature.

Sample	Description	GaAs spacer layer thickness	Amount of InAlAs deposited	QD density (QDs/μm^2)
NT-5	Single layer of QDs	----------	5.0 ML	>100
NT-1	5 layers of QDs	8.0 nm	4.5 ML	>100

Table 4.2 InAlAs/AlGaAs QD laser samples. The in-plane density of QDs is estimated from TEM cross sections.

Two laser structures of this type will be discussed below, their characteristics are listed in table 4.2. Both samples have high QD densities, although it should be noted here that ~2.0 to 2.5 ML of $In_{0.64}Al_{0.36}As$ has to be deposited before QDs start appearing. No indium-flush was performed on the QDs during growth.

TEM cross-sectional images of the active regions of sample NT-5 and NT-1 are shown in figure 4.3. The images were taken under two-beam (2 0 0) dark-field conditions to maximize the contrast due to chemical compositions. The TEMs reveal a high density of InAlAs islands, and the QDs from the single-layer sample have a base diameter of ~20 nm and thickness of ~5.0 nm. These structural characteristics are comparable to the ones obtained with similar self-assembled QDs where other optical studies were performed.[131] Sample NT-1, the five-layer sample, shows vertical alignement of the islands caused by QD-induced interacting strain fields which give rise to a preferred direction in the In migration.[14,49] The QD dimensions increase in upper layers in a correlated growth regime: the average base diameter varies from ~15 nm in the first layer to ~35 nm in the top layer. This increase in size for closely spaced layer is characteristic of a sample that has not received the indium-flush treatment between the QD layers during growth.

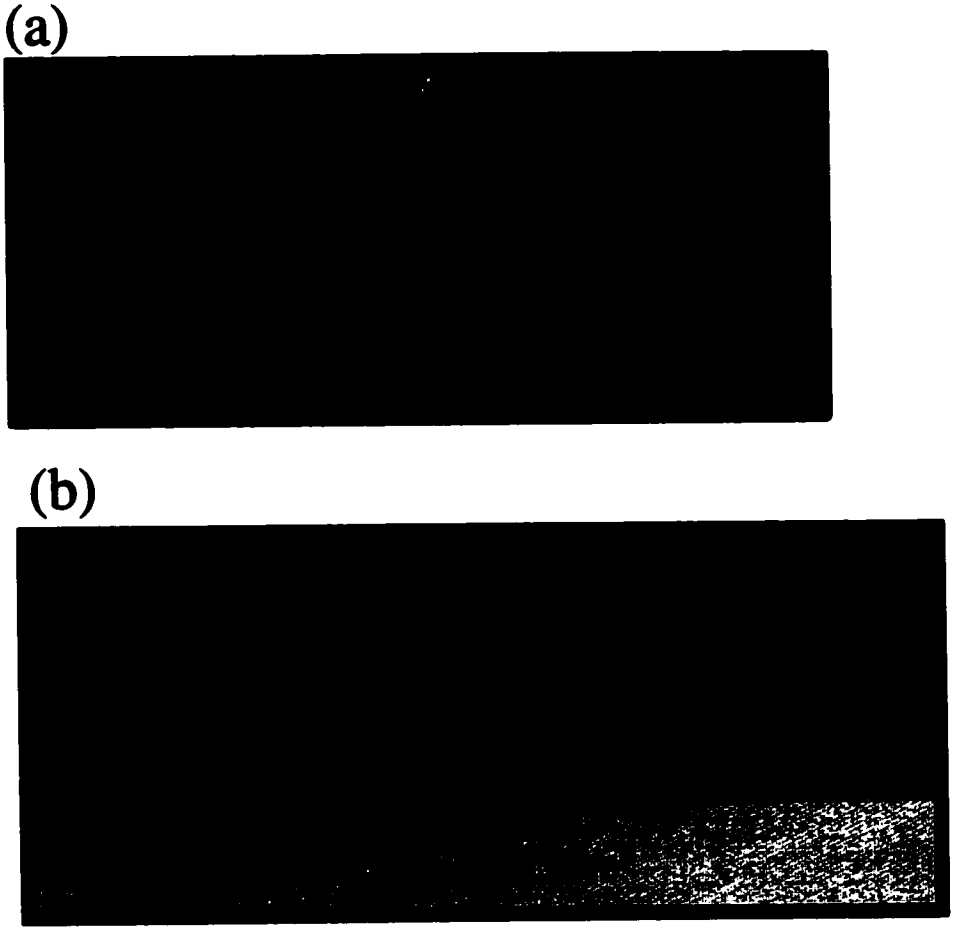

Figure 4.3 TEM cross-section view of the active region of (a) sample NT-5 and (b) sample NT-1. The $Al_{0.36}In_{0.64}As$ QDs (dark) are centered in the $Al_{0.25}Ga_{0.75}As$ (medium), and the $Al_{0.25}Ga_{0.75}As$/ $Al_{0.3}Ga_{0.7}As$ interfaces (line above and below) are clearly observed. TEMs by E. M. Griswold, Nortel Networks.

The TEM micrographs also show that the growth front returns to a planar mode after only a few nanometers of deposited $Al_{0.25}Ga_{0.75}As$ above the QDs to produce an atomically flat interface at the upper $Al_{0.25}Ga_{0.75}As/Al_{0.33}Ga_{0.67}As$ heterojunction. Table 4.2 displays the estimated QD densities obtained from the cross-sectional TEMs.

For a laser to function, one needs an active medium for light amplification, QDs in the case of the samples studied in this thesis, and a resonant cavity, i.e. two mirrors

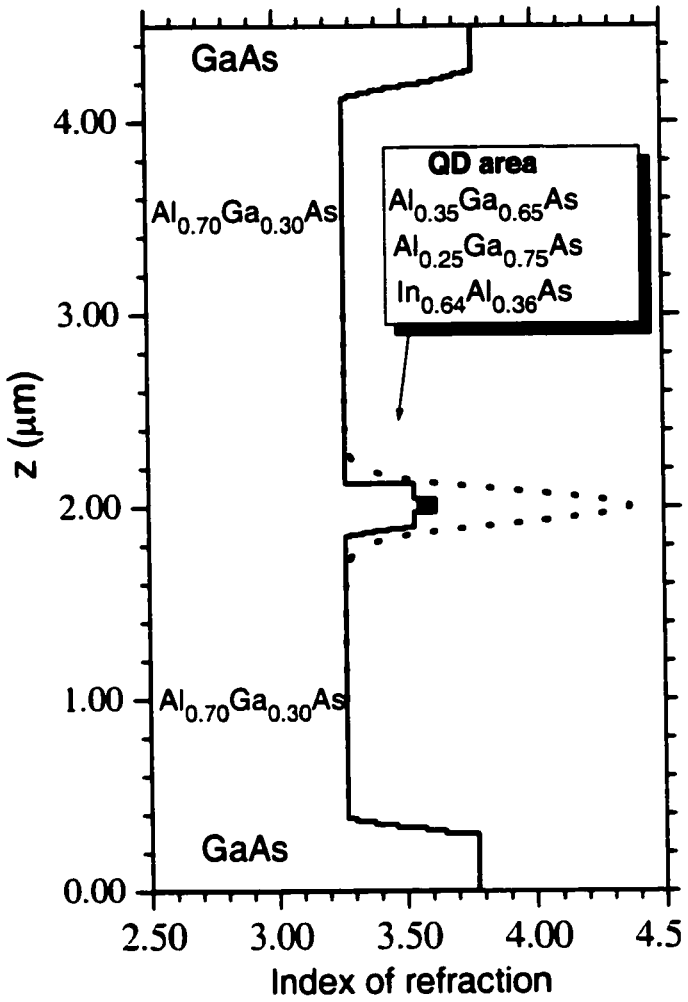

Figure 4.4 Index of refraction as a function of the laser structure cross-section (solid), and electric-field intensity of the first guided mode in the QD laser cavity for sample NT-1 (dotted).

delimiting a cavity capable of optical mode confinement such as a waveguide. The slab waveguide consists of a slab of high refractive index material sandwiched by low index material. The light is confined in the growth direction by the difference in refractive indices but diverges in the lateral direction of the cavity because there is no guiding structure in this direction. Waveguiding in this direction arises from the difference in gain between the regions underneath and outside the electrodes in Fabry-Perot lasers.

Numerical calculations of the guided modes of these structures were done using the multilayer slab waveguide model from a program by André Delage at NRC.[132] Figure 4.4 shows the change in index of refraction as a function of the laser structure cross-

section and the resultant electric field intensity of the first guided mode is displayed as the dotted line. The results show that the dominant guiding modes of the structure are the first transverse electric and transverse magnetic guided modes. The narrowness of the field intensity confirms that the outer heterojunctions confine the photons well owing to the large change in index of refraction between the $Al_{0.25}Ga_{0.75}As$ and the $Al_{0.7}Ga_{0.3}As$ regions. The lasing threshold current is influenced by the mode confinement factor Γ_{QD}, which represents the ratio of the optical power in the QDs to the total optical power

$$\Gamma_{QD} = \frac{\int_{QDs} |E_t(z)|^2 \, dz}{\int_0^{\infty} |E_t(z)|^2 \, dz}. \qquad (4\text{-}1)$$

For the structure shown in figure 4.3 with one layer of QDs, like sample NT-5, the optical confinement factor Γ_{QD} is calculated to be ~ 0.5 %. This value is obtained when approximating the QDs as a 1 nm thick well. This overlap between the optical mode and the QDs increases to Γ_{QD} ~ 2.5 % for sample NT-1, the laser structure with the stack of five QD layers. These confinement factor values are lower than values from QW laser structures since self-assembled QDs are thin and they cover at most 50 % of the area occupied by a two-dimensional structure.[93] Similar confinement factors are obtained for the InAs/GaAs QD lasers, their values will increase with increase in the number of layers for the same active region thickness, as well as increase in the QD density.

4.1.3 Laser processing

The laser structures were processed into broad area lasers with two cleaved

uncoated facets to form a laser cavity. The broad area lasers consists of a wide stripe acting as the Fabry-Perot cavity, homogeneously pumped, and do not require current confinement in the lateral direction, making the fabrication process relatively simple and easy.[133] Lasers were fabricated using standard photolithography and wet chemical etching. An ~2 cm^2 wafer piece was cleaned using organic cleaners, hydrochloric acid, and ammonium hydroxide. The *p*-doped side of the structure was coated in photoresist with a stripe pattern mask over it, which was then exposed to ultraviolet light, and subsequently developed, leaving only the stripe design. After this, 25 nm of titanium, 55 nm of platinum, and 300 nm of gold were evaporated onto the sample, and this was followed by a metal lift-off. The metal stripes were used as the positive electrical contacts during the experiments; these had widths of 40, 60, 100, 150, and 200 μm. At this point, the metal stripes are used to protect the semiconductor material beneath them, and the unprotected top 0.6 μm of GaAs, and the AlGaAs *p* layers were etched away. This etch prohibits current spreading along the lateral direction of the laser. The GaAs substrate was then thinned from 600 μm or 450 μm to ~ 150 μm for easy cleaving, and 25 nm of nickel, 55 nm of germanium, and 80 nm of gold were evaporated at the base of the sample and alloyed at 415°C for 15 s in a rapid thermal annealer; this is the negative electrical contact. The processed samples were cleaved into 100 μm to 5000 μm long strips, with each strip holding 1-10 broad area lasers. The strips were then bound on aluminium nitride laser diode mounts with a thermally activated, electrically conducting epoxy which provided the negative contact, while gold bonding of the top metallization strip provided the positive contact.

A few samples where processed into ridge waveguide structures to decrease the threshold current at room temperature. An ~2 cm^2 wafer piece was cleaned using organic cleaners, hydrochloric acid, and ammonium hydroxide. The *p*-doped side of the structure was coated in photoresist with a stripe pattern mask over it, which was then exposed to ultraviolet light and developed, leaving only the stripe design. This is followed by evaporation of metals onto the sample and metal lift-off. Ridges are etched using reactive ion etching (RIE). 200.0 nm of the dielectric SiO_2 is deposited followed by its patterning using resist and than etched off by RIE and removal of the resists and cleaning of sample. Since the ridges are only a few microns wide, metal contact pads must be deposited next to the ridges to allow space for bonding of gold wires. This is done again using a pattern on photoresist and depositing metals. The backside is then thinned and metallized followed by a 30 s 350°C rapid thermal anneal to allow metal alloying to take place and therefore ensure a good ohmic contact.

4.1.4 Tunability

Samples NT-1 and NT-5 were grown with elevated confining barriers to obtain room-temperature operation at lower thresholds. The large confining potentials result in impeded thermionic emission, as well as a larger optical confinement factor. The single layer sample (NT-5) has a threshold current of ~650 A/cm^2 at low temperatures, this increases to 4±1 kA/cm^2 at room temperature. The temperature characteristic of the threshold current density is usually formulated with the empirical relationship:

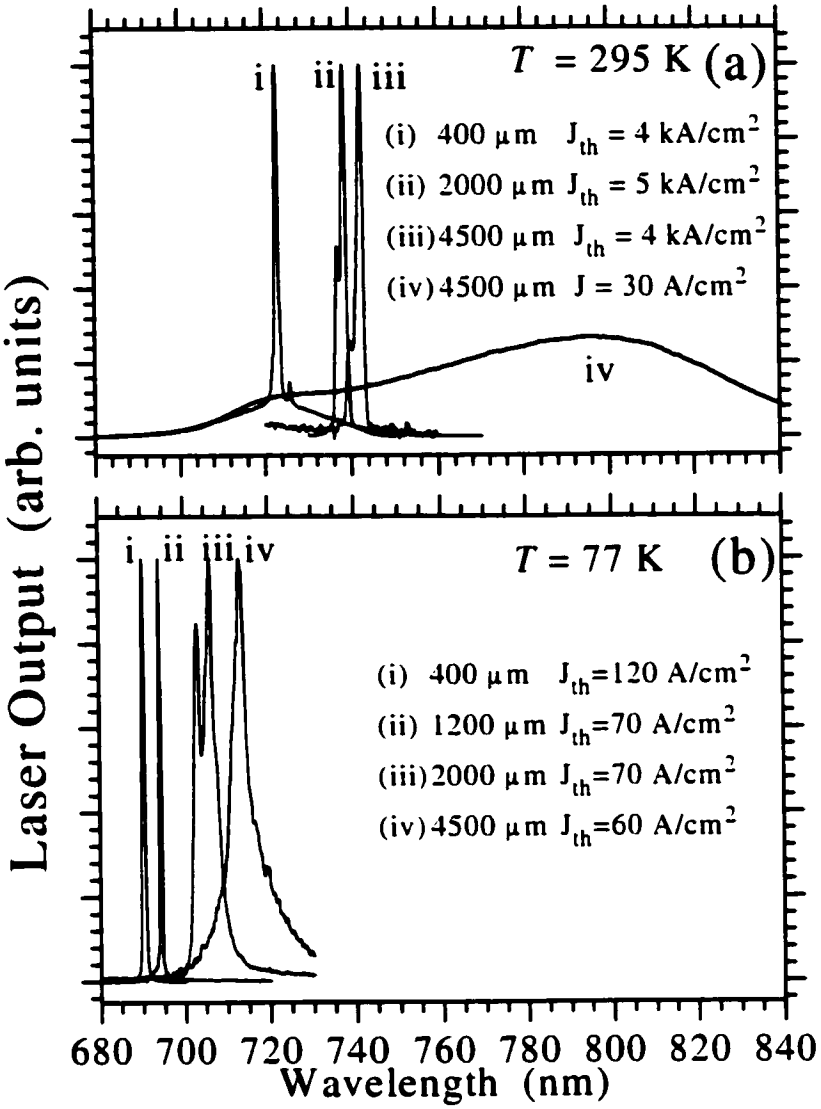

Figure 4.5 Laser output of sample NT-5 as a function of cavity length at (a) room temperature, and (b) T = 77 K. Cavity lengths and threshold current densities are indicated for each curve. Curve iv shows very low injection current spectrum for the longest laser cavity.

$$J_{th}(T_2) = J_{th}(T_1)\exp\left(\frac{T_2 - T_1}{T_0}\right) \tag{4-2}$$

where J_{th} is the threshold current density at two different temperatures T where $T_1 > T_2$, and T_0 is a characteristic temperature which characterizes the temperature dependence of threshold current. The larger the T_0 value, the weaker the temperature dependence of the

threshold current. For sample NT-5, the threshold current density results give a characteristic temperature T_0 = 50 K around room temperature. As a reference, typical

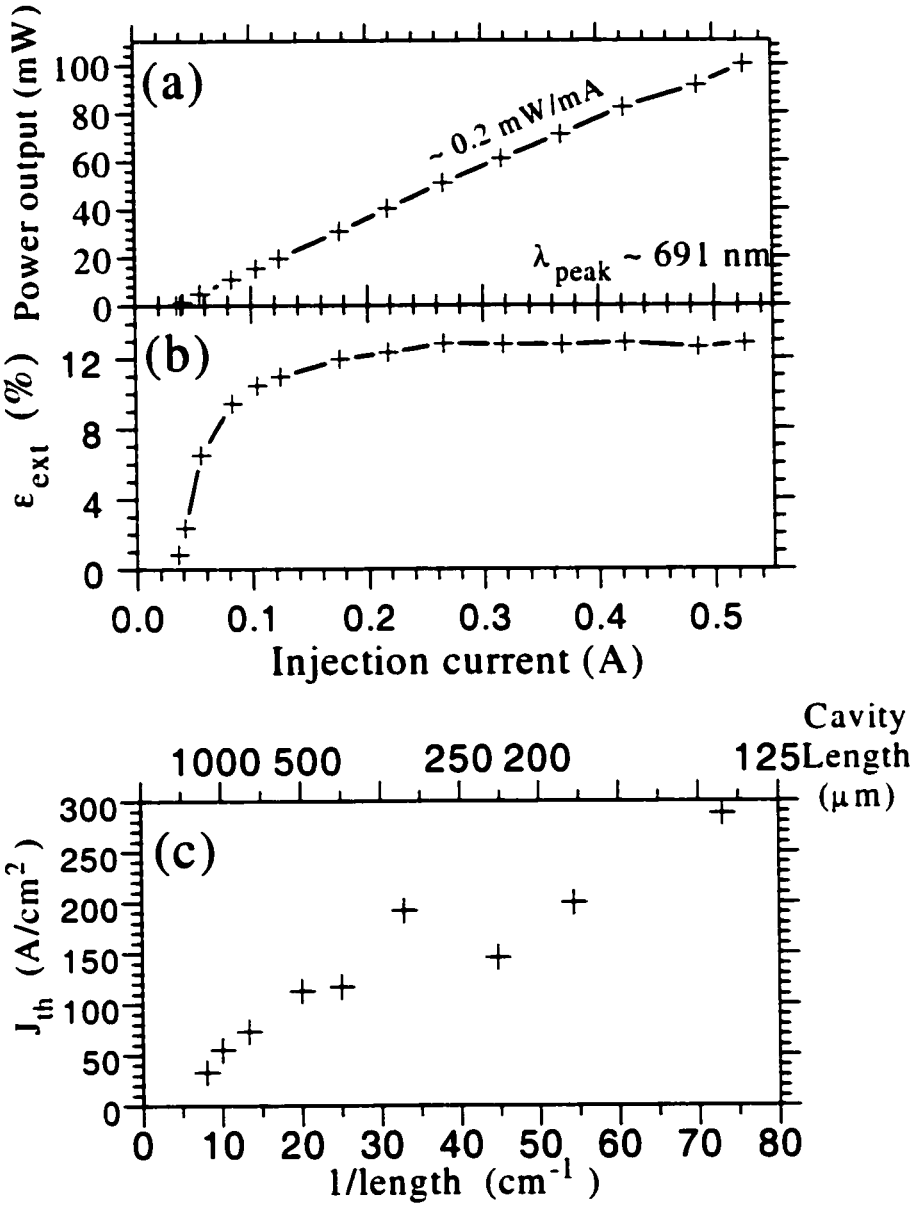

Figure 4.6 Lasing properties of sample NT-5 at T = 77 K for 60 μm metallization widths. (a) Peak power emission and (b) electrical-to-optical conversion efficiency ε_{eff} from both facets as a function of injection current. (c) Threshold current density versus reciprocal cavity length.

values of characteristic temperatures are T_0 = 120-160 K for a GaAs/AlGaAs double heterostructure QW laser around room temperature.[134]

Figure 4.5 shows lasing spectra for sample NT-5 at room temperature and at T = 77 K for different cavity lengths. The EL of curve iv in figure 4.5a displays QD state filling, the curve is smooth and almost featureless, so that we cannot obtain any information on the AlInAs QD shell structure. No WL is observed in the spectra because of the sample's high-QD density.[105,135] Curves i-iii are spectra taken just above threshold, the shortest laser emits at 723 nm, while the longest is at 742 nm representing a shift of 45 nm. All of these peaks are emitting from QD excited states. As figure 4.5 shows, in longer cavity devices, the lasing threshold decreases due to a larger material gain, and permit stimulated emission in lower states (see section 4.2.3 below). The 45 meV shift is significant although probably less than the intersublevel spacing for these QDs. The same shift is also observed at T = 77 K (figure 4.5b) and a significant decrease in threshold current density is noted as the cavity length is increased.

The efficiency of the 400-μm-long broad-area laser is investigated in the temperature range where the threshold has weak temperature dependence (T = 77 K). Figure 4.6a shows the output power from the two cleaved facets for quasi-CW injection current. The threshold current density is 160 A/cm^2, and CW operation is obtained from ridge waveguide lasers with similar current densities. The differential efficiency above threshold is 0.2 mW/mA, and the power output reaches 100 mW at 0.55 A. The net external quantum efficiency is calculated at ~12% (figure 4.6b). The capture and relaxation of the injected carriers is efficient since the QD coverage is at most 50% and,

due to the state distribution width of ~90 meV at low temperatures, only a small fraction (estimated to be at most 5% by looking at the threshold lasing line width compared with the inhomogeneous broadening of the QD distribution) of the QDs can emit at the lasing energy.

4.1.5 Gain

The optical gain of a QD laser should saturate at a certain value, since the number of carriers contributing to the stimulated emission is limited by the QD surface density. No saturation effect is observed in figure 4.6c where the threshold current density is plotted versus cavity lengths longer than 140 μm, indicating that saturation would occur for even shorter cavity lengths. The optical gain g_{QD} can be estimated at lasing threshold from

$$\Gamma_{QD}\, g_{QD} = \alpha_{mir} + \alpha_{in}, \tag{4-3}$$

where α_{mir} and α_{in} are mirror and internal losses, respectively. For short-cavity lasers where $\alpha_{in} << \alpha_{mir}$,

$$\alpha_{mir} = \frac{1}{L} \ln \frac{1}{R}, \tag{4-4}$$

where L is the cavity length and R is the reflectance at the facets.[136] Using values for the shortest cavity length measured (L = 140 μm) and an optical confinement Γ_{QD} calculated at 0.005, we obtain $g_{QD} \geq 1.7 \times 10^{4}$ cm^{-1}. This value is similar to ones reported for InAs/GaAs QD lasers.[137,138]. Comparisons are difficult to make with a similar single QW laser since it is not possible to grow a thick enough InAlAs QW in AlGaAs, due to the

large lattice mismatch between the two materials, to reproduce the emission wavelength. A value of peak material gain of ~3000 cm^{-1} for low temperature has been stated for an InGaAs/GaAs QW laser.[137] This gain value is an order of magnitude less than the one measured here

4.1.6 Broadband lasing

Waveguide simulations show a significant increase in the optical confinement factor for lasers with more than one QD layer in the active region. Sample NT-1 has the same separate confinement structure as NT-5 but the active region is wider with five layers of QDs sandwiched between 8 nm $Al_{0.25}Ga_{0.75}As$ spacer layers. The EL shown in figure 4.7 displays a Gaussian peak at λ = 920 nm (1.087eV) having a FWHM of 150 meV at very low current at room temperature, this is ~ 3 times wider than what is measured for the single layer structures. This is not surprising since the TEM micrograph shows an increase in QD dimensions on each additional layer grown, so that the larger QDs located on the top layers will emit at lower energies than the smaller ones located on lower layers due to reduced carrier confinement. What is assigned as the ground state emission for this sample is located ~100 nm lower energy than the ground state of sample NT-5. As the current is increased, state filling is observed and lasing occurs in the QD excited states. At threshold, the lasing linewidth is 5-7 meV wide, and at higher currents, the stimulated linewidth broadens significantly up to a 60 meV wide at a current density of 3.0 kA/cm^2 (figure 4.7b). This value is much larger than any observed with either single layer QD lasers for high current densities (for sample NT-5 at J = 2.0 kA/cm^2, the

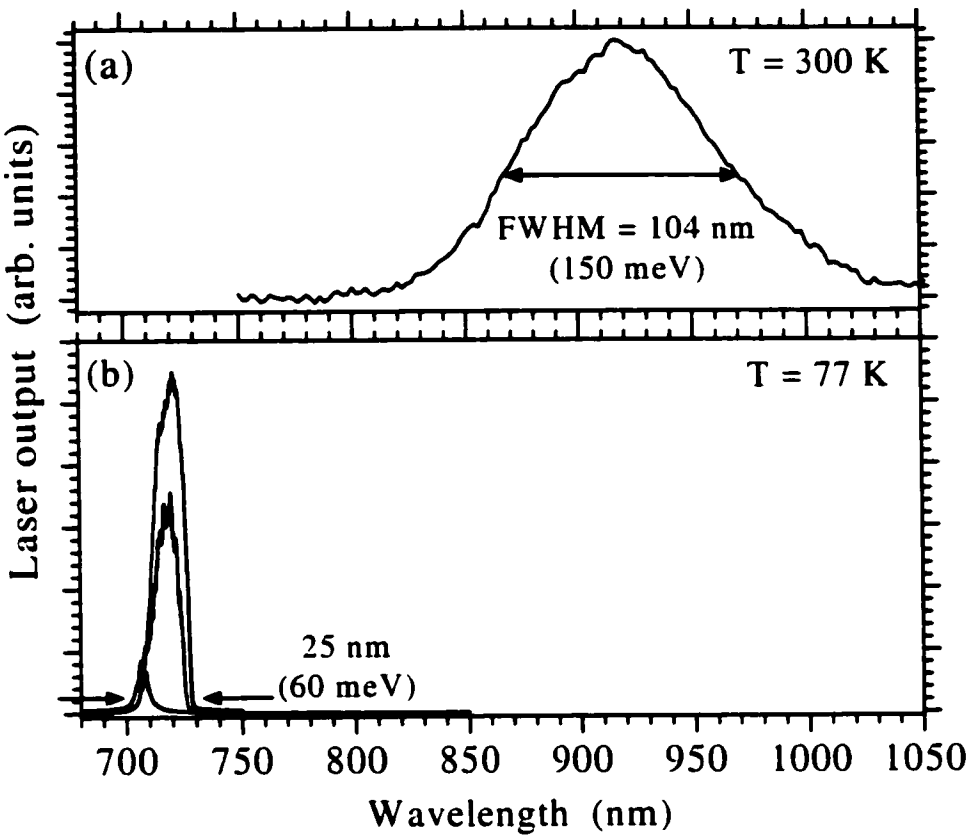

Figure 4.7 (a) Spontaneous emission spectrum of a ~0.5-mm-wide by ~1-mm-long piece of sample NT-1, the five layer sample, at room-temperature with 1.0 mA injection current. (b) Stimulated emission at T = 77 K of sample NT-1 in a 60 μm by 400 μm cavity for different injection currents. The bottom curve is for an injection current of 115 mA, the middle curve is taken at 450 mA and the top curve is for a current of 720 mA.

linewidth was ~ 8 meV), or for a reference 5.0-nm thick GaAs QW laser with the same cladding layers as sample NT-1 emitting at 830 nm (at J = 1.7 kA/cm^2, the linewidth was ~ 4 meV). The larger inhomogeneous broadening of the QD ensemble allows for a larger gain bandwidth in the stimulated emission process.

A drawback for a broadened gain such as sample NT-1 is that a smaller proportion of the QD ensemble contributes to lasing at threshold. Therefore one must excite the QD laser at a significantly higher current density to obtain lasing threshold compared with a sample having QDs with the same dimensions on each layer.

For temperatures below 77 K, the threshold lasing linewidth is 10-12 meV wide

about double the value measured at higher temperatures. This transition between strong multimode emission at threshold to narrower emission widths with increasing temperature is believed to be due to thermal coupling between the QDs and WL.[139,140] At higher operating temperatures, thermal emission of carriers out of the QDs having smaller confinement energies (i.e. the smaller QDs) in the ensemble and subsequent recapture by neighbouring QDs with deeper confining potentials becomes important.[141] At higher lasing currents, stimulated emission from the WLs is observed indicating that some of the injected carriers do not have time to diffuse from the two-dimensional WL to the zero-dimensional QDs before recombining.

4.1.7 Emission from single quantum dots

In order to understand the shell structure of the ternary QDs, PL mapping of ridge waveguide laser facets was done using a sub-micron diameter probe spot. By mapping the facet using 0.1 μm steps, imaging the cross-section of the structure is possible.

The small laser probe diameter is achieved using a 60 X microscope lens and using equations for a Gaussian beam,[142] the beam waist diameter d can be expressed in terms of the input beam parameters:

$$d = \left(\frac{4\lambda}{\pi}\right)\left(\frac{F}{D}\right), \tag{4-5}$$

where λ is the laser wavelength, F is the lens's focal length, and D is the beam diameter. In this case, we used a 60 X focal length microscope lens to focus the collimated output of the 488 nm line of an Ar^+ ion laser that has an ~3-4 mm diameter beam. The diameter

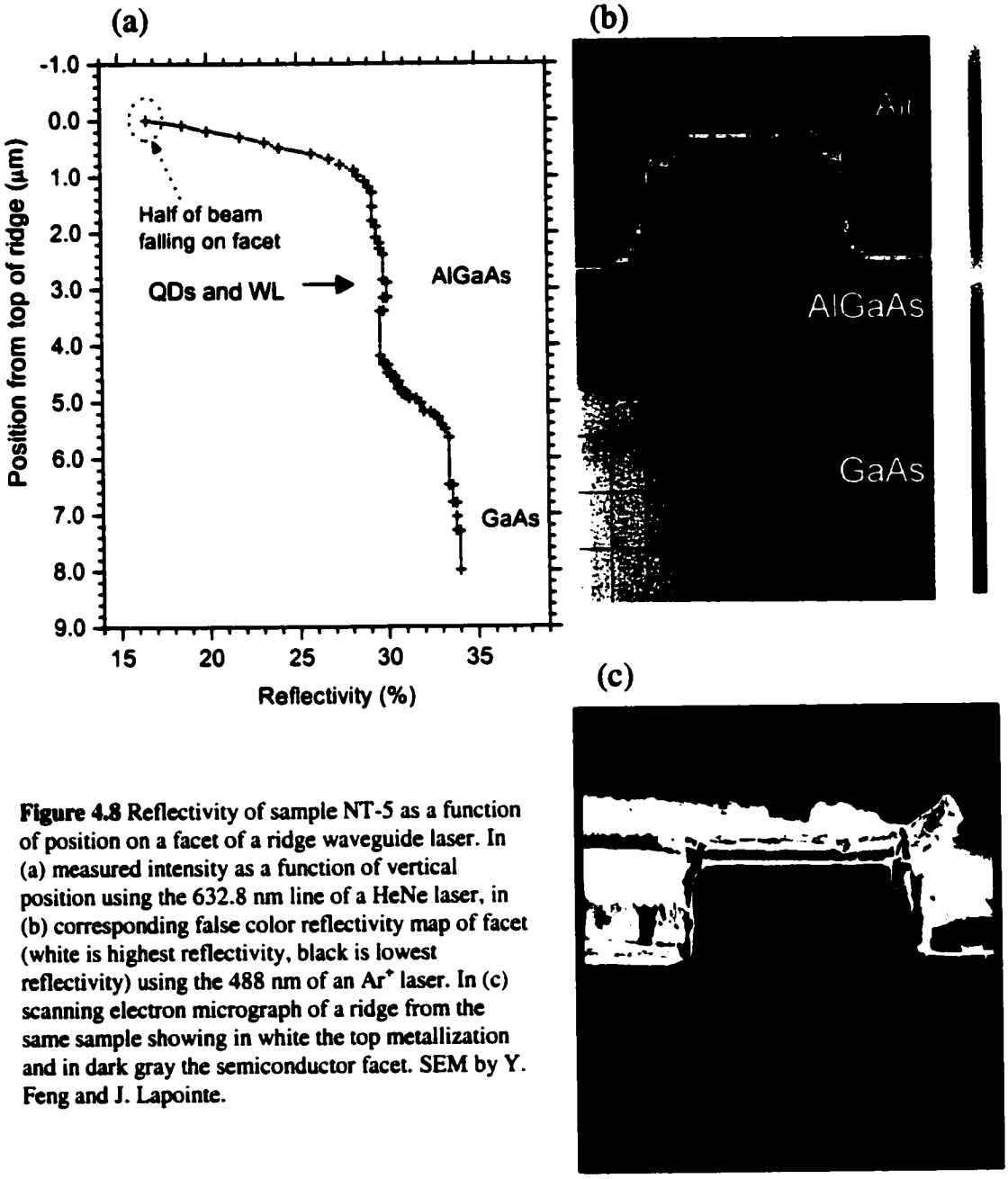

Figure 4.8 Reflectivity of sample NT-5 as a function of position on a facet of a ridge waveguide laser. In (a) measured intensity as a function of vertical position using the 632.8 nm line of a HeNe laser, in (b) corresponding false color reflectivity map of facet (white is highest reflectivity, black is lowest reflectivity) using the 488 nm of an Ar^+ laser. In (c) scanning electron micrograph of a ridge from the same sample showing in white the top metallization and in dark gray the semiconductor facet. SEM by Y. Feng and J. Lapointe.

of the focal spot is therefore ~0.6-0.8 μm.

Figure 4.8a displays the reflectivity of a facet from a 5 μm wide ridge waveguide laser structure as a function of vertical position where 0.0 μm is set as the top of the

structure. Between the 0.0 μm and 1.0 μm position, part of the laser beam does not reflect since it continues its path in air, the reflectivity increases from 15 to 29 %. From the 1.0 μm position to the 4.0 μm position reflectivity is measured at 29 %, this is followed by a gradual increase over a 1 μm distance up to 34 %, this value stays constant up to the 8 μm position. At normal incidence, the fraction of the incident intensity which is reflected R off an air-semiconductor interface can be written as

$$R = \left(\frac{n-1}{n+1} \right)^2, \tag{4-6}$$

where n is the index of refraction of the semiconductor. For $Al_{0.7}Ga_{0.3}As$, n = 3.35 at 632.5 nm giving a reflectance value of 29 %,[143] for GaAs, n ~ 3.5 giving a reflectance value of 34 %.[62] The measured values correspond well to the ones reported in the

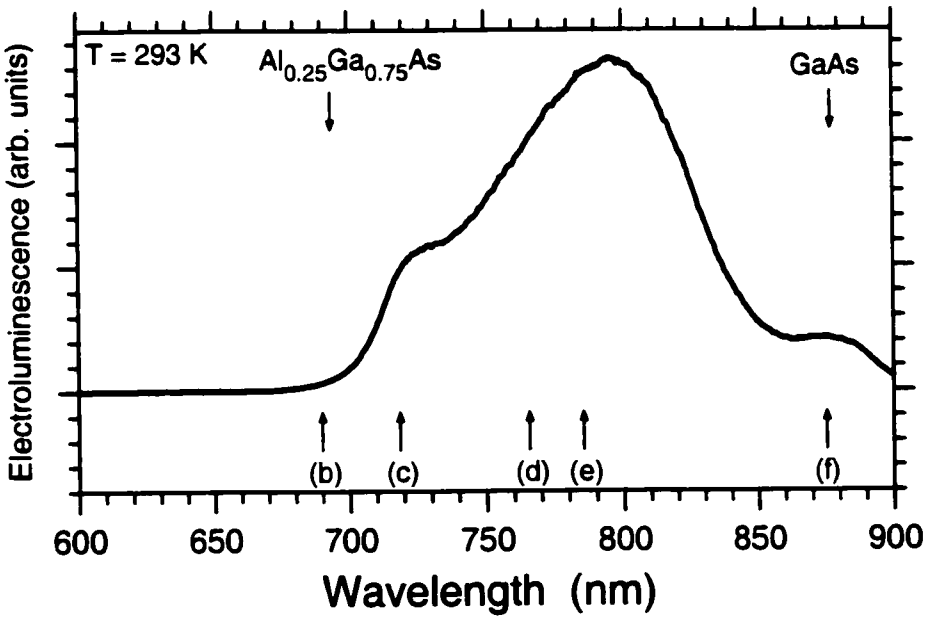

Figure 4.9 EL spectra at very low injection current (2 μW/cm^2) of sample NT-5 at 20 °C. The arrows labeled (b) to (f) correspond to the detection wavelength of the PL maps shown in figure 4.10.

literature.

Figure 4.8b displays the reflectivity map of a 5 μm wide facet using a false color scale shown on the right. The first top 4 μm of the structure is AlGaAs shown in red, below this is GaAs shown in purple. The etched ridge structure itself is clearly observed with air shown in black. The QDs are not resolved since they represent a fraction of a percent of the thickness of the AlGaAs layers and their index of refraction is similar (n ~ 3.5). Figure 4.8c is a scanning electron micrograph of the edge of a laser from the same sample. The ridge dimensions on the reflectivity map correspond with the ones from the SEM.

Figure 4.9 shows the very low injection current EL curve of sample NT-5 which displays state filling of the QDs between 710 and 850 nm. No resolved QD shell structure is visible in the spectra when exciting this large amount of QDs, as well, no WL emission is observed due to the sample's high QD density. GaAs emission is observed at 875 nm. EL studies at low temperatures show the QD distribution to have a FWHM of ~90 meV.

Detection of the PL originating from the two 15 nm wide planes of $Al_{0.25}Ga_{0.75}As$ above and below the QDs is shown in figure 4.10b for excitation intensity of ~1 kW/cm^2. We see that it is placed right under the ridge in the middle of the AlGaAs region revealed in the reflectivity map. The width of the $Al_{0.25}Ga_{0.75}As$ area using the PL mapping system is ~1 μm in agreement with the spatial resolution of the setup when exciting at 488 nm. In figures 4.10c, 4.10d and 4.10e, PL detection was at different energies of the QD energy distribution (refer to figure 4.9) on a broad area laser facet. It should be noted that the relative intensities are reset for each map. An estimate of the number of QDs probed can be done using the absorption coefficient of the barrier material α:

$$I_t = I_i e^{-\alpha d}, \tag{4-7}$$

where the intensity at a certain depth in the material I_t is related to the incident intensity I_i, and d is the material thickness. For GaAs, $\alpha = 1 \times 10^5$ cm^{-1} in the visible, this results in a characteristic excitation depth of ~0.2 μm.[144] Using 1 μm as the incident beam diameter, we can estimated that ~20 QDs are excited optically. Due to non-radiative surface recombination rates, the PL of the QDs closest to the surface will be considerably quenched and their emission is probably not detected.[145] The surface effects certainly take place in the 10 nm closest to the surface, but probably go on deeper as well due to oxidization of the aluminium alloy at the facet.

The diffusion length of the generated carriers and excitons in PL also plays a significant role in determining the resolution of the micro-PL technique. The diffusion length (L_{diff}) is a parameter that is complicated to model, and most data rely on empirical measurements. In principle,

$$L_{diff} = \left(\frac{k_B \mu T \tau}{q_e} \right)^{1/2} = (D\tau)^{1/2}, \tag{4-8}$$

macroscopically,[146] where k_B is Boltzmann's constant, μ is the mobility of the diffusing carriers, T is the sample temperature, q_e is the electron charge, D is the diffusion constant, and finally, τ is the lifetime of the diffusing carrier. The diffusion length can be limited by local potential variation, nonradiative surface recombination for excitation close to the surface, as well a doping.[47] An ambipolar diffusion length, i.e. the combined diffusion lengths of electrons and holes, of 0.68 μm were measured for a 10 nm thick GaAs QW in $Al_{0.3}Ga_{0.7}As$ barriers at 300 K.[147]

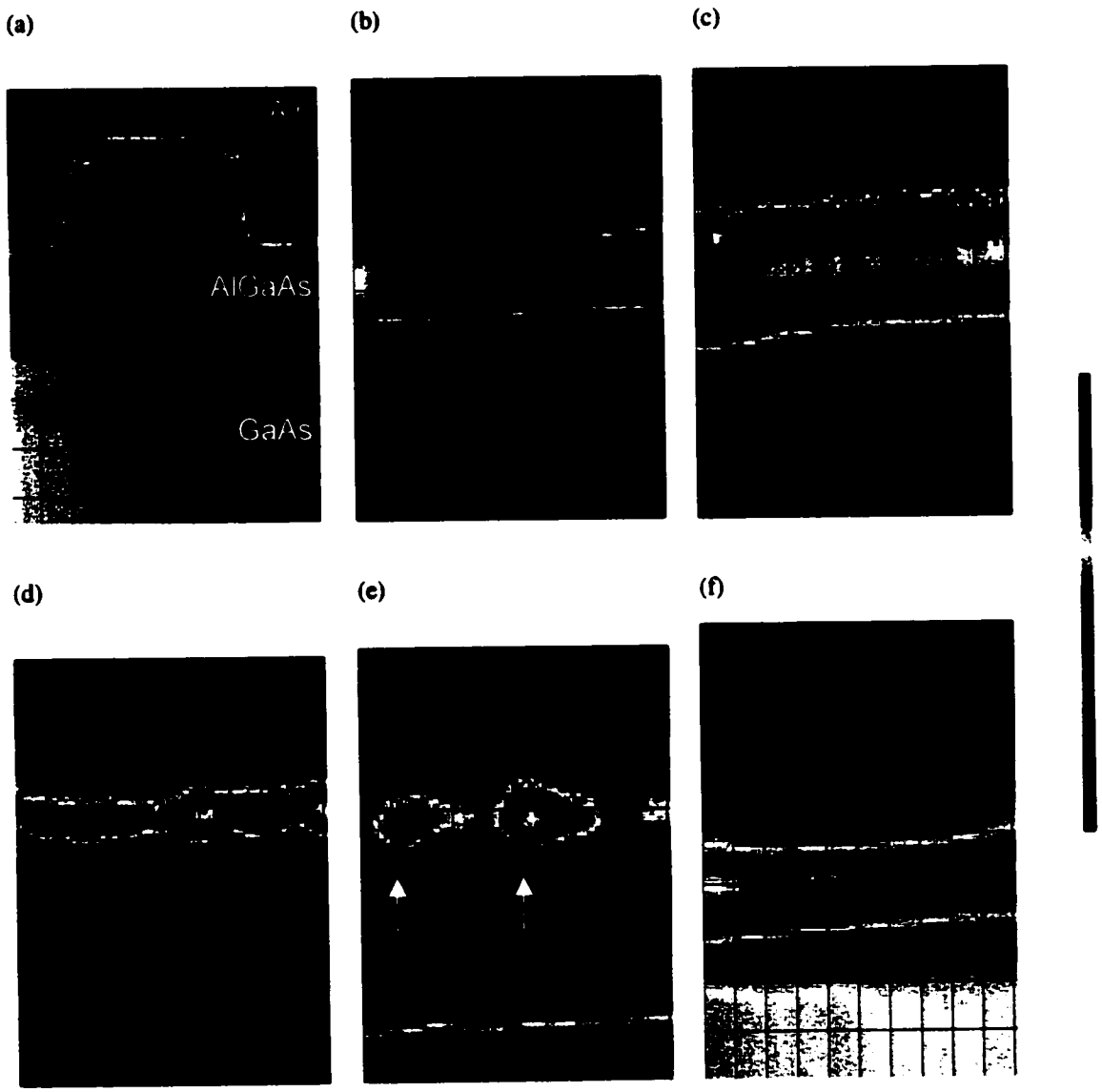

Figure 4.10 Mapping of a facet from an NT-5 ridge waveguide laser using a false color intensity scale where white is the highest intensity on a specific map and black is the lowest intensity (legend is shown on right) at room temperature. (a) reflectivity measurement showing air at the top in black, towards the middle in red is AlGaAs, and the bottom four microns is GaAs in pink. PL map with detection set in (b) for $Al_{0.25}Ga_{0.75}As$ at 693 nm, in (c) for the higher energy part of the QD distribution at 720 nm, in (d) for the middle of the QD distribution at 765 nm, in (e) for the low energy part of the QD distribution at 785 nm, and in (f) for GaAs at 875 nm.

In figure 4.10e, the detection is set at 785 nm, around the maximum intensity of the QD distribution. The detection spectral window of the PL maps is 3 nm, thus only

~10% of the QD ensemble (zero to a few QDs) can be detected. Strong emission is observed from two very distinct areas in the laser active region marked by arrows. The strongest intensity is recorded at the center of the right spot surrounded by high intensity red over a 1 μm diameter. The area indicated by the left arrow is slightly less intense, and on the extreme right side of the map, a weaker (yellow) area is observed. As well, emission from the n-doped substrate GaAs is observed in magenta on the bottom 2μm of the PL map. In figure 4.10d, the detection wavelength was set at 765 nm, in the middle of the QD distribution. All of the QD area is emitting with variations in the intensity depending on the position. In figure 4.10c, the detection wavelength is set at 720 nm, at the higher energy part of the QD distribution, very close in energy to the WL energy. Most of the QD area is emitting with the same intensity, although this is not as smooth as the emission in figure 4.10b where, the detection is set for the thick $Al_{0.25}Ga_{0.75}As$ QW surrounding the QDs. Approximately 1.5 μm below the active region, a red continuous line is observed. This emission originates from thin GaAs QWs in the *n*-$Al_{0.7}Ga_{0.3}As$, these thin films between 0.8 nm to 10 nm thick act as smoothing layers in thick AlGaAs to minimize interface roughness.[1] In figure 4.10f, detection is set at 875 nm to observe the emission of GaAs from the ridge laser. Since the GaAs is *p*-doped above the active region and *n*-doped below the active region, both areas emit with different intensities.

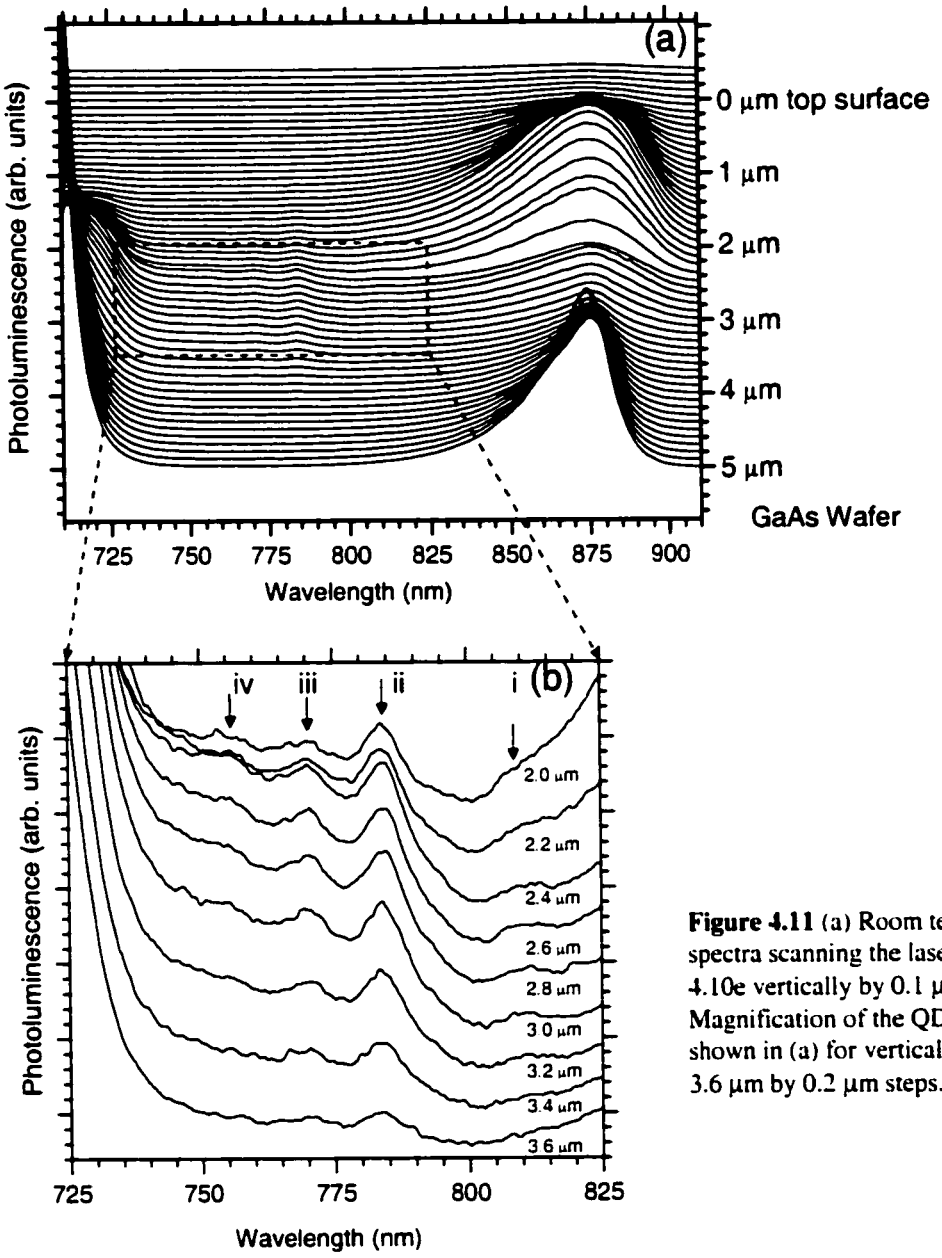

Figure 4.11 (a) Room temperature PL spectra scanning the laser facet of figure 4.10e vertically by 0.1 μm steps. (b) Magnification of the QD emission spectra shown in (a) for vertical positions 2.0 to 3.6 μm by 0.2 μm steps.

To further understand figures 4.10c, 4.10d and 4.10f, micro-PL spectra with 0.1 μm steps were taken along the vertical axis centered on the right QD in figure 4.10e, this is shown in figure 4.11a. At the top of the sample, we observe the p^+ GaAs cap peak centered at 875 nm for the first micron. The p^+ GaAs stops around micron 2. At this point, we observe a strong peak at 700 nm: $Al_{0.25}Ga_{0.75}As$, and approximately four fainter

peaks appear between 730 and 830 nm. After the 3 micron mark, emission from *n* doped GaAs is seen at 875 nm, as well emission from a protective GaAs superlattice in the *n* $Al_{0.7}Ga_{0.3}As$ is observed around 700 nm at the 5 micron mark (not shown). Therefore, the green around the QDs in figure 4.10e is associated with weak emission from the low-energy shoulder of $Al_{0.25}Ga_{0.75}As$. As we probe the lower part of the facet, the color changes to green, followed by dark blue, and finally light blue, a sign of higher intensity, and then a high intensity red-magenta at the bottom of the figure indicating strong emission from the high-energy shoulder of the *n*-doped GaAs wafer.

The QD emission region is shown magnified in figure 4.11b. The four peaks labelled i to iv are positioned at 811 nm (1.529 eV), 784 nm (1.581 eV), 770 nm (1.610 eV), and 755 nm (1.642 eV) respectively. They are all located within the ensemble QD emission shown in figure 4.9. Peak ii has the strongest intensity and corresponds to the QD emission of figure 4.10e, the spectral resolution of the experiment does not allow the observation of resolved sharp lines originating from specific energy level transitions,[28] but we can still observe energy spacings of ~30 meV between peaks ii and iii, and between peaks iii and iv, up to an energy spacing of 53 meV between peaks i and ii. These energy intervals are within the range observed for intersublevel energy spacing in the InAs/GaAs self-assembled QD system,[36] although they are smaller than the 70 meV intersublevel energy spacing observed in the study of InAlAs/AlGaAs QDs presented in the next chapter. In that study, the InAlAs/AlGaAs QD growth conditions as well as the heterostructure were different from this case. As well, it has been observed that due to the parabolic confinement potential, the intersublevel energy spacings are nearly equidistant in GaAs-based QD systems,[36] and peaks ii, iii, and iv are spaced 30 meV one from

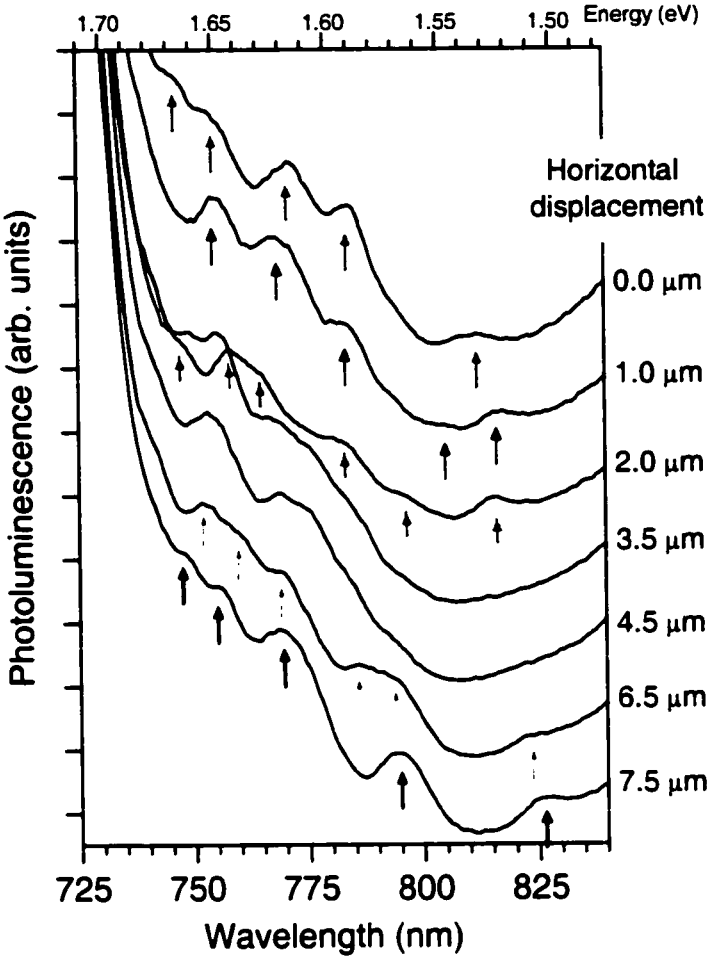

Figure 4.12 Room temperature PL spectra as a function of horizontal displacement in the active region of the laser.

another and therefore could be emission from the same QD. Peak i has very weak intensity and could be emission from another QD that is excited less.

Figure 4.12 shows micro-PL of the QD emission as a function of horizontal position along the WL. The curve at 0.0 μm has five peaks marked by arrows with energy spacings ranging from 20 to 53 meV between them. We observe the same type of pattern for the other curves, usually, five to six peaks can be observed per spectra with energy spacings varying between 15 and 59 meV. Exceptions are the 3.5 and 4.5 μm curves since they seem to have at least five or six peaks per spectrum but these are convoluted so as to show an increase in intensity but no resolvable features. Spectra that are taken 1 μm from one another show some similar characteristics, for example the 1 μm and 2 μm spectra

both have a peak at 816 nm and one at 784 nm so probably both spots are probing the same QD or QDs, but the other peaks appearing on these two curves do not seem to show this type of correspondence. We can rule out emission from the smoothing GaAs QW layers since the spectra changes as we move horizontally across the sample. There are probably more then five or six peaks per spectra indicating that we are detecting more than one QD per spectra, but the emission from the low energy side of the $Al_{0.25}Ga_{0.75}As$ peak as well as possible convolution of peaks prevent definite conclusions on the number of QDs probed.

4.2 InAs/GaAs quantum dot laser diodes

4.2.1 Sample growth

The Stranski-Krastanow growth mode was used to produce between seven and eleven layers of self-assembled QDs in the active region of a two-step separate confinement heterostructure (figure 4.13). The structures generally consisted of a thick (~2 μm) $Al_{0.7}Ga_{0.3}As$ contact layer doped n^+ ~ 6×10^{17} cm^{-3}, followed by a bottom cladding layer of n ~ 3×10^{16} cm^{-3} doped $Al_{0.33}Ga_{0.67}As$. The active region is composed of 17 nm undoped GaAs on each side of a stack of self-aligned InAs QDs. All the InAs layers were grown at 515 ± 5°C and these were followed by 60 s growth interrupts. The active region is followed by a symmetric p-doped step-graded cladding and contact layers with corresponding doping and material concentrations follow, and a 150 nm p^+-GaAs cap (p ~ 3×10^{19} cm^{-3}) terminates the structure. The samples were processed into broad

area lasers as described at the beginning of the chapter.

4.2.2 Structural characterization

Figure 4.2a displays the confining potentials for this structure.[68,125,126] The bandgap energies of the different materials contained in the heterostructures are given in table 4.1. It should be noted that the energies are for unstrained materials. The lattice mismatch between InAs and $Al_{0.25}Ga_{0.75}As$ is ~ 7.1 %;[130] this compressive strain produces an increase in the bandgap compared with unstrained materials.

Four different laser structures of this type were grown for this study, their

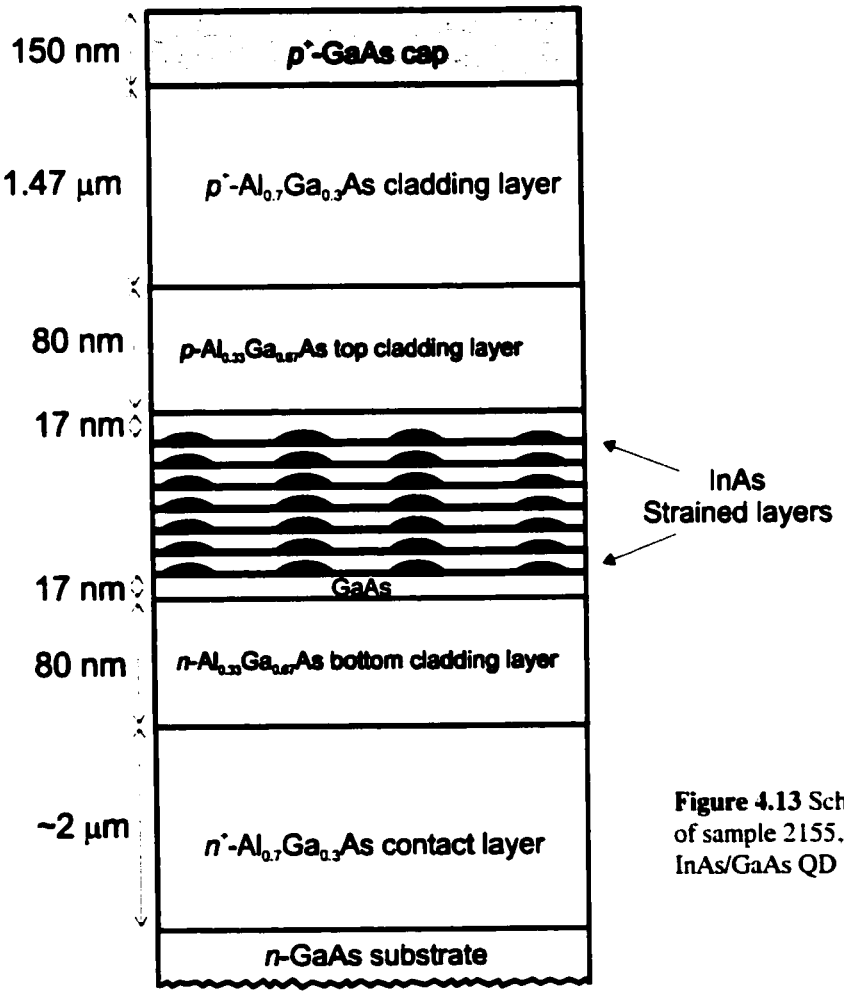

Figure 4.13 Schematic cross-sectional view of sample 2155, a seven layer stack InAs/GaAs QD laser.

characteristics are listed in table 4.3. For samples 2155 and 2157, the top cladding layers of the structure were grown at lower temperatures (~540°C) to avoid additional in situ QD intermixing. The laser structure of sample 2155 was engineered to have a ground state emission at λ ~980 nm. This is the most common wavelength used for pump lasers in erbium-doped fiber amplifier devices in wavelength division multiplexing systems. The active region has seven layers of QDs in order to increase the gain and the optical confinement factor of the QDs. The layers are separated by 10.4 nm of GaAs leading to uniform self-aligned QD stacks with little wavefunction coupling between QDs in adjacent layers.[48] Sample 2157 has eleven layers, in this case in order to keep the same thickness for the active region, the GaAs spacer layers are 6.4 nm apart, this probably leads to some wavefunction coupling between the QDs in adjacent layers (for a more thorough discussion on this subject see the chapter on coupled QDs). Sample 2084 is also a seven layer sample but with a higher QD density hence, no WL emission is observed in PL or EL measurements. Sample 2093 is a reference QW laser sample emitting at 880 nm at 77 K. The QD densities are estimated from TEMs taken from samples with similar growth conditions.

Sample	Description	GaAs spacer layer thickness	Amount of InAs deposited	Indium flush	QD density (QDs/μm^2)
2084	7 layers of QDs	10.4 nm	2.5 ML	5.0 nm	> 100
2155	7 layers of QDs	10.4 nm	1.9 ML	2.8 nm	~30-40
2157	11 layers of QDs	6.4 nm	1.9 ML	2.8 nm	~30-40
2093	7 WLs	10.0 nm	1.8 ML	5.0 nm	----------

Table 4.3 InAs/GaAs QD laser samples.

4.2.3 Tunability

Figure 4.14a displays state-filling spectroscopy of the energy levels of sample 2155, the seven layer QD laser sample. As the injection current is increased from 1 to 360 mA, an electronic shell structure with at least four levels is revealed having intersublevel energy spacings of ~40 meV. The lasing spectra for currents taken slightly above threshold are shown in figure 4.14b, for various cavity lengths. The shortest cavity with asymmetric facets (i.e. poor cavity) emits just below the WL energy in the highest QD shell at λ = 869 nm. As the cavity length is increased, the lasing peak shifts to 900 nm for a 500 μm cavity, to 927 nm for a 1000 μm cavity, to 955 nm for a 2000 μm cavity, and to

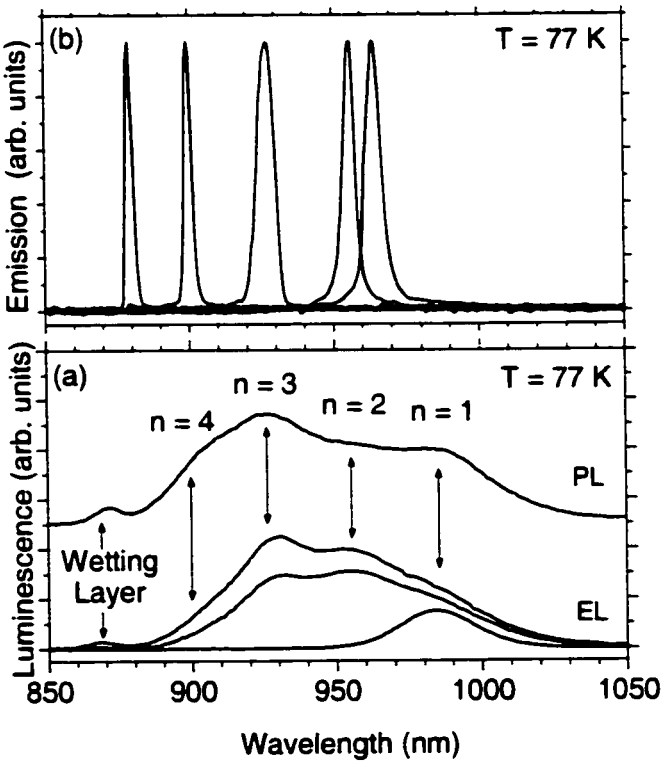

Figure 4.14 PL and EL spectra at T = 77 K from the sample consisting of a stack of seven InAs/GaAs QD layers. (b) Lasing spectra just above threshold for different cavity length. from right to left the lengths are: 500 (nonparallel facets), 500, 1000, 2000, and 5000 μm, respectively.

964 nm for a 5000 μm cavity. An increase in gain media results in lasing towards the QD ground states. This demonstrates that the diode cavity length can be used to adjust the lasing wavelength by 95 nm compared to a few nanometers for a QW structure when an external cavity pumping scheme is not used.[148] It has been shown that by coating the facets with high reflectivity coatings, ground state QD laser emission can be observed. High reflectivity coatings (e.g. SiO_2/SiN_x) reduce the optical losses at the facets and therefore lowers the threshold current density.[149]

The wavelength tunability is also observed at room temperature as shown in figure 4.15. Shorter cavity lengths lase in the n = 4 shell, while the longest cavity emits in the n = 3 shell. A change towards a higher shell is observed for the lasing position of a given cavity length from 77 K to 290 K (see table 4.4). This is brought about by the

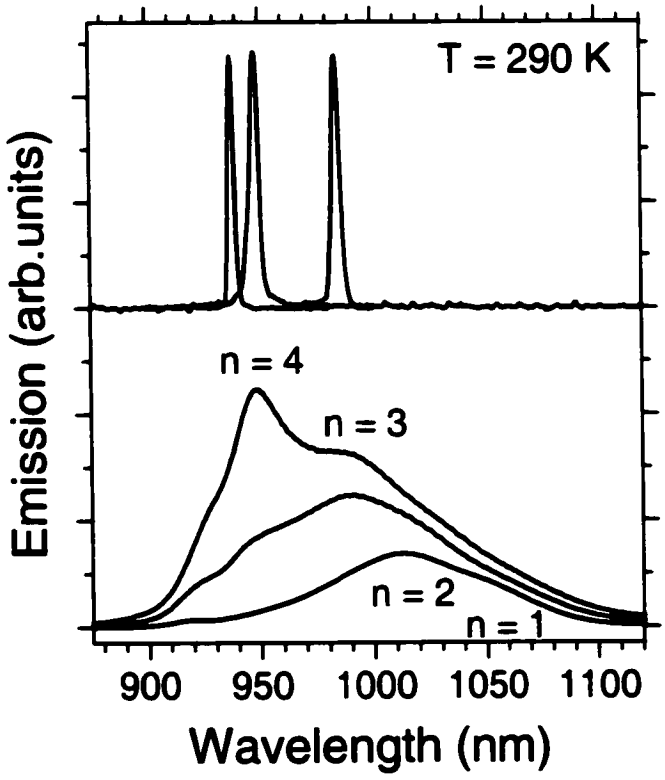

Figure 4.15 (a) EL (bottom) and lasing (top) from the seven layer sample (2155) at T = 300 K. The just above threshold lasing peaks, from left to right, are for 500, 1000, and 5000 μm long cavities, respectively.

increased thermionic emission of the carriers from the QD potentials to the WL at higher temperatures. The lasing peak from the 1000 μm cavity shifts from n = 3 to n = 4, while the lasing peak from the 5000 μm cavity shifts from n = 2 to n = 3.

Table 4.4 and figure 4.16 show the wavelength shift and threshold current density trends. The same trends are observed at T = 77 K and T = 290 K, as the cavity length is increased, a red shift of the lasing wavelength is observed as discussed previously. Also, a significant decrease of the threshold current density is observed which should be expected since longer cavity wavelengths emits in a lower shell, requiring less current to fill them.

Cavity length (μm)	J_{th} at T = 77 K (A/cm^2)	Lasing level at T = 77 K	J_{th} at T = 290 K (A/cm^2)	Lasing level at T = 290 K
5000	13.5	n = 2	430	n = 3
2000	15	n = 2		
1000	125	n = 3	490	n = 4
500	180	n = 4	667	n = 4
500*	325	n = 5		

Table 4.4 Threshold currents and lasing position for the seven layer sample (2155). (*) Last 500 μm cavity has non-parallel facets.

Some groups have observed mode structure at lasing threshold during low temperature operation[150,151] as well as a decrease in the number of these modes as a function of increasing temperature.[139,149] In contrast to this, our emission spectra do not show multimode structure at threshold, rather, single mode structure is apparent in all samples. In addition, no pronounced changes were observed in the width of the lasing spectra just above threshold as a function of temperature. This absence of multimode features indicates a good uniformity of the QD ensemble, and according to Asryan and

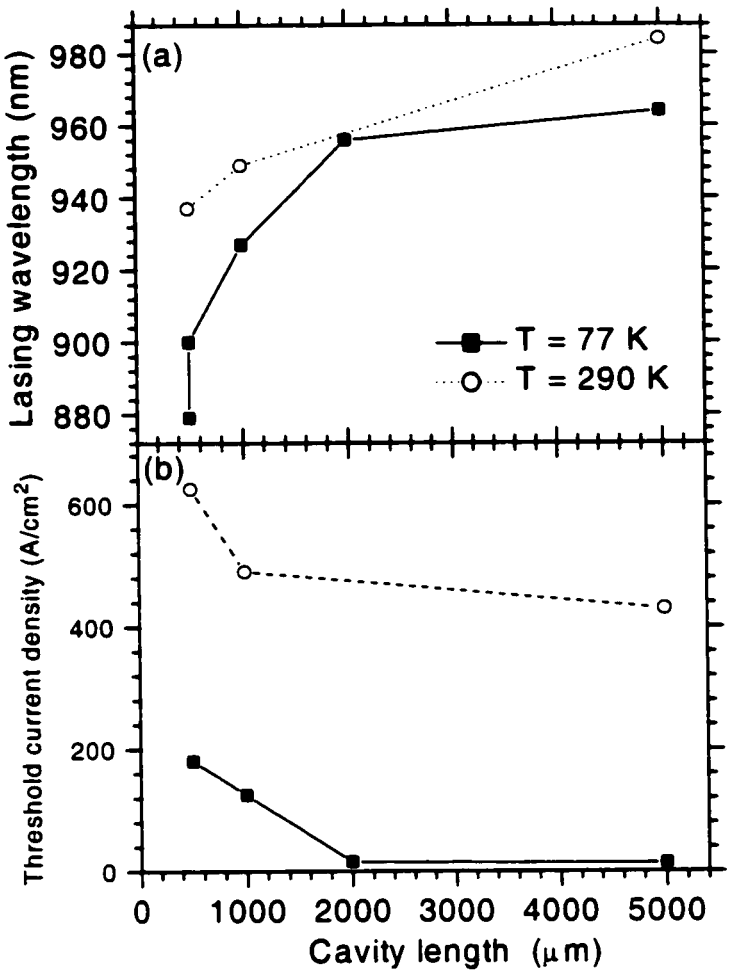

Figure 4.16 (a) Lasing wavelength, and (b) threshold current density for different cavity position at T = 77 K and T = 290 K for sample 2155.

Suris,[152] "A decrease in the QD size dispersion is shown to increase considerably the relative multimode threshold."

4.2.4 Broadband lasing

To understand the effects of the QD density on the laser output, characterization was done on a sample having 30% more InAs material on each layer increasing the dot density above 100 QDs/μm^2 (sample 2084) while preserving the material quality using the indium flush technique,[36] and on a sample having eleven layers in the same active region thickness, bringing down the thickness of the spacer layers to 6.4 nm (sample 2157).

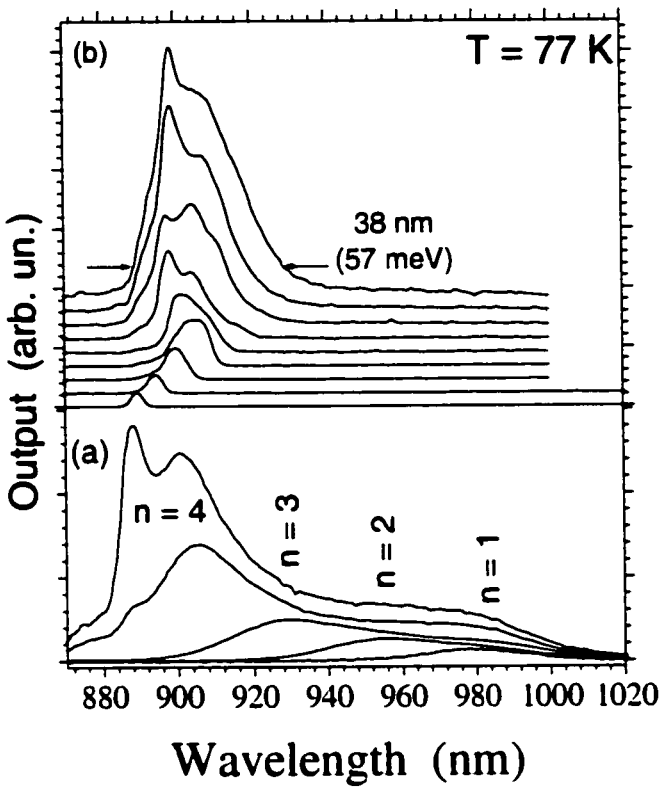

Figure 4.17 Emission at T = 77 K from the stack of eleven layers with a 500 μm long cavity. (a) State filling spectroscopy with current densities varying from 0.003 A/cm^2 (bottom) to 213 A/cm^2 (lasing threshold) (top). (b) Lasing in an excited states for currents between 230 A/cm^2 (bottom) and 4.0 kA/cm^2 (top).

State-filling in the stack of eleven QD layers is shown in figure 4.17. The energy-level positions are very similar to the ones of the stack of seven QD layers. The lowest curve in figure 4.17b displays the lasing threshold spectrum for a 500 μm long cavity positioned at the n = 4 shell. The lasing line has a full width at half maximum (FWHM) of 4 nm (this is limited by the apparatus resolution), therefore only a small portion of the QD ensemble is playing a part in the stimulated emission. As the injection current is gradually increased a widening of the laser line is observed until it covers the whole fourth electronic shell: 38 nm (57 meV), indicating that most of the QD ensemble is playing a part in the stimulated emission. This multimode emission does not follow a

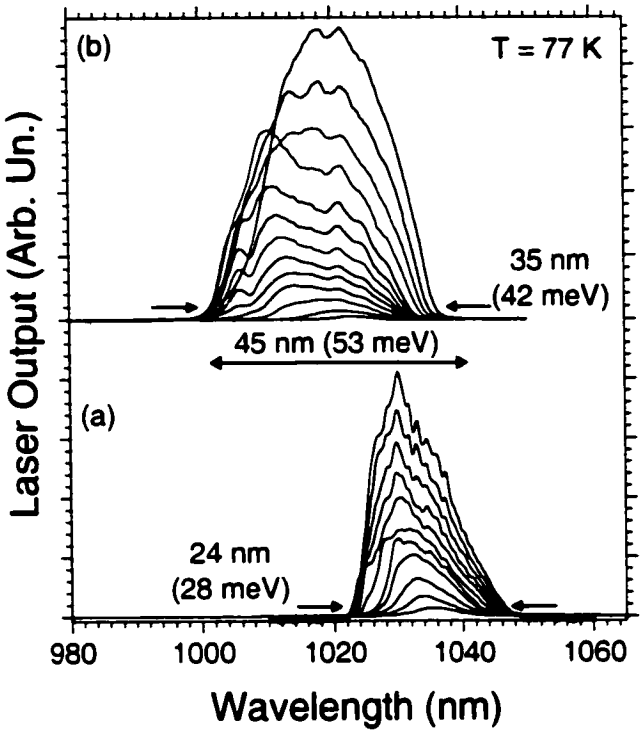

Figure 4.18 Lasing at T = 77 K from sample 2084, the stack of seven layers having a larger QD density: (a) 1300 μm long cavity for current densities between 20 A/cm^2 (bottom) and 120 A/cm^2 (top), and (b) 500 μm long cavity for current densities between 65 A/cm^2 (bottom) and 2.1 kA/cm^2 (top).

Gaussian distribution profile as observed in PL or in spontaneous emission due to nonlinear interactions between different modes.[153] This broad lasing linewidth is also observed in the stack of seven layers with higher dot densities as shown in figure 4.18. In figure 4.18a, for a cavity length of 1300 μm, the lasing linewidth widens from 3 nm to 24 nm (28 meV) as the injection current is increased. In figure 4.18b, for a cavity length of 500 μm, the lasing linewidth widens from 3 nm to 35 nm (42 meV). Together, these two cavities cover a 45 nm wavelength range (53 meV). The peaks modulating the lasing spectra are associated to non-resolved Fabry-Perot lines of the resonant cavity. Using the equation for spacing between allowed modes stated in chapter 3, the mode spacing for

these laser lengths is ~0.1 nm.

4.2.5 Threshold currents

The dependence of the threshold current density as a function of temperature for the InAs QD samples is displayed in figure 4.19. The inset shows that at T = 77 K a large decrease in current is observed for longer cavities. As observed in figures 4.15 and 4.16, the shorter cavity lengths lase in the higher QD shells where more state-filling must take place before threshold conditions are achieved which results in higher onset currents. It appears that threshold for the seven and eleven layers are similar for the various cavity lengths studied. The inset in figure 4.19 show that a large decrease in the threshold current density is observed when increasing the cavity length, in this case from 3600 to 5000 μm, particularly at higher temperatures. The longer cavity emits at a lower energy and it therefore has higher confining barriers in the QD making it less susceptible to thermionic emission of the carriers over the barrier at higher operating temperatures. The threshold curves for the two different stacks of seven QD layers with 5000 μm long cavities display quite different behaviors at higher temperatures. The high QD density sample has a better confining potential since lasing occurs at 1050 nm for this cavity length while the lower dot density sample lases at 964 nm, a difference of 105 meV. Therefore, thermionic emission has less of an effect on the high dot-density seven-layer sample at these higher temperatures. Comparison with the seven layer QW structure can not be done since the emission from these WLs is at higher energy and this results in much lower energy confinements. For sample 2155, T_0 = 46 K; for sample 2157, T_0 = 55

K; and for sample 2084, T_0 = 90 K.

4.3 Concluding remarks

Large lasing linewidths are demonstrated in both systems using multi-layer QD samples. This demonstrates the wide spectral profiles available for this type of zero-dimensional structures. Also, it has been shown that the lasing wavelength can originate from any of the QD shells. Unfortunately, with AlInAs/AlGaAs samples, the inhomogeneity of the QD ensemble does not permit the observation of well-resolved

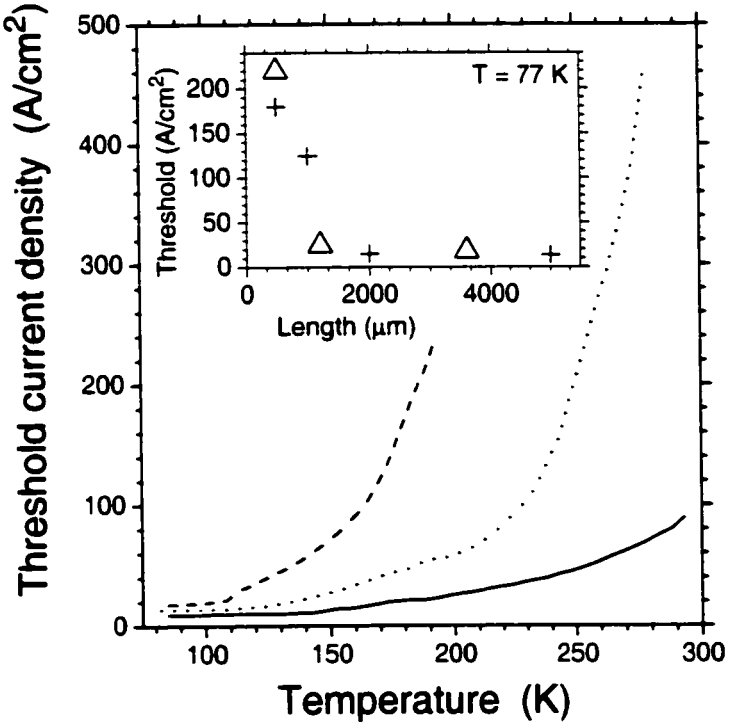

Figure 4.19 Temperature dependence of the threshold current densities for the three InAs QD samples with long resonant cavities: sample 2155, the stack of seven layers (dash), sample 2157, the stack of eleven layers (dot), and sample 2084, the larger dot density stack of seven layers (solid). In inset, threshold current density as a function of the cavity length at T = 77 K for sample 2155 (+), and sample 2157 (Δ).

electronic shells.

The micro-PL mapping technique used on the AlInAs/AlGaAs QDs allows one to probe individual QDs on a laser facet by setting the detection wavelength to a specific energy window of the inhomogeneously broadened QD ensemble spectrum. This is a useful technique for this system since it has a large inhomogeneous broadening of the QD ensemble linewidth. Some reservations must be made regarding the interpretation of the micro-PL spectra since it is difficult to conclude if the measured peaks originate from different level transitions of one QD or are level transitions from different neighboring QDs.

To further understand these systems regarding shell structure and excitonic effects, single QD spectroscopy will be presented in the following chapter. As well, the possible wavefunction coupling that neighbouring QDs may experience in high QD density samples (100 QDs/μm^2 or more), or superposed QDs from adjacent layers in multi-stack samples will be further investigated in chapter 6.

Chapter 5

Spectroscopy of single quantum dots

In this chapter, we use single dot spectroscopy to demonstrate the existence of quantized electron and hole energy levels in $Al_{0.36}In_{0.64}As$ QDs. The chosen samples have low QD densities. The QDs are isolated using the mesa etching technique described in chapter 3. State filling spectra from mesas containing different amounts of QDs are compared. From this, the emission characteristics of a single QD are defined. The excited states and level spacing is obtained by measuring recombination from up to six exciton complexes. In the intermediate pumping intensity regime, we present a magneto-optical study of an exciton, bi-exciton, and charged exciton complexes. These studies give us information on the bi-excitonic binding energy, the excitonic *g*-factor, as well as the intersublevel energy spacing. The measured emission spectra are compared with calculated emission spectra from exact diagonalization studies of exciton, charged exciton, and bi-exciton complexes. Additional information on the exciton and bi-exciton is obtained when perfoming measurements using a micro-PL setup. Finally, the chapters ends with measurements done on single InAs/GaAs QDs.

5.1 AlInAs/AlGaAs QDs

5.1.1 Sample growth

The Stranski-Krastanow growth mode was used to produce a series of single layer QD samples with different amounts of $Al_{0.36}In_{0.64}As$ deposited. The growths were carried out on (100) *n*-doped GaAs substrates. After oxide desorption, a GaAs undoped buffer layer of 300 nm was grown at 630°C. The $Al_{0.33}Ga_{0.67}As$ cladding layer was then grown at 650°C. The strained $Al_{0.36}In_{0.64}As$ layer was deposited at a rate of 0.02 nm/s, followed by a 300 s anneal time, and the deposition of 5.0 nm or 6.0 nm of $Al_{0.33}Ga_{0.67}As$ at 520°C. The temperature was then ramped up to 610°C for 100 s to allow for Indium evaporation. 90 nm of $Al_{0.33}Ga_{0.67}As$ was then deposited at 650°C, and finally, a 5.0 nm thick GaAs cap was grown as the last layer to protect the AlGaAs from oxydation. This structure is

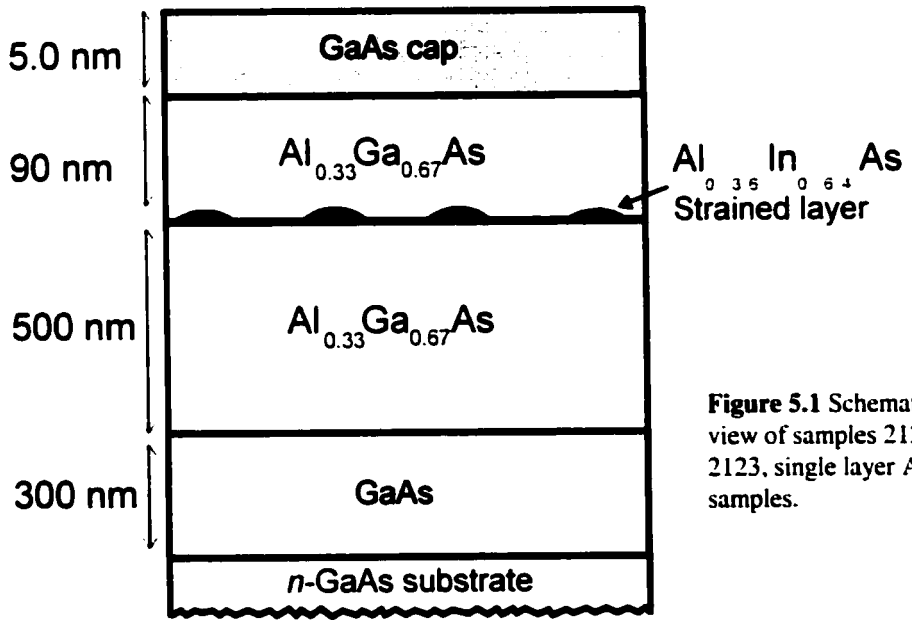

Figure 5.1 Schematic cross-sectional view of samples 2127, 2128, 2134, and 2123, single layer AlInAs/AlGaAs samples.

shown in figure 5.1. Table 4.1 enumerates the samples and their properties.

TEM of the similar samples shown in chapter 4, and in ref. [131] show lens-shaped QDs having base diameters of ~20 nm and heights of ~5 nm.

Sample	Amount of $Al_{0.36}In_{0.64}As$ deposited at 0.031 nm/s	Amount of $Al_{0.36}In_{0.64}As$ deposited	Indium flush
2127	27.5 s	3.0 ML	5.0 nm
2128	28.75 s	3.1 ML	5.0 nm
2134	29.5 s	3.2 ML	6.0 nm
2123	30.0 sec	3.3 ML	5.0 nm

Table 5.1 AlInAs/AlGaAs samples.

5.1.2 Ensemble photoluminescence

Fig. 5.2 shows the evolution of the low temperature PL spectrum with increasing excitation intensity for the four samples. The excitation has been carried out with the 514 nm line of an Ar^+ laser, or the 532 nm line of a Nd:YVO_4 laser above the $Al_{0.33}Ga_{0.67}As$ barrier. For sample 2127, the sample with the least strained material deposited, two peaks are visible: the WL peak at 1.90 eV (656 nm), and the emission from the barrier material, i.e. bulk $Al_{0.33}Ga_{0.67}As$ at 1.99 eV (622 nm). No QD emission is observed. For the second sample, sample 2128, at very low excitation intensity a peak appears centered at ~1.72 eV (720 nm) with a FWHM of ~ 50 meV, as the excitation intensity is increased, the emission peak becomes asymmetric and widens toward higher energies.[9] Some features

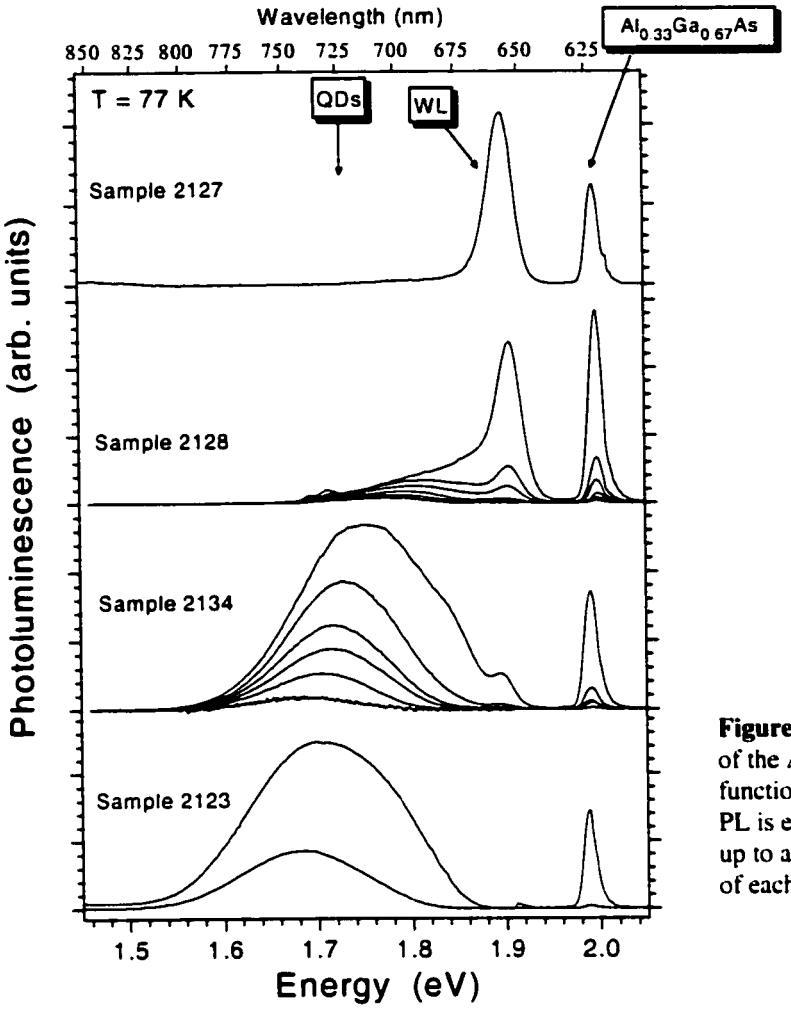

Figure 5.2 State filling spectroscopy of the AlInAs/AlGaAs samples as a function of excitation intensity. The PL is excited with various intensities up to a few kW/cm^2 for the top curve of each sample.

are observed on the low energy side of the saturated QD emission peak. As well, at higher excitation intensities, the peaks from the WL emission and the bulk $Al_{0.33}Ga_{0.67}As$ dominate the spectra, indicative of a very low QD density sample. For sample 2134, at low excitation intensities, the QD peak is centered at ~1.68 eV (738 nm) with an inhomogeneous linewidth of ~100 meV. This value is twice the value observed for sample 2128 and the same state filling as for sample 2128 is observed. But, it should be noted that even at higher excitation intensities, the QD emission dominates the spectra. As the amount of $Al_{0.36}In_{0.64}As$ material is increased, a red-shift of the QD PL emission is observed, this is confirmed when looking at the emission spectra of sample 2123. For this

sample, the WL is no longer observed.

Samples 2128 and 2134 both have a WL signal in their spectra indicating samples with low QD densities (1-50 QD/μm^2). They are therefore good candidates for single QD spectroscopy. As the PL shows, in this ternary/ternary system, the emission from the different QD shells remains unresolved when probing large amount of QDs.

5.1.3 Single quantum dot photoluminescence

Fig. 5.3 displays the effects of reducing the number of QDs probed to a 5 μm mesa on sample 2134. If the QD density of this sample is set as ~10 QDs/μm^2, then more than 1000 QDs are probed. At low excitation, the PL spectra display distinct extremely narrow lines. As the excitation intensity increases, the lines increase in intensity. Three of these lines have been marked by dashed markers. The FWHM of the ensemble is measured to be 90 meV at low excitation intensities, which corresponds well with the measurement made on the ensemble shown in the previous figure. This data is similar to measurements obtained at the University of California at Santa Barbara and at the Australian National University by Leon et al.[23] and Fafard et al.[27]

Figure 5.4 presents results on four mesas with sizes less than half a micron. As the probe area is reduced from a 5 μm wide mesa down to a 300 μm mesa, the inhomogeneous broadening vanishes and only sharp emission lines originating from individual QDs are present. Arrows are used as guides to the eye to indicate emission from possible single QDs. The lowest energy spectra of the mesa labeled "below P2" at 1.9 μW excitation intensity has no features, but at 5.2 μW, at least nine faint lines appear

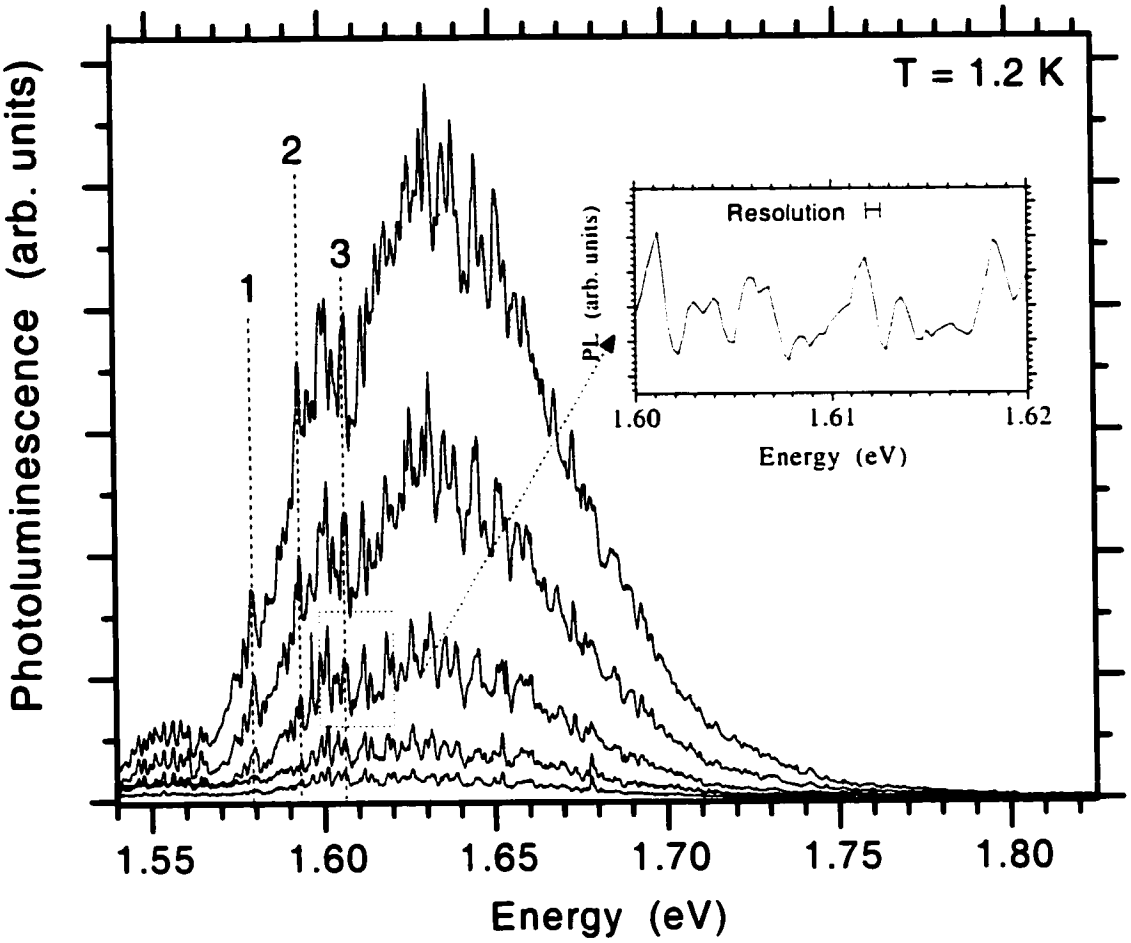

Figure 5.3 PL spectra from a P1 mesa of sample 2134 having 5 μm side lengths for excitation intensities varying from 1.9 μW (lowest curve) up to 130 μW (top curve) with a spectral resolution of 1.0 meV. The inset shows an expanded scale of one of the spectrum.

which grown in intensity as the excitation intensity is increased to 305 μW. As well, as the excitation intensity is increased, additional lines appear. For the mesa C8, five faint emission lines are detected at low excitation intensity, while for mesa B7 and B2, only three faint lines are present at low excitation intensity. Again for these smaller mesas, additional lines appear as the excitation intensity is increased. This type of spectra is characteristic of the spectra observed for most fields having dimensions between 600 and 300 nm.

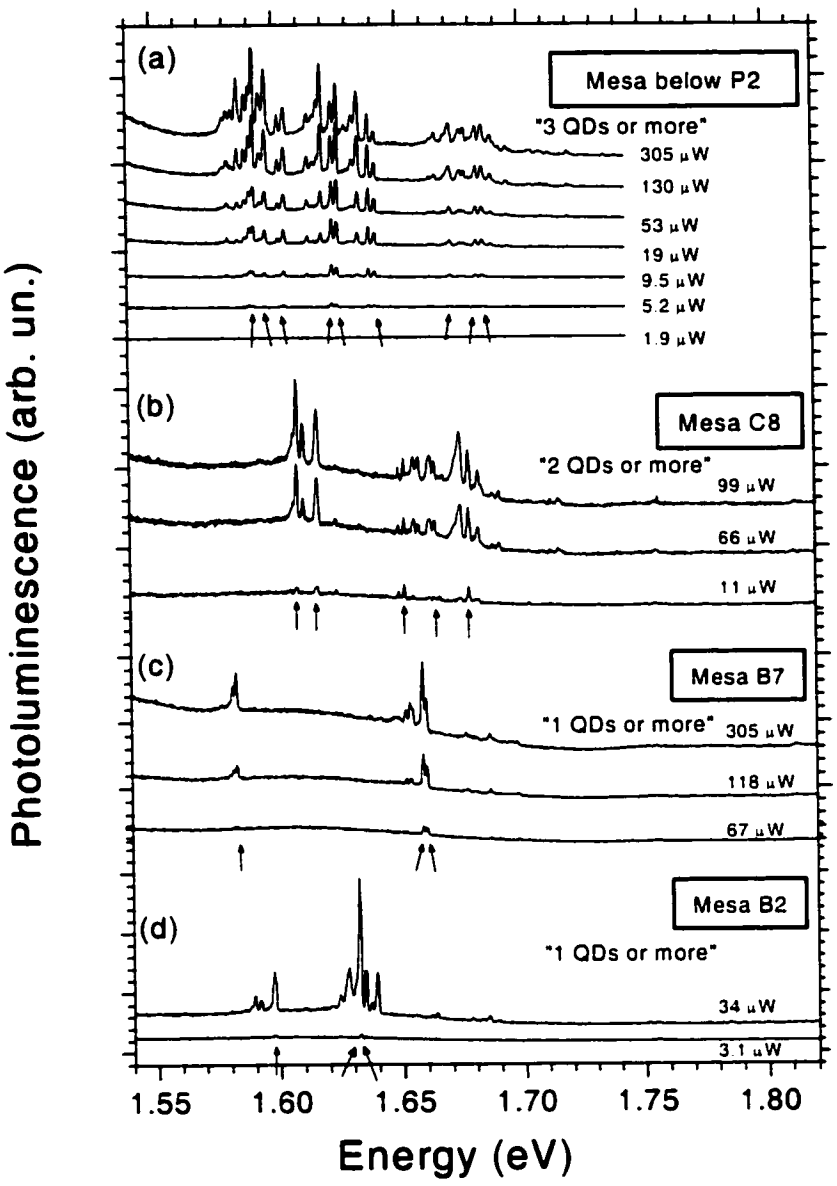

Figure 5.4 PL spectra from various mesas of sample 2134 taken as a function of excitation intensity at T = 2 K. The arrows indicate single line emission. The mesa named "below P2" arises from artifacts of the etching and its dimensions are unknown.

A linewidth of ~1.0 meV is measured for these sharp lines. Two possible factors can explain this line broadening, first the processing used for etching down material to isolate a single QD introduces surface defects on the walls of the pillar containing the QDs. These defects can get charged and discharged as a function of time (of the order of a

nanosecond) and may lead to small variations in the QD confinement potential. When performing a measurement that lasts for seconds, these variations in confinement get averaged out increasing the homogeneous linewidth of ~0.1 meV[28] to ~1 meV. As well, above barrier excitation can lead to linewidth broadening due to the presence of a large phonon population in the sample.

Figure 5.5 illustrates a mesa having probably two QDs. At very low excitation intensity, only two peaks are present in the spectrum, they are labeled 1 and 2 in the

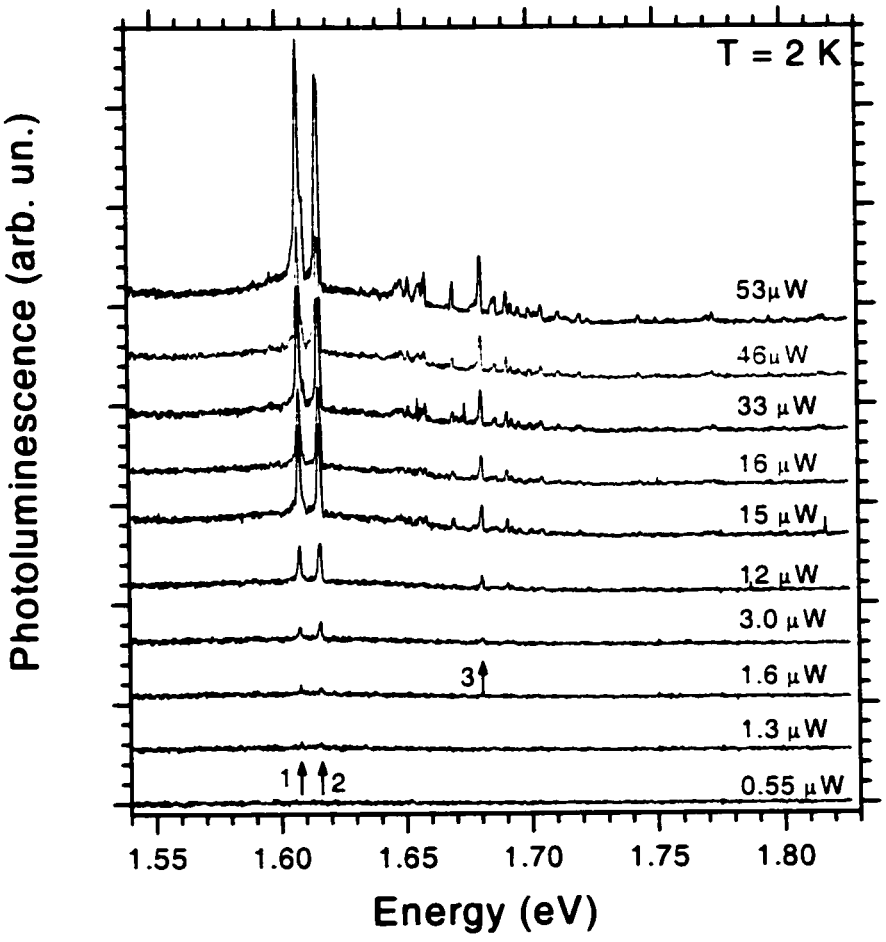

Figure 5.5 PL spectra from mesa C7 of sample 2134 taken as a function of excitation intensity.

figure. Peak 1 is positioned at 1.608 eV, peak 2 is positioned at 1.616 eV, 8 meV one from the other. Both of these peaks increase in intensity in a similar fashion, at I_{ex} = 3.0 μW, a third peak appears at 1.681 eV, 65-73 meV higher energy than peaks 1 and 2. Starting at I_{ex} = 12 μW, additional peaks appear around peak 3, although peak three stays dominant until the highest excitation intensity (53 μW). Also starting at I_{ex} = 16 μW, on the high energy side of peak 1, a new peak appears which increases faster than peaks 1 or 2 in intensity. These behaviors will become clear after studying single QDs as shown below.

When probing small enough mesas, spectra originating from what is believed to be a single QD can be observed. Figure 5.6 displays spectra from various mesa of this kind with a certain level of state filling. All the mesas have a dominating peak, except for mesas C2 and F7, surrounded by fainter peaks located at most 15 meV one from another. Most of these fainter peaks are located at a lower energy than the main peak, an exception is mesa D7 which has a distinct peak located 8 meV higher energy than its main peak at 1.628 eV. The peaks are all located within the range of the low intensity ensemble PL of mesa P1. Listed on the right of the figure is the excitation energy used to observe this type of state filling. The excitation intensity increases an order of magnitude between mesa C12 (I_{ex}= 20 μW) and mesa F5 (I_{ex}= 700 μW). When performing state filling spectroscopy on an unetched sample, the same excitation intensity is needed to observe equivalent state filling on any part of the sample. The differences in excitation intensity could be caused by 1) the position of the single QD with respect to the center of the mesa, 2) the quality of the mesa (e.g. etch roughness), or a combination of both these factors. It has been shown that the PL signal originating from QDs near surfaces is quenched,[145] as

well, the carriers trapped at surfaces typically recombine nonradiatively, wasting photocarriers generated near the surface in the absence of passivation.[154] At the higher excitation intensities, a background arising from the bulk GaAs starts to dominate the spectra at lower energies, as is clearly observed in mesas F7 to C2. This is due to the large (20 μm) excitation spot size, compared with the mesa dimensions (< 1μm).

The mesa needing the least excitation intensity to obtain some state filling, mesa C12, was selected for detailed study as a function of excitation intensity, the results are

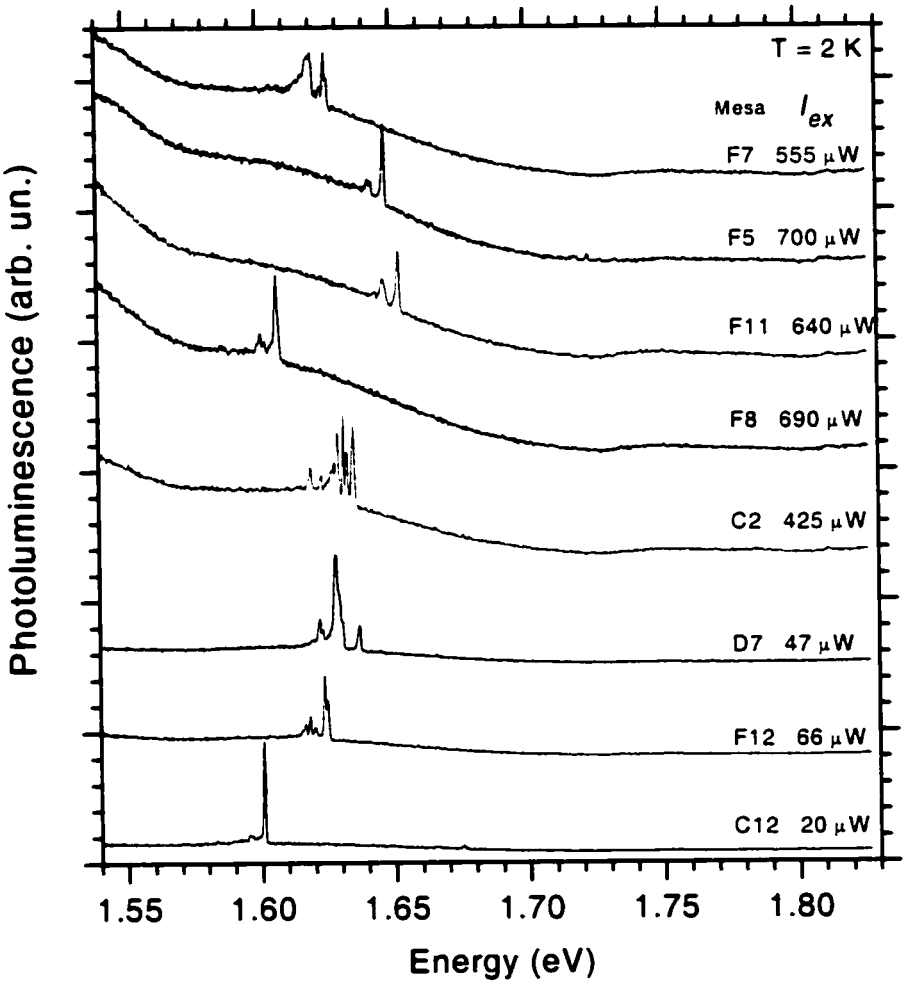

Figure 5.6 PL spectra from various mesas of sample 2134 recorded at nominally equivalent state filling.

presented in figure 5.7. The QD emits in the lower energy range of the QD spectrum and background reference spectra were taken for the higher excitation intensities by recording the spectrum just off the mesa and then subtracting it to the acquired QD spectrum. At low excitation powers, only one sharp line is visible at 1.6008 eV. This is attributed to recombination of single electron-hole pairs. As the excitation intensity is increased above 20 μW, a second peak appears at 1.5952 eV below the exciton line. At a pump intensity of 66 μW, two closely spaced peaks are observed at much higher energy, one at 1.6691 eV and the other at 1.6750 eV. In addition, many mostly unresolved peaks are observed over a range of ~20 meV located just below the first two dominating peaks around 1.60 eV. By increasing the excitation intensity an order of magnitude higher, we are unable to fill the states much more, the background intensity rises in a disproportionate manner compared with the QD emission, and it becomes difficult to perform a correct background subtraction.

In order to explain the spectra further, we must look at a model for confined energy levels of QDs.[155,156,157] Other possible model are also available[158,159,160] but the experimental results will be compared with the theory by Hawrylak et al. from ref. [156]. This model starts with the single particle states of self-assembled indium-based QDs. The bound states of both electrons and valence-band holes of a lens-shaped QD can be represented using an effective parabolic potential. The electronic energies

$$E^{e}_{m\,n} = \Omega^{e}_{+}\left(n+\tfrac{1}{2}\right)+\Omega^{e}_{-}\left(m+\tfrac{1}{2}\right), \tag{5-1}$$

eigenstates $|m\,n\rangle$ and angular momenta

$$L^{e}_{m\,n} = m-n, \tag{5-2}$$

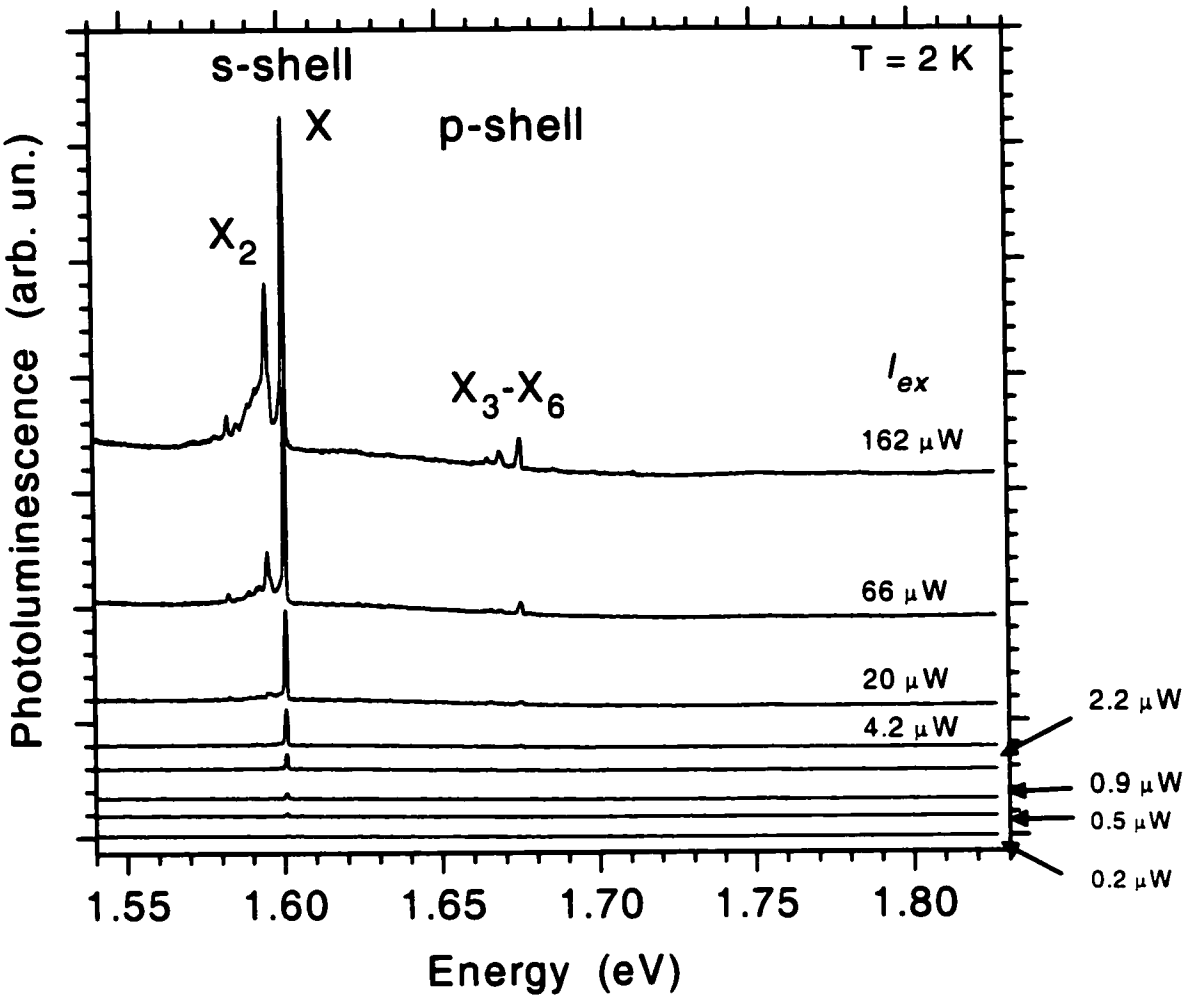

Figure 5.7 PL spectra from mesa C12 of sample 2134 for excitation powers varying from 0.1 W/cm^2 up to 50 W/cm^2.

are those of two harmonic oscillators tunable with magnetic field B applied normal to the plane of the QD. The frequencies

$$\Omega_{+/-} = \tfrac{1}{2}\left(\sqrt{\omega_c^2 + 4\omega_0^2} \pm \omega_c\right), \tag{5-3}$$

where $\omega_c = eB/m_c^*$ is the cyclotron energy, m^* is the effective mass, and e is the charge of an electron. The magnetic length l_0 is given by

$$l_0 = 1/\sqrt{m^* \omega_c}\,, \tag{5-4}$$

and the effective length

$$l_{eff} = 1/\left[1+\left(4\omega_0^2/\omega_c^2\right)\right]^{1/4}. \tag{5-5}$$

The splitting of different spin σ energy levels (Zeeman energy) is very small compared to

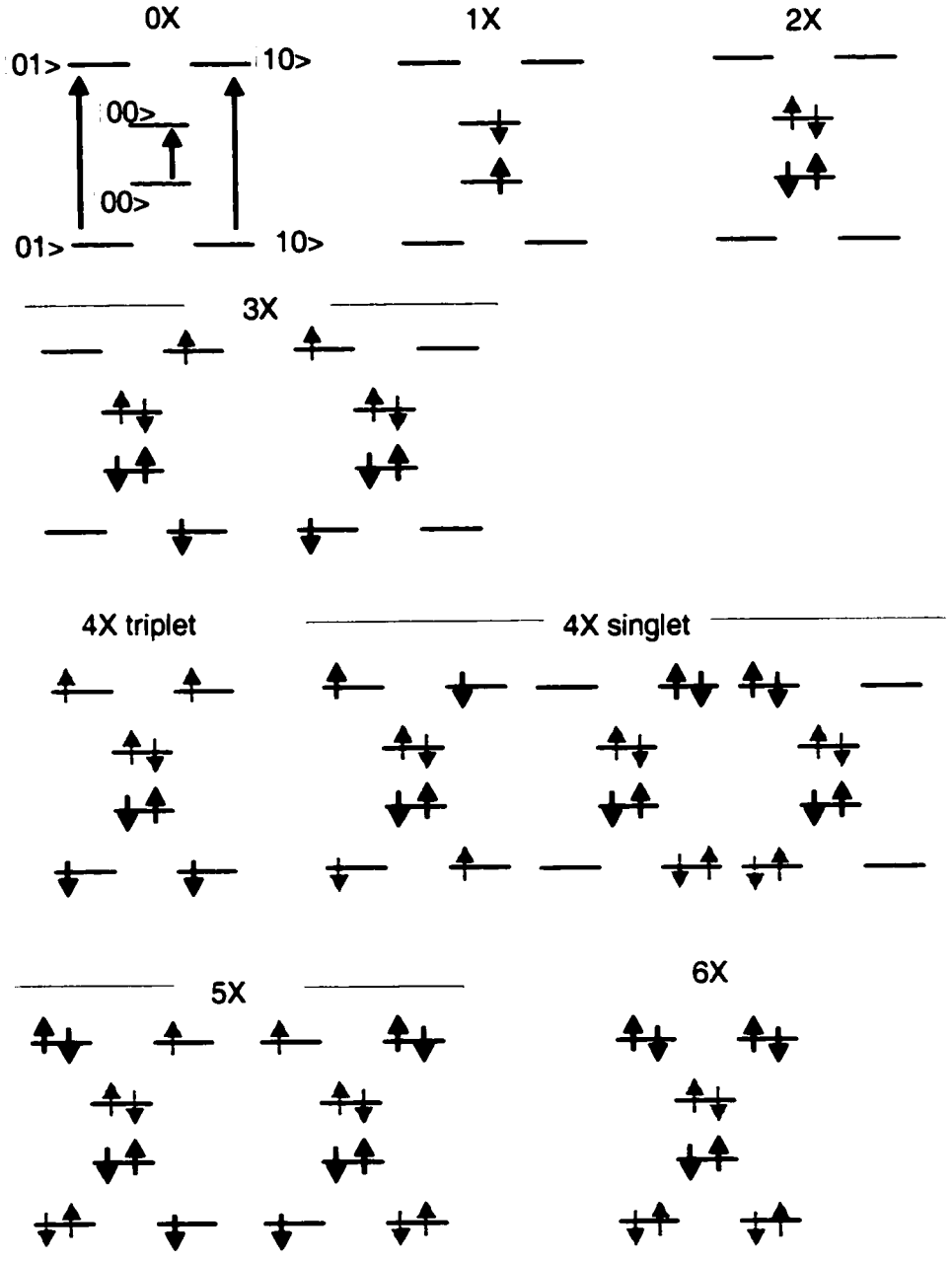

Figure 5.8 Lowest-kinetic-energy configurations of a QD from zero to six excitons. In the diagrams, the three highest energy levels are for the electrons in the conduction band, while the three lowest are for the holes in the valence band. The states are denoted $|m\,n\rangle$, and the allowed radiative transitions are shown with arrows in the 0X diagram. A singlet has a total spin $S = 0$, a triplet has a total spin $S = 1$. From ref. [156].

other energies.

Due to strain in the structure, the heavy and light holes are split at $k = 0$, and the valence-band hole is treated in the effective-mass approximation as a positively charged particle with angular momentum

$$L^h_{m\,n} = n - m, \tag{5-6}$$

opposite to the electron, and energies

$$E^h_{m\,n} = \Omega^h_+ \left(n + \tfrac{1}{2}\right) + \Omega^h_- \left(m + \tfrac{1}{2}\right), \tag{5-7}$$

(ignoring the semiconductor gap E_G).

An example of the single particle configuration of a two-shell QD is shown in figure 5.8. These QD shells are populated with an increasing number of carriers according to the Pauli exclusion principle. The s-shell is two-fold spin degenerate and cannot be occupied by more than two electron-hole pairs, the p-shell is doubly degenerate and can hold a maximum of four electron-hole pairs.

The Hamiltonian of interacting electrons and holes confined in the QD can be written:[156]

$$\begin{aligned} H = &\sum_i E^e_i c^+_i c_i + \sum_i E^h_i h^+_i h_i - \sum_{ijkl} < ij \mid v_{eh} \mid kl > c^+_i h^+_j h_k c_l \\ &+ \frac{1}{2}\sum_{ijkl} < ij \mid v_{ee} \mid kl > c^+_i c^+_j c_k c_l + \frac{1}{2}\sum_{ijkl} < ij \mid v_{hh} \mid kl > h^+_i h^+_j h_k h_l . \end{aligned} \tag{5-8}$$

The operators c_i^+ (c_i) and h_i^+ (h_i) create (and annihilate) the electron and valence-band hole in the state $|i\rangle$ with the single particle energy E_i. The two-body Coulomb matrix elements are $\langle ij|V|kl\rangle$ for electron-electron (ee), hole-hole (hh), and electron-hole (eh) scattering, respectively. The typically smaller confining potential for holes is partially

compensated for by their heavy mass, and the strength of the electron-electron and hole-hole interactions are assumed equal. The scaling of single particle spacing implies that kinetic energy dominates and effects of interaction involving intershell transitions can be treated pertubatively. For states forming degenerate shells, Coulomb interactions completely determine the spectrum.

The interband optical processes in a QD are described by the set of interband polarization operators P_σ^+ $\left(P_\sigma^-\right)$ which create (annihilate) electron-hole pairs with definite spin configuration by annihilating (creating) photons with definite circular polarization. The remaining electron-hole pair spin configurations (σ,σ) correspond to dark excitons.

At very low excitation intensity, the QD is either empty or only one electron–hole pair is present in the s-shell. The resulting emission line (X) clearly originates from a single exciton decay in the s-shell. As the pump power increases, a second peak appears 5.0 meV below the exciton peak, and increases superlinearly with excitation power. This line is immersed in a growing background. We assign this line to the radiative recombination of a bound bi-exciton (2X) into a single exciton state. The group of lines around the bi-exciton line is assigned to the recombination of charged excitons. The energy shift of the bi-exciton line relative to the exciton line arises from the exciton-exciton Coulomb interaction in the QD and can be considered as the bi-exciton binding energy, the difference between the energies of two uncorrelated excitons and the energy of the two-exciton complex. This value for the bi-exciton binding energy is larger by ~2 meV compared with values observed in InAs/GaAs QDs.[41,43,44] The appearance and

growth of the bi-exciton line is followed by some filling of the second shell, located at an energy ~70 meV higher than the lowest shell. The two peaks observed in the second shell are associated to recombination of the three-exciton (3X) up to the six-exciton (6X) complexes. This is supported by the appearance of additional lines in the s-shell region which are attributed to multi-carrier interactions arising from the addition of the third to sixth exciton in the QD.[44,156,157] The exciton and bi-exciton line observed at lower pumping powers are still present in the spectra since statistically at these pump powers, the probabilities of having only one or two electron hole pairs is still high.[109] These two peaks could also be due to recombination of excited states of the exciton and/or bi-exciton, where only one exciton at a time is promoted to the second shell[41,156] although this would not explain the appearance of additional peaks in the lowest shell at higher pump powers.

We are only able to weakly populate the first excited states. However, since the emission from the WL occurs at 1.89 eV and emission from the lowest QD level is at 1.60 eV, we can expect the dot to have approximately four or five groups of bound states (e.g.: 1.60, 1.67, 1.74, 1.81 and 1.88 eV assuming equal spacing of levels). This number of excited states is similar to the one observed in In(Ga)As QDs.

5.1.4. Single quantum dot magneto-photoluminescence

Figure 5.9 shows PL spectra of a single QD at different magnetic fields.[161] The excitation power was increased to a level where some biexciton contribution appears in the spectra. The exciton recombination at B = 0 T is located at 1.6002 eV. In addition,

further emission lines are observed ~5 meV below the exciton, that will be discussed later. In order to facilitate the discussion of these lines they have been enlarged by a factor of 2.

Let us first address the behavior of the exciton: as the magnetic field is increased, the exciton emission splits into σ^- polarized at higher energies, and σ^+ polarized at

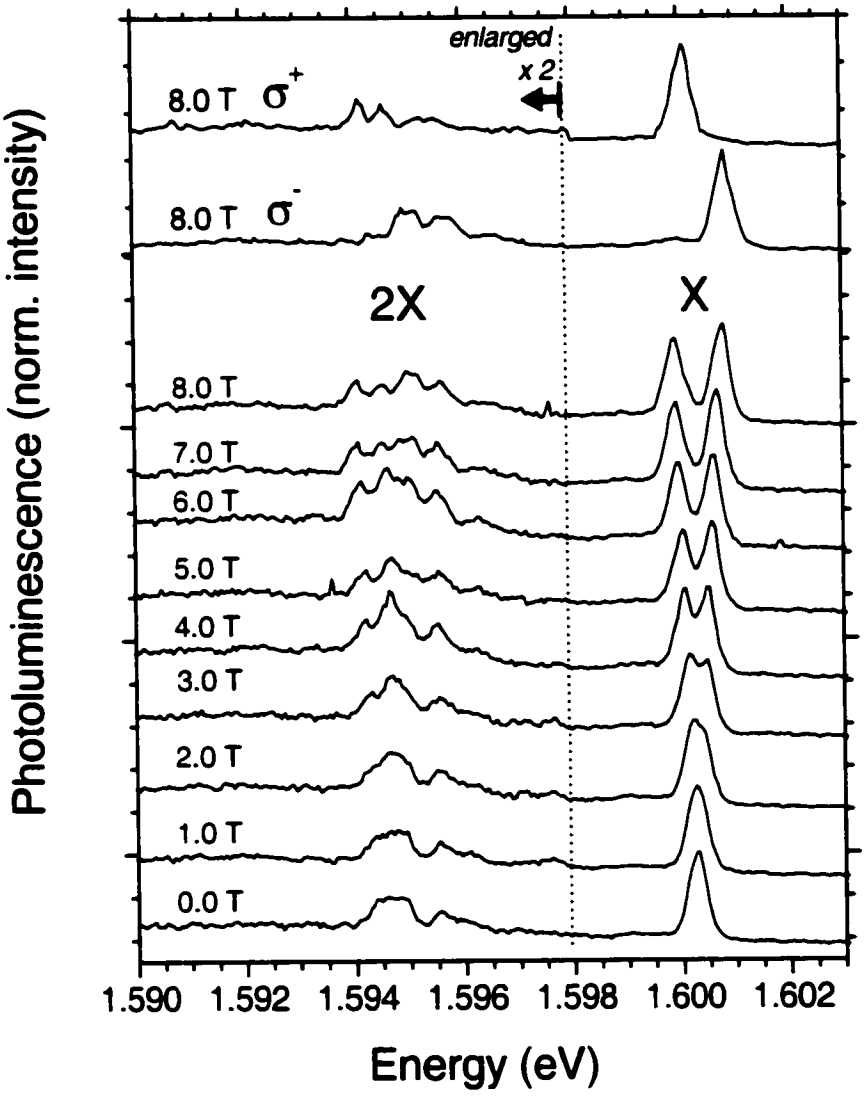

Figure 5.9 Single QD PL spectra recorded at different magnetic fields of mesa C12, sample 2134. Top two curves are polarized PL spectra recorded at B = 8.0 T. From ref. [161].

lower energies (see the polarization resolved spectra at the top of figure 5.9). This is due to the Zeeman splitting of the exciton, $\Delta E_{\pm} = g_X \mu_B B$, where g_X is the exciton g factor and μ_B is the Bohr magneton. The spins of generated/annihilated particles (electrons and holes) are governed by the polarization of absorbed/emitted light. In the case of emission, the polarization of the emitted photon reflects the spin configuration of the pair at the moment of recombination. This is illustrated in figure 5.10. Due to strain between QD and substrate, the heavy and light holes are strongly split in energy so that the light holes can be neglected in the analysis.

The energy of an exciton in magnetic field can be written as:

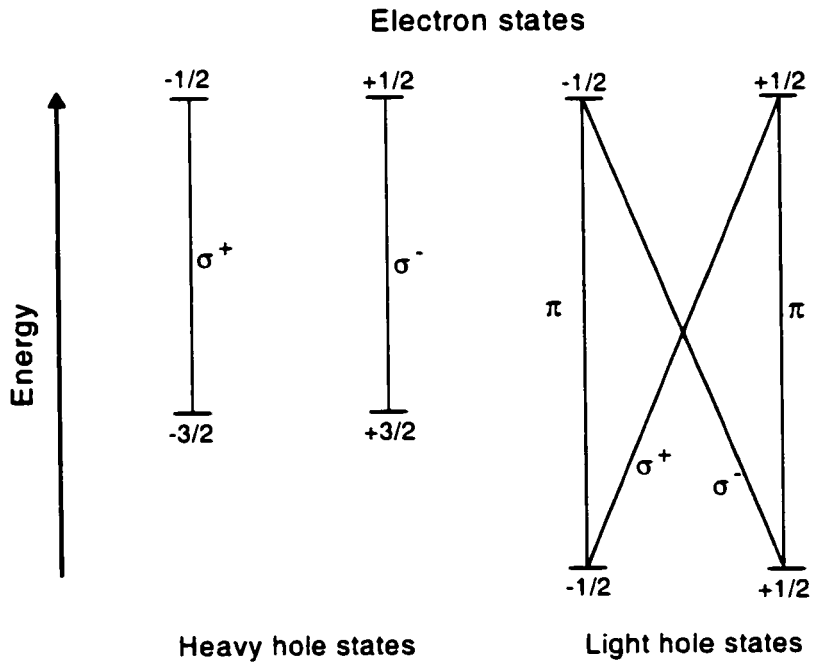

Figure 5.10 Interband optical transitions between the heavy-hole ($j = \pm 3/2$) and light-hole ($j = \pm 1/2$) subbands of the valence band ($m = \pm 1$), and the conduction band ($m = 0, j = \pm 1/2$) for the two circular polarizations of light: σ_+, σ_-, and linear polarization π.

$$E_X = E_n + \frac{e^2\langle r^2\rangle B^2}{8m^*} - \frac{el_B}{2m^*} + g_X \mu_B B \qquad (5\text{-}9)$$

The first term E_n is the energy of the shell, where $n = 1$ for s-shell, $n = 2$ for a p-shell. The second term refers to the diamagnetic shift, where $\langle r^2 \rangle$ is the mean square lateral extension of the exciton. The third term refers to the orbital shift where $l_B = \sqrt{\frac{\hbar c}{eB}} \Big/ a_B$ is the magnetic length measured in Bohr radii a_B; this term does not affect s-type levels. The last term refers to the spin splitting.

In figure 5.11a, the energies of the spin polarized exciton emission line are plotted versus magnetic field. Within the experimental accuracy, the spin-splitting between the two emission lines increases linearly with B, as shown in figure 5.11b. At $B = 8.0$ T, the splitting is as large as 0.9 meV. From the linear regression in figure 5.10b, we obtain an excitonic g factor $g_X = 1.97 \pm 0.04$. A number of single QDs were studied in this way, and the spin splitting changed only slightly from dot to dot by about $\pm$ 0.1 meV. Such small variations are indicative of a high quality material.

Additional information about the exciton can be obtained by looking at the magnetic field dependence of the center of the exciton doublet in figure 5.11a, where we observe only a slight diamagnetic shift to higher energies with increasing magnetic field. The shift is less than 0.1 meV in the range of 0 to 8 T, resulting in a diamagnetic coefficient of 0.8±0.3 μeV/T^2. This value is smaller than the 2.6±0.4 μeV/T^2 measured in an earlier study on $In_{0.55}Al_{0.45}As/Al_{0.35}Ga_{0.65}As$ QDs, although in that case, the shift was measured on a large QD ensemble.[162]

For strong geometric confinement the diamagnetic shift can be approximated[163] by

$$\Delta E^{X}_{diamag} = \frac{e^2}{8}\left(\frac{\langle r_e^2 \rangle}{m_e} + \frac{\langle r_h^2 \rangle}{m_h} \right) B^2, \qquad (5\text{-}10)$$

where $\langle r^2_{e/h} \rangle$ are the mean square lateral extensions of the electron and hole wavefunctions in the QD, respectively. Assuming equal extensions for electron and hole we obtain $\langle r^2_{e/h} \rangle^{1/2}$ ~1.5 nm from the experimental shift which is much smaller than the estimated QD radius of ~ 10 nm. This would indicate that the exciton s-shell type orbital would be mostly confined in the center of the QD.

Now let us turn to the discussion of the low energy lines in the spectra in figure 5.9. As indicated above, at B = 0 T the emission consists of two prominent lines, one rather broad emission band located at ~ 1.5945 eV and one at slightly higher energies ~ 1.5956 eV. The latter one shows no dependence on magnetic field (neither a diamagnetic shift nor a spin-splitting). Furthermore, it does not show a superlinear dependence on excitation power as does the other feature. Therefore it is unlikely that it originates from the recombination of excitonic complexes in the QD. It might be related to defect recombination, however its origin is not clear yet.

The low energy band shows some structure indicating that it might consist of several emission lines, as is also suggested by its large linewidth as compared to the exciton recombination. However, the small energy separation between them prevents the spectral resolution of the several features. Information on the number of spectral lines at B = 0 T can be obtained from the magnetic field studies due to spin splitting. In high fields four prominent lines are observed. Their magnetic field dependencies are quite

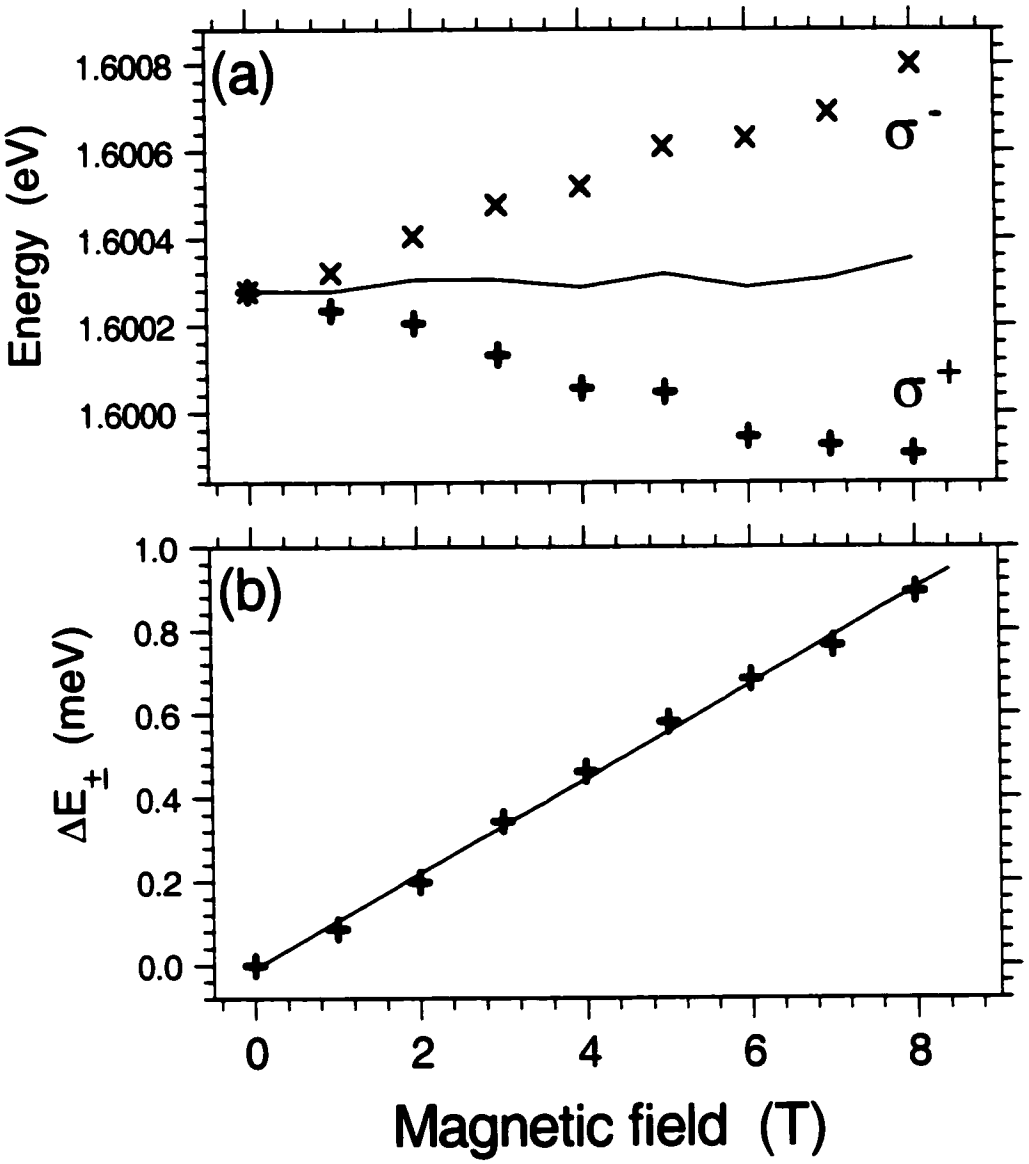

Figure 5.11 (a) Exciton energies as a function of the magnetic field. The transitions are labeled corresponding to their different circular polarizations. The solid line corresponds to the center of the exciton doublet. (b) Zeeman splitting of the exciton versus magnetic field.

similar to that of the exciton. The polarization analysis shows that the two lines at lower energies are σ^+ polarized, while the lines at higher energies are σ^- polarized. From the magnetic dependence we can trace back that the energies of the two low energy lines of opposite polarization converge for $B \rightarrow 0$ as do the energies of the high-energy doublet.

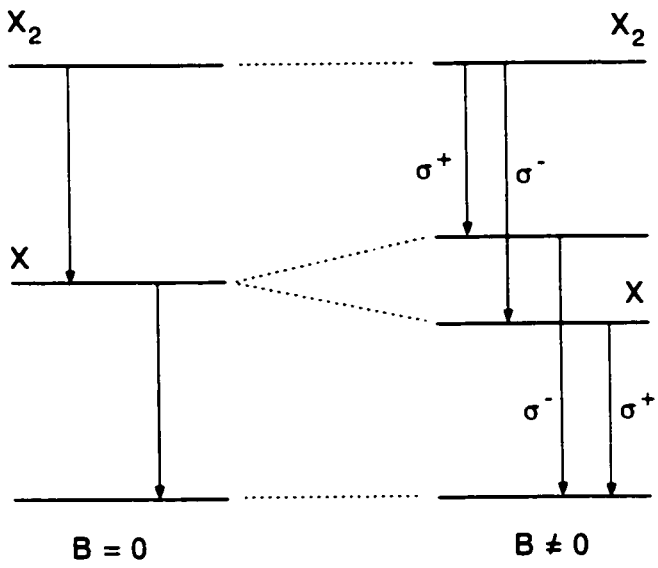

Figure 5.12 Scheme of optical transitions from the exciton and biexciton states at zero and nonzero magnetic fields.

From this observation, we conclude that the zero field emission is mainly a superposition of two spectral lines (the indications for weak additional emission features will be discussed).

However, only one of the two main B = 0 T emission lines can be recombination from the bi-exciton. It should be noted that the bi-exciton is a spin singlet state and thus its energy cannot be split by a magnetic field. However, the final state of the bi-exciton transition is an exciton,[115] as indicated by the transition scheme in figure 5.12. The spin splitting of the biexciton emission is given by the Zeeman splitting of the exciton. Therefore, the splitting of the biexciton is identical to that of the exciton.

The other feature could be associated with emission from a singly charged exciton which would also split in the same way as the exciton peak as a function of magnetic field, because the splitting is given by the *g*-factors of the recombining electron-hole pair. Since the charged exciton can have negative and positive charge (X^- or X^+), in general, six emission lines can be expected in the spectra, while from experiment we obtain evidence

for four lines only. This might have two reasons: (a) First, the creation of one of the charged excitons might be suppressed. To mention only one mechanism for suppression,

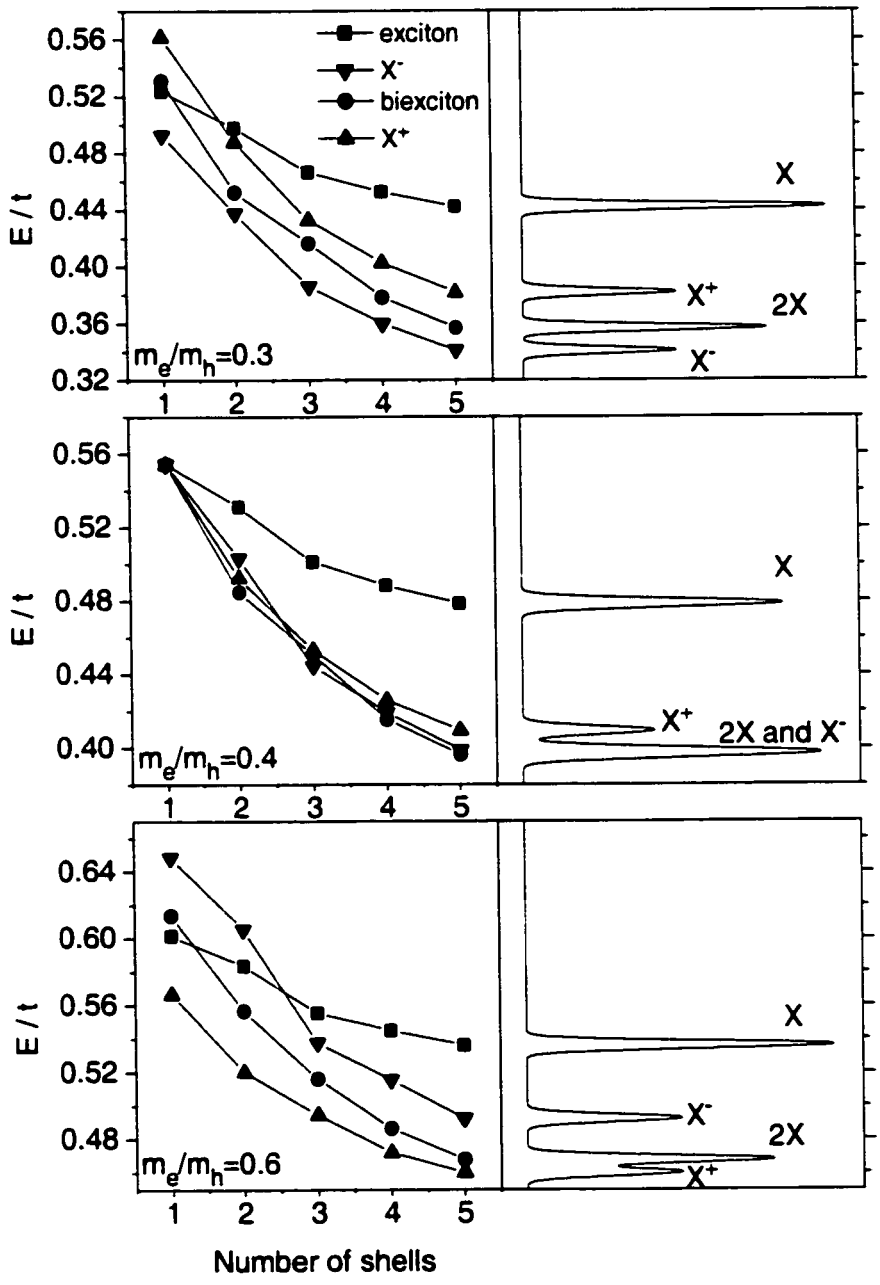

Figure 5.13 Calculated exciton, bi-exciton, and negatively and positively charged exciton emission energies as a function of the number of confined shells for three different ratios of the electron to hole mass. The right hand side shows the possible emission spectrum for five shells with the arbitrary assigned oscillator strength of each transition. The actual intensities depend on the average population of each species. Modeling by Hawrylak and Korkusinski from ref. [161].

in the case of X^-, for example, one could imagine that an electron of a trapped exciton tunnels through the AlGaAs barrier that surrounds the QD towards a defect state at the lateral sidewalls of the field leaving behind a hole in the dot. Together with an additional exciton, this hole will form the X^+ complex. (b) The energy of one of these complexes might be degenerate with the energy of the biexciton.

We note that there are also indications for other emission lines in the spectra, which are, however of rather weak intensity. The appearance of additional emission lines in the spectra becomes possible if the rotational symmetry of the QD system is broken.[164] In this case angular momentum is no longer a good quantum number and a mixing of bright and dark excitons can occur resulting in an observation of the dark states. Indeed one notes, for example, that the σ^- polarized component of the exciton shows some high-energy shoulder, which might arise from recombination of a predominantly dark state. These dark states would naturally also show up in the recombination of the bi- or the charged exciton complexes, because a predominantly dark electron-hole pair can decay due the symmetry breaking.

This assignment is supported by calculations of the emission spectrum from the exciton, bi-exciton, and a negatively and positively charged exciton in a QD using the Hamiltonian of interacting electrons and holes of ref. 156. We assume an energy level spacing of 50 meV for the electrons and 20 meV for the holes which gives the level spacing of t = 70 meV. The level spacing t is an important input parameter that circumvents our lack of knowledge of the microscopic parameters of the QD. The ratio of electron to hole level spacing is unknown but consistent with simultaneous capacitance

and PL measurements on InAs QDs by Schmidt *et al.* in ref. 165. The remaining parameters are the ratio of the electron to hole mass and the number of confined shells. Figure 5.13 shows the emission energies from an exciton, bi-exciton, and a negatively and positively charged exciton as a function of the number of shells for three different ratios of the electron to hole mass. We see that the emission energies depend both on the number of shells and on the ratio of masses. The position of the emission line is strongly renormalized by Coulomb interaction of the carriers in the QD. For a single shell this renormalization accounts for ~50% of total kinetic energy quantization. The renormalization depends further on the type of complex through the number of single particle levels. This is because different complexes are built from a different number of configurations. For five shells, the number of exciton configurations is N_X = 29, bi-exciton configurations N_{2X} = 1276, and charged exciton X^- is N_{X^-} = 186. The differences in the energy of the bi-exciton and charged exciton recombination line appears to be <0.02*t*. The chosen ratio of electron and hole effective masses $m_e/m_h = 0.4$ signifies that the electron-electron, hole-hole, and electron-hole interactions are almost identical (symmetrical interactions). In this case, the exciton acts as a neutral complex, a picture consistent with the presence of almost degenerate levels associated with the recombination from the p-shell. Assuming therefore $m_e/m_h = 0.4$, the bi-exciton binding energy $\Delta E_{2X} = E_{2X} - 2E_X$ is found to be 5.1 meV, which agrees with the measured value. Similarly, the charged exciton (X^-) emission energy is given by $\Delta E_{X^-} = E_{X^-} - E_X - T_e$ where T_e = 50 meV is the single-particle kinetic energy of the electron. The calculated charged exciton binding energy is 4.8 meV, which could

correspond to the weak additional peak observed in the spectra. To summarize, the measured emission spectra are consistent with the calculated emission from the exciton, bi-exciton, and charged exciton complexes.

5.1.5 Single quantum dot micro-photoluminescence

Sample 2128, was studied using the micro-PL setup described in chapter 3. Figure 5.14a displays state filling spectroscopy of the as-grown sample with an ~5μm diameter defocalized probe spot. The excitation intensity is kept low since this sample has very low QD density and the WL peak dominates the spectra quite rapidly at higher intensities (see figure 5.2). The lowest energy curve has broad features with apparent peaks at 1.619,

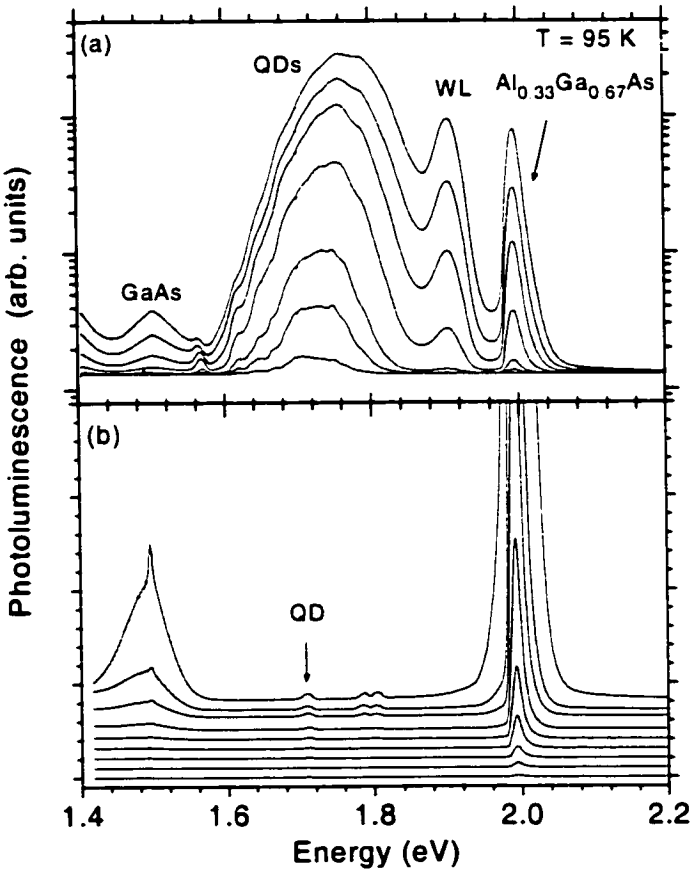

Figure 5.14 State filling PL of sample 2128. (a) As-grown for low excitation intensities, and (b) mesa A1 having 600 nm side length. The QD peaks are resolution limited in (b).

1.646, 1.669, 1.700, 1.729, and 1.749 eV. As the excitation intensity is increased, some of these features remain, such as the features at 1.619, 1.646 and 1.749 eV. Emission from the undoped MBE grown GaAs and from the *n*-doped bulk GaAs wafer is observed at 1.5 eV. As noted at the beginning of the chapter, the s-shell peak is at lower energies compared with sample 2134 and the WL is stronger. In figure 5.14b, the state filling PL of mesa A1, having 600 nm lateral dimensions is shown when probing with a 1-μm diameter probe spot, with a very low energy resolution. At the lowest excitation intensities, only one peak is visible at 1.711 eV in the QD energy range, at higher excitation intensities, two additional peaks appear at 1.787 and 1.803 eV. Note the relatively weak intensity from the QD with respect to bulk AlGaAs and GaAs, indicating that the 1-μm spot excites the area surrounding the mesa as well.

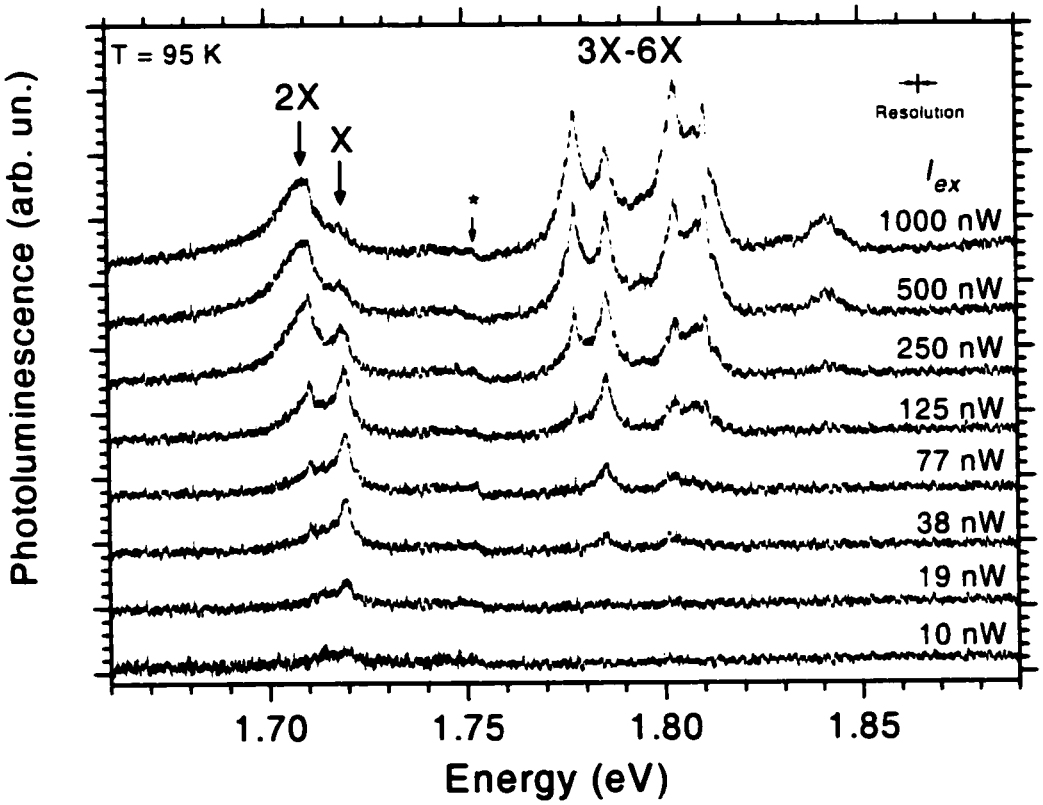

Figure 5.15 State filling PL of mesa A1 of sample 2128. The * denotes an artifact arising from slight misalignement of joined detector energy windows.

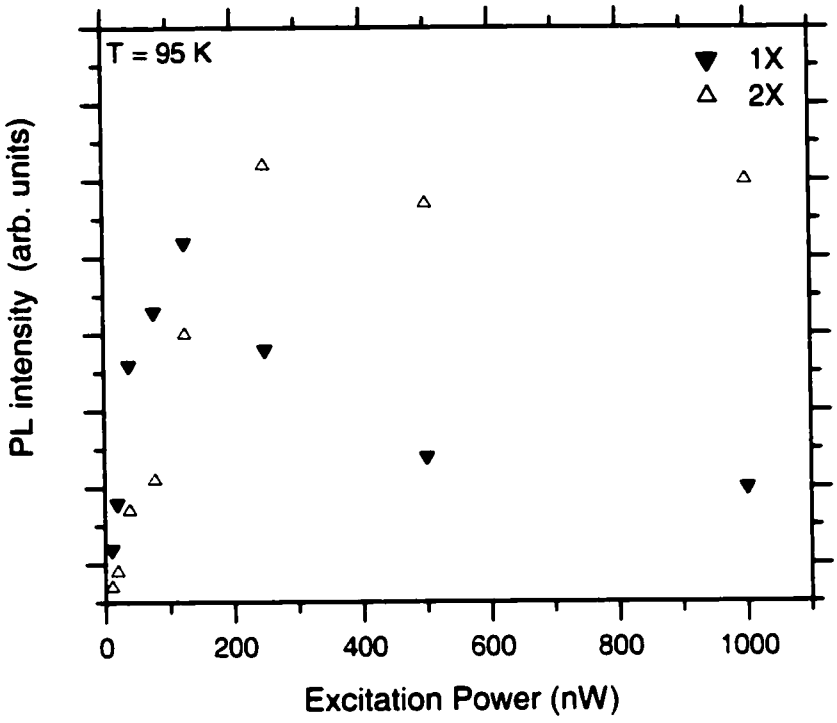

Figure 5.16 PL intensity for both the exciton (1X) and biexciton (2X) as a function of excitation power for mesa A1 of sample 2128.

The region of interest with improved resolution is shown in figure 5.15. Because the measurements are done at 95 K, the linewidth of the peaks broaden from 0.9 meV to 4-5 meV.[166,167] Such a behavior is characteristic for temperatures where thermionic emission is important.[28] At the lowest excitation intensity, one peak is present at 1.719 meV. As the excitation intensity is increased, a second peak is observed 6 meV lower energy at 1.712 eV. This second peak dominates over the first one above 250 nW excitation intensity. As well, additional peaks appear above 38 nW at ~70 meV higher energy with peaks at 1.786 and 1.803 eV. At higher excitation intensity, additional peaks occur at 1.778, 1.811, and 1.841 eV. The spectra is very similar to the one observed for sample 2134: at very low excitation intensity, emission from the exciton is observed, followed by

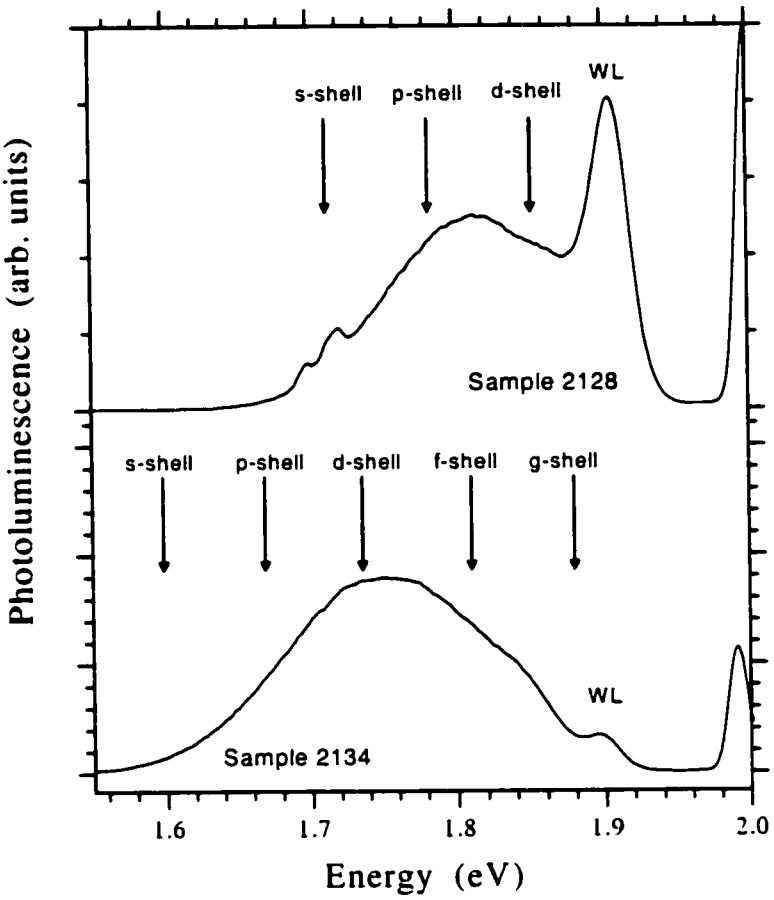

Figure 5.17 PL of samples 2128 and 2134 with excitation intensity of a few kW/cm^2 at T = 77 K. The arrows indicate the energy level positions for both samples with intersublevel spacings of 70 meV.

emission from the biexciton, having a biexciton binging energy of 6 meV. The power dependence of the exciton and biexciton emission is shown in figure 5.16. The exciton peak increases linearly in the power range from 10 to 100 nW. With stronger excitation, the intensity saturates and than starts decreasing. The biexciton gains intensity up to the maximum intensity measured but starts to indicate some saturation above 200 nW excitation. For the higher excitation intensities, the second shell starts being filled, this leads to additional peaks in the lowest s-shell. As well the p-shell has many lines, since we detect more than one configuration between 3X and 6X and that for some level

fillings, more than one configuration is allowed. In this case, the p-shell can be filled to a much higher degree than for sample 2134 due to the reduced excitation spot size (20 times smaller). Again, we obtain an intersublevel spacing of ~70 meV, but in this case a maximum of three confined shells is possible.

Figure 5.17 displays the second highest excitation curves of figure 5.2 for sample 2128 and the highest excitation curve for sample 2134 with arrows indicating the possible positions of all the QD-confined energy levels. Both samples have intersublevel spacings of ~70 meV, but sample 2128 has up to three confined shells while sample 2134 has up to five confined shells. As shown in figure 5.2, for these growth conditions, samples with a greater amount of strained material deposited have their ground state position red-shifted while the WL peak does not move. This allows for a larger number of confined states for sample 2134.

5.2 InAs/GaAs quantum dots

A short section is used to discuss emission from single InAs/GaAs in preparation for the next chapter treating on coupled pairs of InAs/GaAs QDs. Figure 5.18 displays the structure of sample 2072. The growth was carried out on a semi-insulating (100) GaAs substrate. After oxide desorption, a GaAs undoped buffer layer of 800 nm was grown starting at 640°C, with the last 12 nm grown at 620°C. 1.9 ML of strained InAs was deposited at 520°C, followed by 5.0 nm of GaAs. The temperature was then ramped up to 620°C for 100 s to allow for indium evaporation followed by 30 nm of GaAs deposition

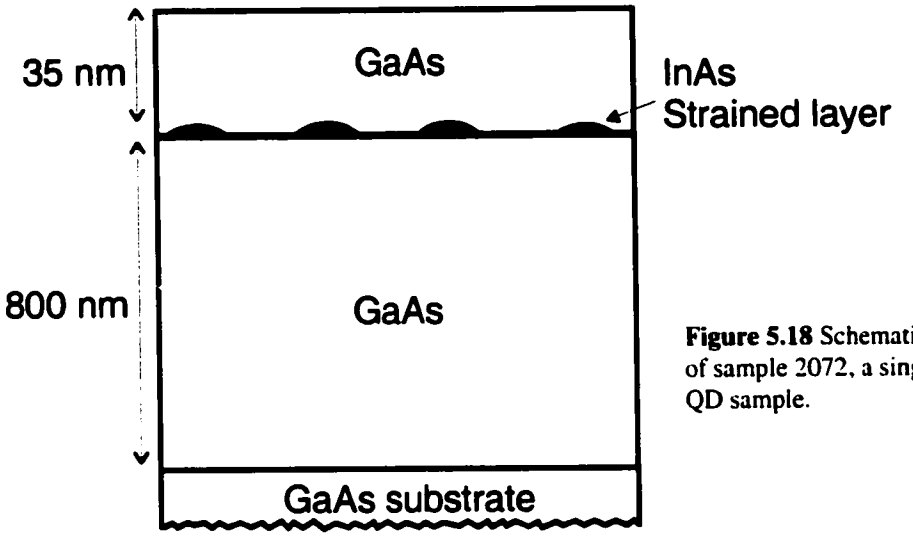

Figure 5.18 Schematic cross-sectional view of sample 2072, a single layer InAs/AlGaAs QD sample.

at 640°C.

Figure 5.19 shows PL results for this sample. The top curve is for the as-grown sample with the s-shell peak located at 1.135 eV. The spectrum reveals five confined shells located 60 meV one from another. The sample was annealed at 850° for 30 s. so that all the QD peaks could be detected using a CCD detector which has a limit of ~1050 nm in the infrared. This anneal causes pronounced interdiffusion of the In and Ga atoms in the growth direction and results in a pronounced blue-shift of the energy levels as well as a reduction of the intersublevel spacing and the inhomogeneous broadening of the QD ensemble.[168] The annealed sample has the first confined shell at 1.26 eV (984 nm) well within the CCD detection range. The annealed sample also shows five confined shells with intersublevel spacings of 40 meV.

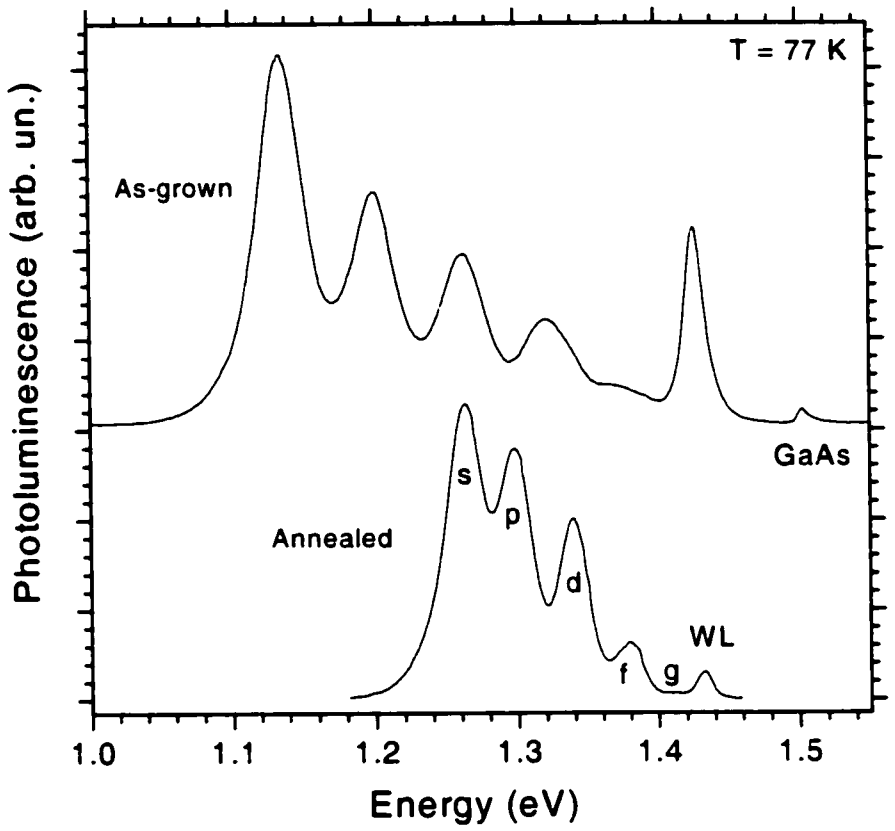

Figure 5.19 Ensemble PL of sample 2072 with excitation intensity of a few kW/cm^2 at T = 77 K. The top curve displays the as-grown sample, while the bottom curve is for the sample annealed at 850°C for 30 s.

Emission from two single QDs originating from two mesas having ~200 nm diameters are shown in figure 5.20. At low excitation intensities, the exciton line (X) dominates the spectra for both QDs, as the excitation intensity is increased, many lines appear below the exciton line and cover a wide energy range (~20 meV). For mesa K6, the peak assigned as the biexciton (2X) line is located 2.8 meV below the exciton line. At higher pump powers, the p-shell is seen, and for QD from mesa J10, emission from the d-shell is also observed. The peaks are located ~40 meV one from another as observed in the ensemble PL. The state filling is similar to the observations of single AlInAs/AlGaAs single QDs. The large amount of lines has been previously observed by other groups[42,169]

and is in great part due to the non-resonant optical excitation. By using a laser line with an energy high above the barrier, the relaxation of the carriers into the QD levels involves multiple phonon emission, so the carriers in the system are in strong non-equilibrium. In order to minimize these additional lines, resonant excitation can be used,[44] or low-intensity excitation at higher temperatures. The chosen temperature must allow for thermal population of higher states but must not be so high that thermionic effects become important for that system.

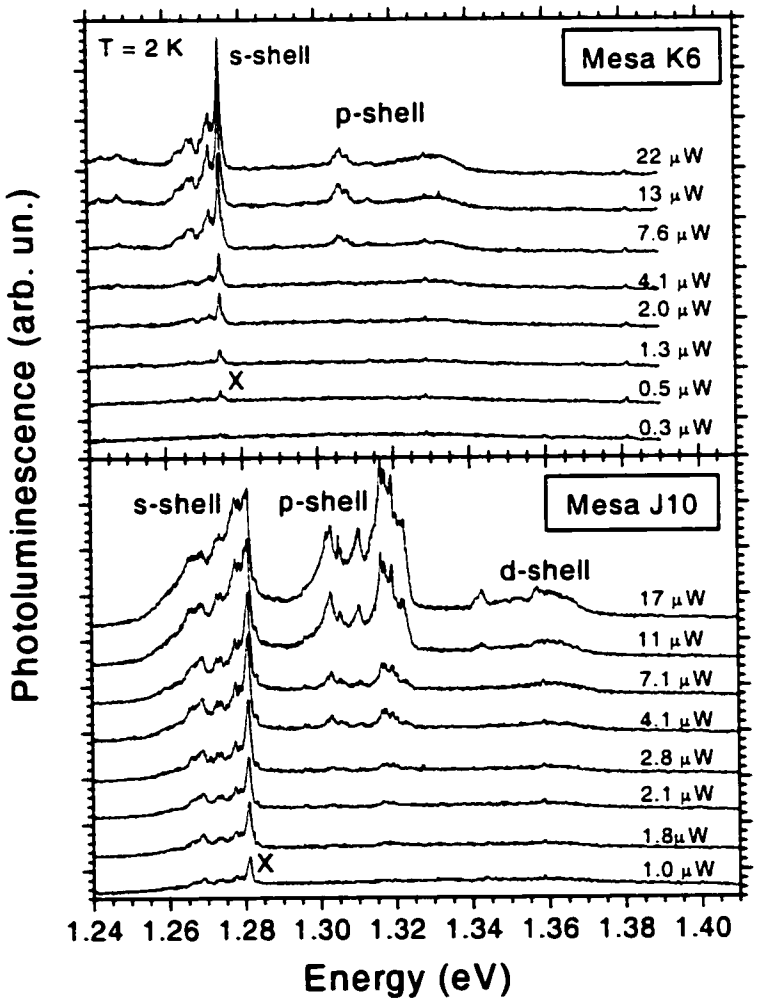

Figure 5.20 PL spectra from mesas K6 and J10 of sample 2072 as a function of excitation intensity.

5.3 Concluding remarks

We investigated single self-assembled InAlAs/AlGaAs QDs by PL spectroscopy. The single QD are isolated by lithography of as-grown material, in which mesa structures with lateral sizes down to 100 nm are fabricated. We demonstrated the existence of quantized energy levels in these ternary QDs. By varying the excitation power, we measured the recombination spectrum of neutral and charged excitons populating ground and excited state of a QD. We deduced an intersublevel electron and hole energy spacing of ~70 meV, which points to the existence of up to five confined shells in these QDs. The binding energy of a biexciton and charged exciton was found to be ~5 meV. This value is 2 meV larger than the value of 2.7 meV[43] and 3.1 meV[41] found for $In_xGa_{1-x}As/GaAs$ QDs. In magnetic field, we observed a similar Zeeman splitting of the exciton and the bi-exciton transitions confirming the spin degeneracy of the lowest energy level. Low excitation intensity spectroscopy of single InAs/GaAs QDs reveals a strong exciton peak with many additional lines located between 3 and 20 meV lower energy associated with multi-carrier effects.

Chapter 6

Spectroscopy of single pairs of coupled InAs/GaAs quantum dots

In this chapter, we present results on the effects of energy level coupling of adjacent QDs. In order to systematically study this effect, the coupling strength between the zero-dimensional states is varied by changing the distance between 2 layers of stacked self-assembled InAs/GaAs QDs. This binary system was used since sharp electronic shells can be obtained for stacked systems as explained in chapter 2. The chapter starts with a description of the samples and explanation of the drastic indium-flush used during the QD growth to bring the two layers close enough for energy level coupling to be observed in the spectroscopic measurements. This changed the shape of the QDs from a lens-shape to a disk-shape. This is followed by luminescence results of coupled QD ensemble and presentation of different models to explain the observations. Two models from the literature are summarized, one treating the QDs as two thin-coupled QWs, another using the adiabatic approach briefly described in chapter 2 and the effective mass approximation. Presentation of spectroscopy of single pairs of QDs reveal wave function coupling and energy splitting larger than 30 meV of the symmetric and anti-symmetric states of the lowest confined shell for the closest pairs. The results compare favorably with the theory. The end of the chapter relates the observed peaks to coherent tunneling of

electrons and holes between the two QDs which, leads to entangled states of electron-hole pairs. This is a first step in possibly using QDs for quantum information processing.[170,171,172,173,174,175,176]

6.1 Sample growth and structural characterization

Figure 6.1 displays the structure of the coupled layer samples. The growths were

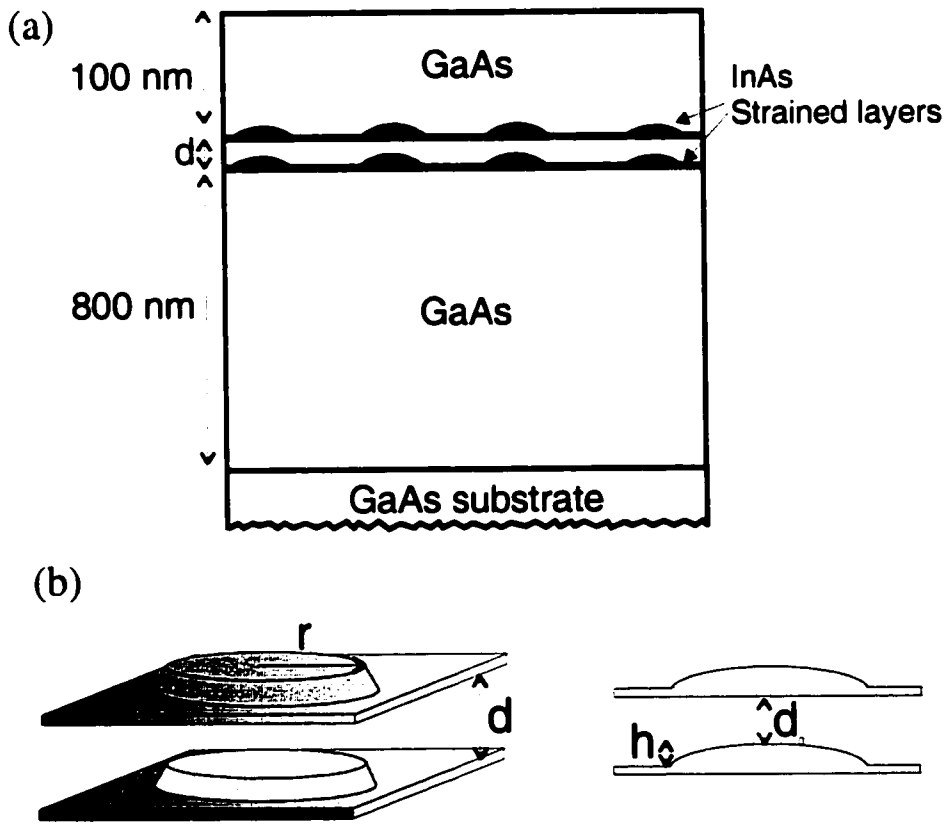

Figure 6.1 (a) Schematic cross-sectional view of the coupled QD samples, the double layer InAs/GaAs QD sample. The spacer thickness *d* varies from sample to sample. (b) Schematic picture of a pair of coupled QDs.

carried out on semi-insulating (100) GaAs substrates. After oxide desorption, a GaAs buffer layer of 800 nm was grown starting at 640°C, with the last 12 nm grown at 620°C. 1.9 ML of strained InAs was deposited at 520°C with a 60 s anneal time, followed by 3.0 nm of GaAs. The temperature was then ramped up to 620°C for 100 s to allow for Indium evaporation followed by a GaAs spacer layer, which had a thickness of 1.0 to 12 nm depending on the sample. A second layer of QD is deposited using the same procedure as the first. This is capped with 100 nm of GaAs.

Table 6.1 lists the different samples studied. The spacer thickness *d* increases by 1 nm for each sample between samples 2191 to 2195. Sample 2190 is a single layer reference sample. Some sample parts where etched to only leave small mesas as described in chapter 3.

Sample	Spacer thickness d (nm)
2190 single layer (reference)	----------
2191	4.0
2192	5.0
2193	6.0
2194	7.0
2195	8.0
2196	15.0

Table 6.1 InAs/GaAs coupled QD samples.

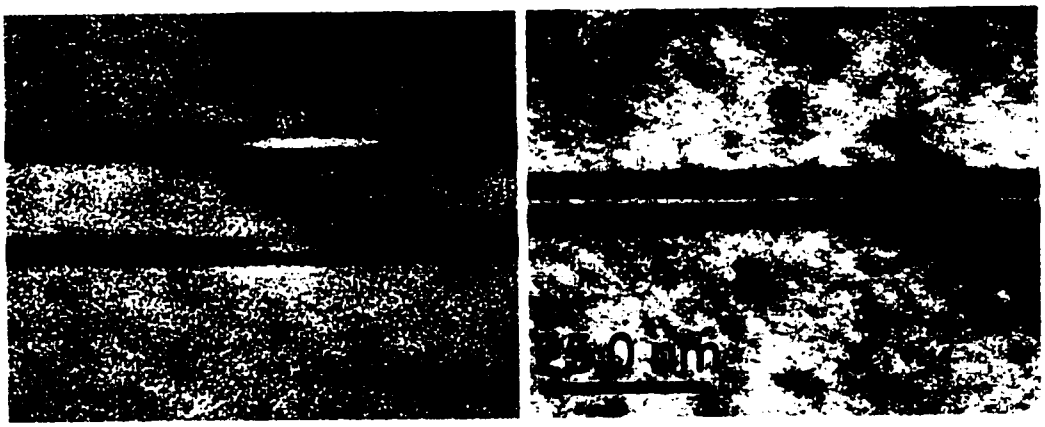

Figure 6.2 Cross-sectional (200) dark field TEM of the double-QDs indium flushed at 3.0 nm. A pair of QDs is shown for a nominal spacer thickness of a) d = 15.0 nm (sample 2196), and b) 4.0 nm (sample 2191). TEMs by J. P. McCaffrey, NRC.

In figure 6.2, TEMs of sample 2196 and 2191 show that the QDs take the shape of thin disks due to the strong Indium-flush done on them. The typical QD height h is estimated to be between 1 and 2 nm and the typical radius r varies from 8 to 12 nm. The QD density is estimated at ~30-40 QDs/μm^2 based on plan-view TEM of QD samples with similar growth conditions[36] except for a different Indium-flush.[177]

6.2 Ensemble photoluminescence

State-filling spectroscopy is shown in figure 6.3 for spacer thicknesses between d = 15 nm and d = 4 nm. For the sample with d = 15 nm, sample 2196, the intersublevel spacing is ~43 meV. Simple wavefunction calculations show that at this thickness, the confined states should have very little coupling. Figure 6.3 shows that the coupling

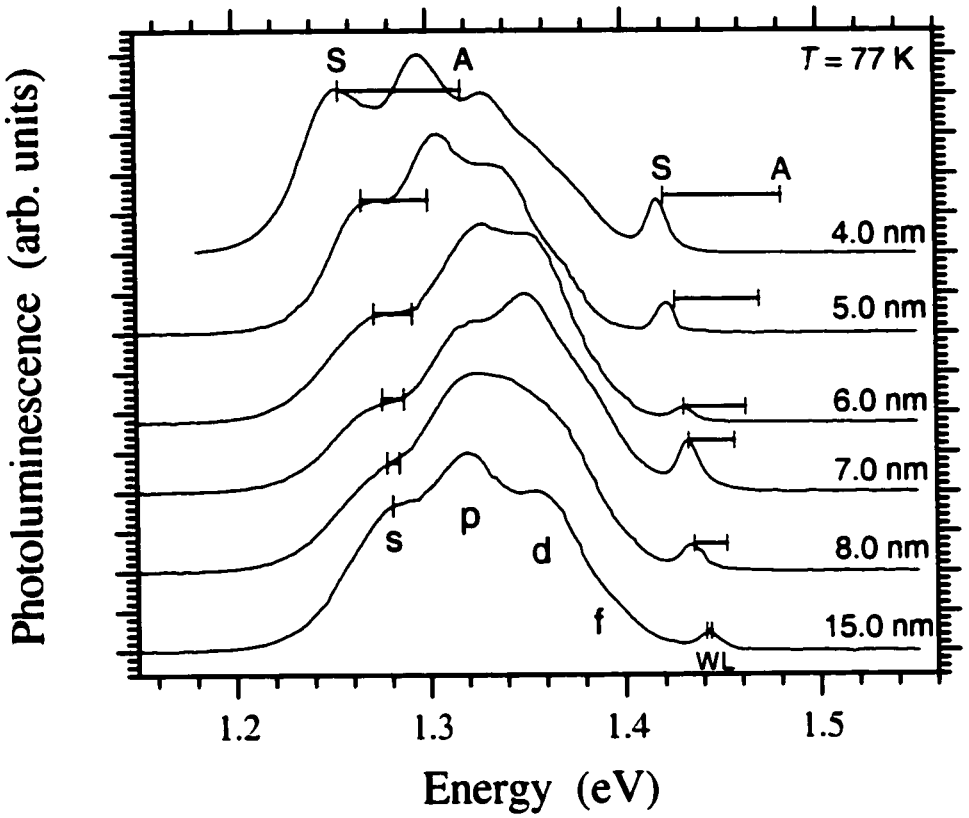

Figure 6.3 Coupling for thin disk-like double QDs (indium-flushed at 3.0 nm) for spacer thicknesses d between 15 nm and 4.0 nm. The solid lines are calculations of the energy level splitting of the symmetric (S) and anti-symmetric (A) states for the WL and the QD s-shell state from figure 6.4a. The spectra are excited with a few kW/cm^2. See also ref. [50].

between the zero-dimensional states leads to an apparent redshift of all of the shells. The shift is particularly strong for spacer thicknesses d <6 nm. The total redshift of the s-shell is ~23 meV between d = 15 nm and d = 4 nm. There is also a remarkable shift of the WL by 26 meV between d = 15 nm and d = 4 nm.

6.2.1 Modeling

The behavior of the WL is properly understood with a simple model calculating the energy splitting for the electrons in two thin InAs QWs separated with a GaAs

barrier.[50] Models of symmetric double QWs are now standard and can be easily found in the literature.[1,178] When the QWs are separated by a large distance, the interaction between the eigenstates localised within each well is very small and the wells behave as two independent single QWs. However, as the central barrier is decreased, the energy levels interact, with one being forced to higher energies and the other to lower energies. The wave function of the lower state is the sum of the wave functions of the separate QWs, and the higher state is a difference in wave functions, i.e.

$$\Psi_{symmetric} = \frac{1}{\sqrt{2}}(\psi_1 + \psi_2); \tag{6-1}$$

$$\Psi_{anti-symmetric} = \frac{1}{\sqrt{2}}(\psi_1 - \psi_2). \tag{6-2}$$

Where ψ_1 and ψ_2 are the lowest level uncoupled wave functions of QW 1 and QW 2.

Fafard et al. did the same modeling to verify the coupling between the QDs. For example, figure 6.4a reproduces the results of such calculations using a well width of 0.54 nm, corresponding to the nominal growth thickness used for the InAs layers. Because of the finite potential and because the wells are extremely narrow, the wave function extinction in the barrier is weaker for such upper states. The wave function coupling and the energy splitting into a symmetric and anti-symmetric state is therefore observed for a relatively thick barrier (splitting close to 10 meV for a spacer d = 6 nm). For the same reason, the WL electron probability for the symmetric state is high in the region between the two WLs, which corresponds to the bottom QD region. As observed in figure 6.3, the redshift of the WL compares well with the measured experimental values. The experimental data is also represented in figure 6.4a, where the diamonds

indicate the WL peak position relative to the GaAs barrier energy, and where an additional fixed offset (here ~11 meV) is included to take into account the hole contribution. The hole contribution is expected to be smaller because of their larger effective masses. The higher energy anti-symmetric state of the WL is not observed in the emission spectra since the WL is a two-dimensional system where filling of the second level can only be done at excitation intensities that can damage the sample. The calculated anti-symmetric and symmetric states arising from the wave function coupling of the s-states between the two QDs and the lowest level of the WL are denoted "A" and "S" in figure 6.3.

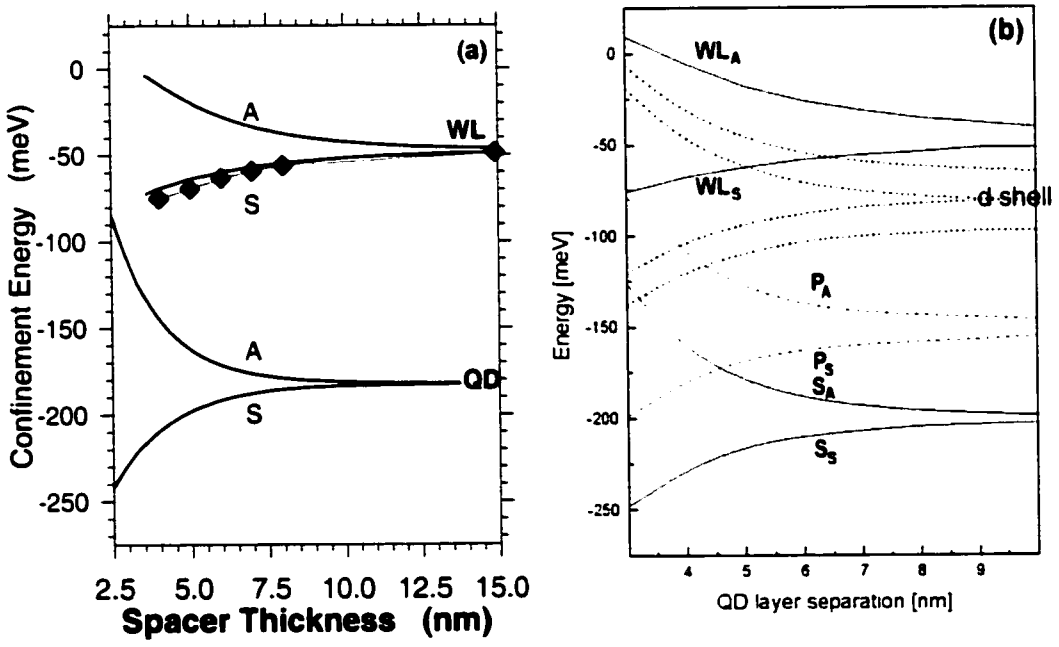

Figure 6.4 Energy level splitting of the symmetric (S) and anti-symmetric (A) states for the WL and the QD states. (a): The solid lines are calculations obtained for electrons in a coupled InAs/GaAs double-wells 0.54 nm wide (WL), and 1.25 nm wide (QD). From ref. [50]. The diamonds are the data points for the shift of the WL peak positions from figure 6.3. (b): Calculated electronic energy levels as a function of quantum dot distance *d*. The calculations are done in the effective mass and adiabatic approximations. From ref. [179]. The GaAs barrier is set as a reference.

A similar model can be used to obtain more information about the QD coupling. To simulate the QDs, in a simple first approximation, Fafard et al.[50] used two InAs QWs having a width corresponding to the QD thickness. The QD line in figure 6.4a gives the results for a width of 1.25 nm as a function of the spacer thickness. The width calculated has the WL height plus the QD height h. This width is chosen because it gives a QD ground state position, which is close to what can be deduced for the QD thickness from the TEM images of figure 6.2. As well, the spacer thickness d is related to the actual barrier thickness d_0 for the QD by $d_0 = d - h$. Also the effective QD width is the sum of the WL thickness plus h, and so using the QD width and a WL thickness of 0.54 nm gives h = 0.71 nm for the QDs indium flushed at 3.0 nm. From this simple model, the QD coupling can only be observed for h<6.0 nm when probing a QD ensemble, since the inhomogeneously broadened linewidth will mask the effect of smaller splitting. For the thinnest spacer used d = 4.0 nm, a splitting of ~60 meV is calculated between the symmetric and anti-symmetric s-state. The 25 meV redshift calculated for the QD symmetric electron state was close to the value of ~23 meV found experimentally for the s-shell.

Figure 6.4b shows results of calculations of the electron energy levels of coupled disks as a function of the distance between the QD layers d using the effective mass and adiabatic approximations.[179] This model was developed by M. Korkusinski and P. Hawrylak and is explained in ref. 180. The adiabatic approximation separates the motion in the growth direction and the motion in the lateral direction relying on the disparity of vertical and lateral dimensions of the QD, and on an assumption that the wave function

describing the vertical motion changes slowly along the disk radius. The lower disk has a diameter of 16 nm and the upper disk one of 17 nm, the disks are 1.54 nm high, the WL thickness is 0.54 nm, the confining potential is 800 meV, and the effective electron mass $m^* = 0.043$. For $d > 6$ nm, there are three confined shells, s, p, and d in each QD. The d shell is split into two degenerate states with angular momentum $m = \pm 2$ and one state with angular momentum $m = 0$. When the disks are far apart for each angular momentum, the symmetric and anti-symmetric levels are close to each other. As in the previous model based on calculations on thin QWs, the shells are seen to split into symmetric and anti-symmetric states as the two QD layers are brought closer together. This splitting increases with energy, because the higher the energy the lower the tunneling barrier and the bigger the overlap of wave functions due to their shallower confinement. In the region $d = 4$-5 nm crossing of levels with different symmetry is observed and different angular momenta.

6.2.2 Large mesas

Figure 6.5 shows PL spectra of ensembles of QDs recorded for various excitation powers. The left panel shows spectra of a sample containing only a single sheet of QDs. At low excitation only emission from the s-shell is observed. With increasing excitation the emission from this shell saturates due to complete shell filling and simultaneously emission from the higher p-shell is observed. The spectral features are almost equidistantly spaced with an energy splitting between two adjacent emission lines of about 50 meV.

The other panels in figure 6.5 show PL spectra of ensembles of coupled QDs for

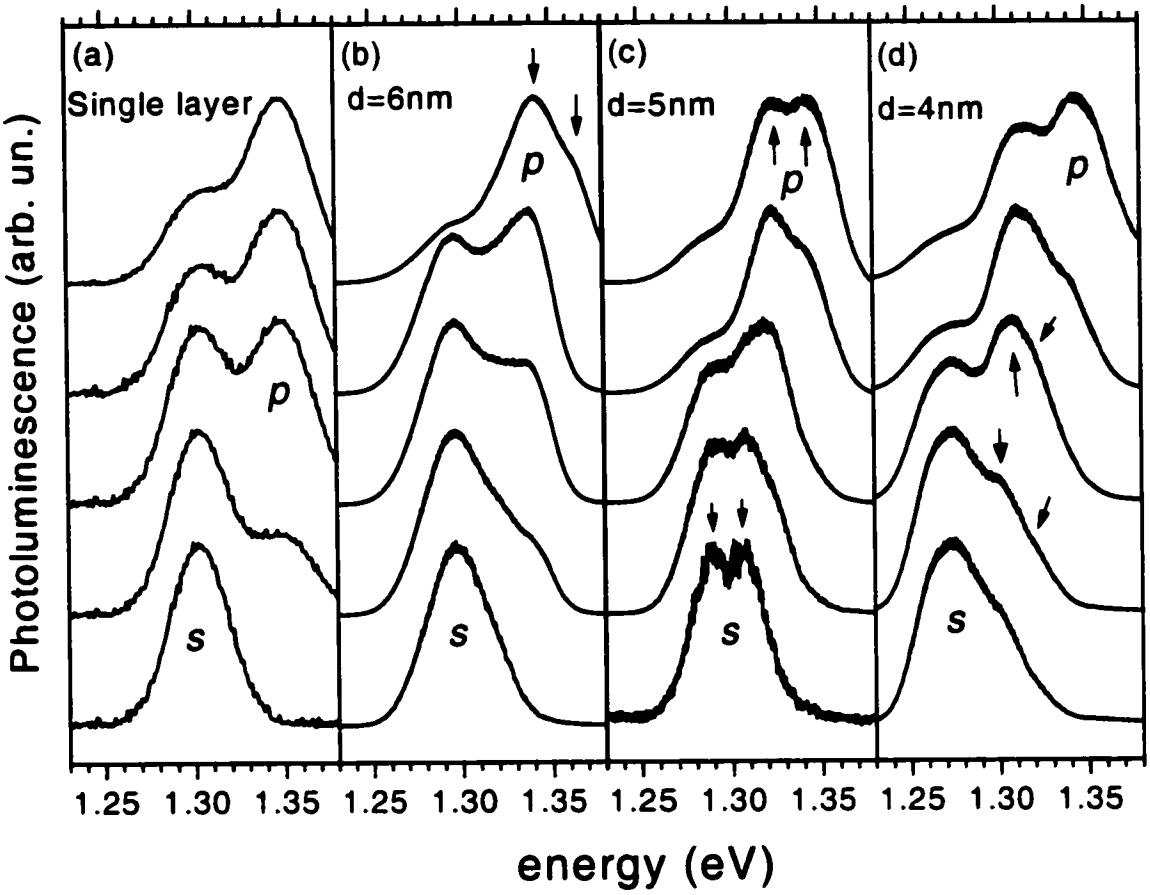

Figure 6.5 PL spectra of ensembles of QDs, at T = 4 K, as a function of the excitation intensity for (a) a single layer, sample 2190, (b) a double layer with spacing d = 6 nm , sample 2193, (c) a double layer with spacing d = 5 nm , sample 2192, (d) a double layer with d = 4 nm, sample 2191. Courtesy of M. Bayer.

varying separation between the two layers. For the sample with a 6 nm wide barrier, the evolution of the spectra at low excitation powers is very similar to that for the sample containing a single dot sheet. One notes that the halfwidth of the emission from the s-shell is now 8 meV larger. The splitting between the p- and the s-shells is about 50 meV as observed for the single QDs. At high excitation, however, one finds clear indications of a splitting of the p-shell emission by about 20 meV.

The appearance of the spectra changes drastically when the barrier width is reduced to 5 nm. In this case the s-shell develops two emission lines with an energy separation of 20 meV. Upon increasing excitation power, emission from the p-shell

begins to dominate, which shows also clear signs of a doublet structure with a splitting of almost 30 meV.

The right panel in figure 6.5 finally shows the PL of a coupled QD array with 4 nm barrier thickness. At the lowest excitation, only emission from the lowest s-shell state is observed. At elevated excitation (in particular in the second trace from the bottom) signs for two closely lying emission lines are observed around 1.31 eV. The splitting is estimated at 10 meV. On the high energy side a further spectral line appears at the highest excitation used in the experiments. From comparison of the several panels one notes, that with decreasing barrier width the symmetric peak of the s-shell shifts continuously to lower energies as observed in the large ensemble PL spectra of the previous section.

6.3 Single pair photoluminescence

While these PL studies of QD arrays give clear indication of a splitting of the QD induced by the coupling between two dots, a clear resolution of this splitting requires optical spectroscopy on single coupled QDs. These spectra were recorded at low excitation powers to avoid emission from multi-exciton complexes. The temperature was T ~60 K so that not only ground state exciton emission, but also emission from excited exciton states is observed due to thermal population. In each case, symmetric single QD molecules were selected whose ground state emission is located at the center of the emission band of the corresponding arrays. The same lithographic and spectroscopic techniques as in chapter 5 were employed to isolate a single coupled QD.

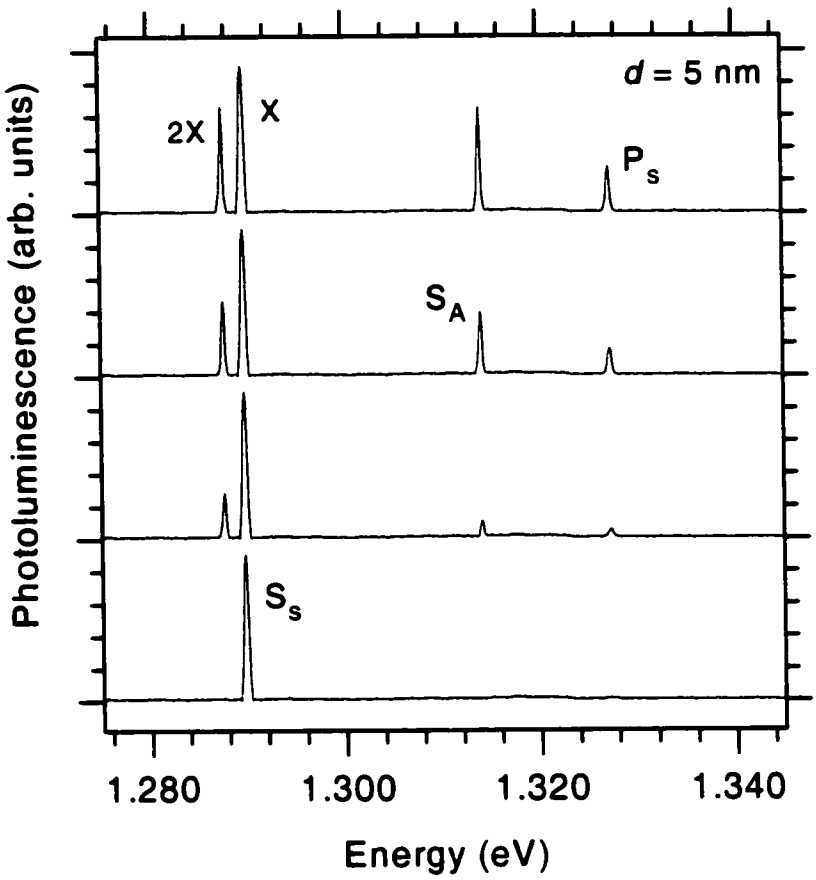

Figure 6.6 Emission spectra of a single coupled QD with $d = 5$ nm (sample 2192) as a function of the excitation power. Bottom curve is the lowest excitation intensity. From ref. [179].

Figure 6.6 shows the PL of a single coupled QD for various excitation powers increasing from bottom to the top. The barrier thickness between the QDs was 5 nm. At the lowest excitation only emission due to the recombination of an exciton X in its ground state denoted S_S is observed. With increasing excitation, we observe the formation of biexciton 2X, simultaneously emissions from excited states S_A and P_S are observed.

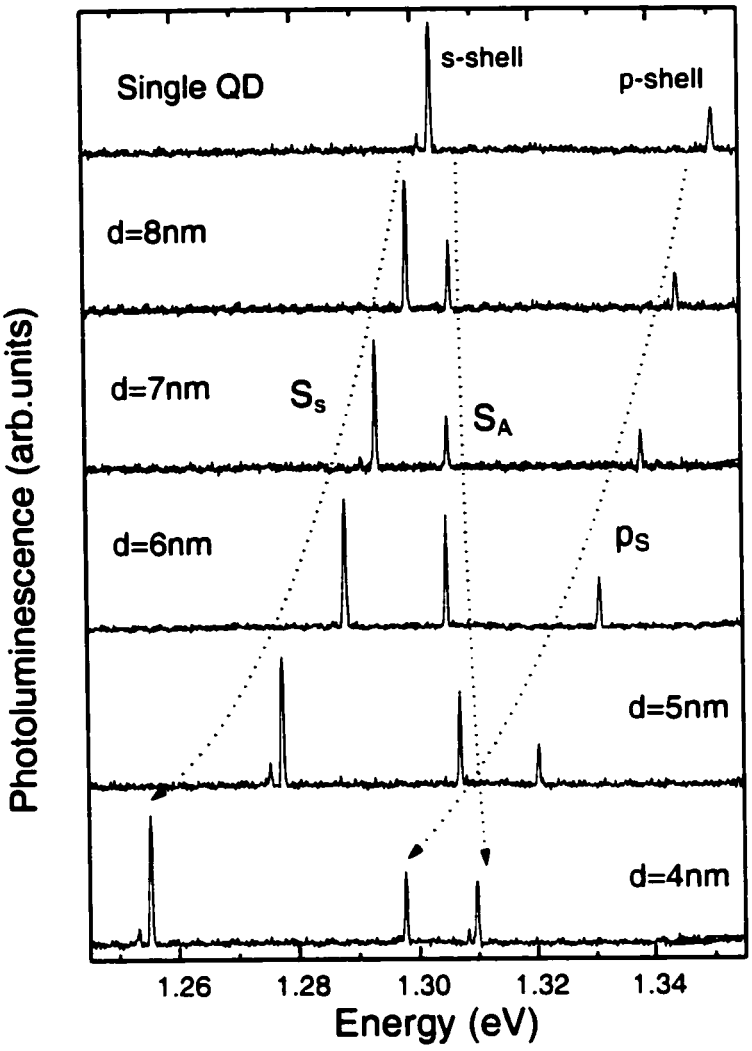

Figure 6.7 Emission spectra of single coupled QDs at T ~60 K for varying dot layer separation *d* from 8 down to 4 nm. As reference, also a single QD was studied (top trace). From ref. [183].

The dependence of the energies of the QD molecule states on the barrier width which separates the two coupled dot layers can be seen in figure 6.7. It shows excitation spectra of different coupled dot samples in comparison to the spectrum of a single QD; excitation intensities are equivalent to the top spectra shown in figure 6.6. For the single dot (top trace) excitonic as well as very faint biexcitonic emission from its s-shell is registered at 1.30 eV, and a peak originating from the p-shell is observed at 1.35 eV. For

the QD separation d = 8 nm, the peak located at 1.30 eV splits and we ascribe these peak to emission of the symmetric (S_S) and anti-symmetric (S_A) peaks of the s-shell. The energy splitting between them is about 10 meV. In addition, a further emission line P_S appears on the high energy side and is assigned to the symmetric state of the p-shell. The energy of all these features depend systematically on d: reduction of the QD separation moves the emission line S_S strongly to lower energies, while the energy of the peak S_A is almost constant leading to an increase of their splitting to more than 25 meV. This behavior is suggestive of the energy level splitting due to the QD coupling. It should be noted that some QD pairs showed a more symmetric splitting than the QD pair shown in figure 6.7. The asymmetry could be caused by a slight lateral misalignment of the two QDs.

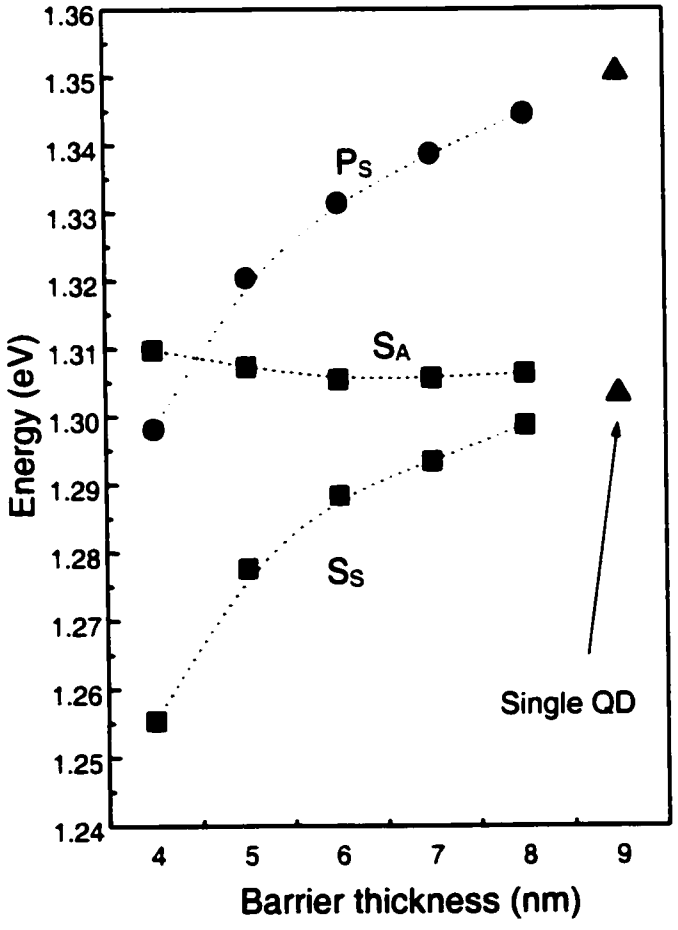

Figure 6.8 Evolution of the energies of emission lines as a function of distance between QD layers. Circle and squares denote experimental data, with dotted lines as guides to the eye. From ref. [183].

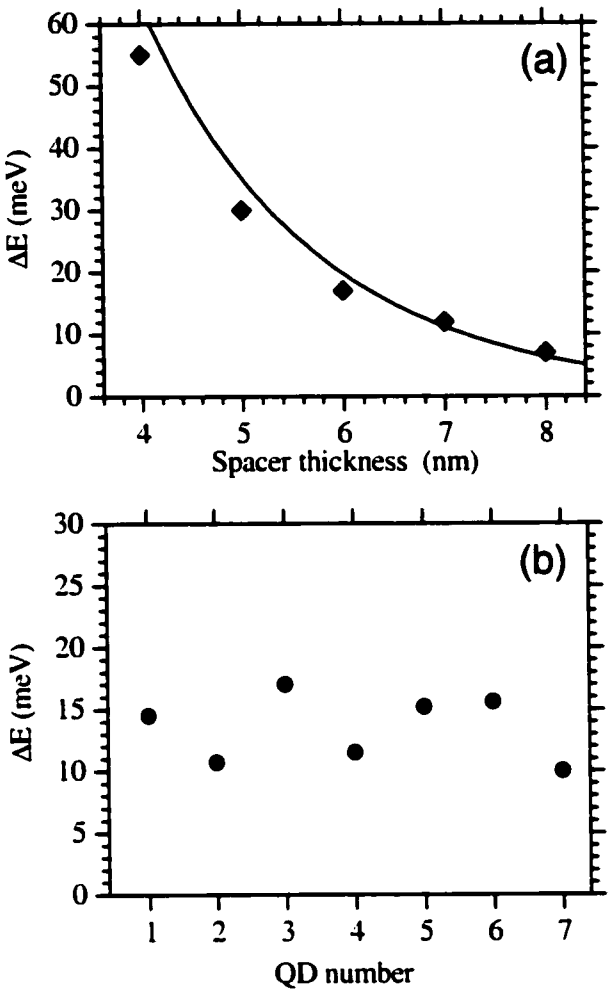

Figure 6.9 (a) Evolution in the energy splitting between the *s*-shells symmetric and anti-symmetric states as a function of the spacer thickness *d*. The solid line is from the calculation shown in figure 6.3. (b) Statistics on the energy difference between symmetric and anti-symmetric *s*-shell states for six different single coupled QDs having $d = 6$ nm spacing widths.

The dependence of the observed transition energies as a function of the distance *d* is summarized in figure 6.8. The trends in energy levels are suggestive of a crossing of the anti-symmetric s-shell emission and the symmetric p-shell emission at $d = 4$-5 nm so that the vertical misalignement of the QDs, if any, is small.[180] The observed behavior is in qualitative agreement with that expected from the model calculations of figure 6.4.

The splitting energy ΔE measured between the symmetric and anti-symmetric s-shell (S_S and S_A) for the different samples of figure 6.7 are shown in figure 6.9a. We see that they correspond well to the calculated splitting, ranging from a splitting of ~8 meV for *d*

= 8 nm up to ~55 meV for d = 4 nm. Statistics on the splitting between the symmetric and anti-symmetric states of single QD pairs with spacer thickness d = 6 nm are shown in figure 6.9b. This data indicates that the points of figure 6.9a have uncertainties of ± 4 meV.

6.4 Coherent tunneling of electrons and holes and the formation of entangled states

In light of the results of the past section, we can look at the possibility of using two coupled QDs as a quantum gate, the key building block of a quantum processor. Recently, Hawrylak, Fafard and Wasilewski in ref. 181 proposed to use a pair of vertically aligned semiconductor QDs as the optically driven solid state quantum gate, in which an electric field applied along the growth direction can localize individual carriers on the upper QD (index zero) or the lower QD (index one). The two different QD indices play the same role as the two states of a "spin" (a qubit) and are referred to as "isospin".[58] When the electric field is turned off, the quantum mechanical tunneling rotates the "isospin" leading to the superposition of two QD states. The quantum gate is built when two different particles, an electron and a hole are created optically. In the presence of the electric field, the particles are localized on opposite QDs. After switching off the electric field, the tunneling and interaction between the two particles should lead to the formation of entangled states, i.e. the two particles are brought together and are allowed to interact.[182] The states can be disentangled later by preventing tunneling through the

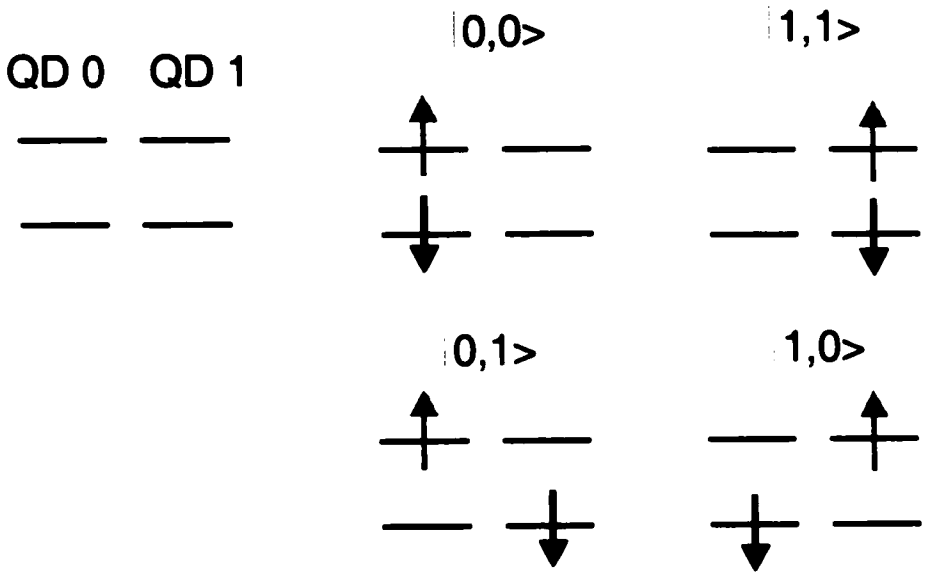

Figure 6.10 Scheme of the electron-hole pair configurations. In each panel, the left side corresponds to QD 0, and the right side to QD 1. The light arrows correspond to the electron, the dark ones to the hole. From Bayer et al. [183].

application of an electric field.

This proposition can be directly related with the results presented in the previous section. We start with the model proposed in section 6.2 using weak tunneling and strong lateral quantization, and assume that an electron tunnels from QD0 to QD1 with a tunneling probability $\langle 0|H|1\rangle = t$ without changing angular momentum, and H is the Hamiltonian of the system. The Hamiltonian in this basis is diagonal, with $2t$ being the splitting between the $\Psi_{\text{symmetric}}$ and $\Psi_{\text{anti-symmetric}}$ levels.

In the spectroscopic experiments, it is the recombination of electron-hole complexes that are measured, so Coulomb correlations also need to be included. Below is a simple model of an exciton in a pair of QDs in the weak tunneling limit taken from ref. 183. In figure 6.10, we show the four isospin states of a single electron hole pair: |0,0>, |1,1>, |0,1> and |1,0>. The first two states correspond to an electron and a hole on QD 0

or QD 1 and these can be created optically. The second pair corresponds to indirect electron-hole pairs e.g. electron on QD 0 and hole on QD 1 and can only be created optically when there is a (small) overlap of the states on the two dots. The interband polarization operator P^+ describing the creation of an electron-hole pair can be written as

$$P^+ |V\rangle = M_{00}\left[|0,0\rangle + |1,1\rangle\right] + M_{01}\left[|0,1\rangle + |1,0\rangle\right] \tag{6-3}$$

where the $M_{ij} = \langle i | j \rangle$ are the overlap integrals of the electron and hole wave functions on QDs i and j. The electron-hole pair states can therefore be written in a new basis of entangled states |a>, |b>, |c> and |d> consistent with the interband polarization operator:

$$\begin{bmatrix} |a\rangle \\ |b\rangle \\ |c\rangle \\ |d\rangle \end{bmatrix} = \frac{1}{\sqrt{2}} \begin{bmatrix} |0,0\rangle + |1,0\rangle \\ |0,1\rangle + |1,0\rangle \\ |0,1\rangle - |1,0\rangle \\ |0,0\rangle - |1,1\rangle \end{bmatrix} \tag{6-4}$$

For simplicity, similar tunneling matrix elements for electron and hole is assumed. Other factors that come into play are the terms for the electron-hole attraction for both particles being either on QD 0 or QD 1, the direct interaction for an electron in QD 0 and a hole on QD1, as well as matrix elements for electron-hole pair scattering from QD 0 to QD1 and scattering involving only one particle. The electron-hole pair Hamiltonian can be written in the new basis (a-d) with all these elements taken into account. This results in only the optically active states |a> and |b> remaining coupled via the tunneling matrix element *t*. The two lowest energy states that result from these calculations are linear combinations of the entangled states |a> and |b> and therefore are also entangled, they are referred to as eigenstates |a'> and |b'> of the exciton Hamiltonian. They are the excitonic

analogs of the symmetric and anti-symmetric single particle states, with the splitting controlled by tunneling and by Coulomb interactions. The two entangled states |c> and |d> are exact exciton eigenstates in this model but they are not coupled to the optically active states.

The results of the model show the evolution of the entangled states |a'> and |b'> of the two coupled isospins (electron-hole pair) as function of the QD separation.[183] When the QDs are brought closer, the optically active states lower their energies and increase the spacing in a manner similar to the symmetric S_S – anti-symmetric S_A splitting of the single particle energy levels. We can therefore conclude that the symmetric S_S and anti-symmetric S_A energy levels are entangled states |a'> and |b'>.

6.5 Concluding remarks

In conclusion, we studied double InAs/GaAs QD ensembles with well-resolved shells. Using spectroscopy on a single pair of coupled QDs, we are able to show energy level splittings larger than the thermal energy available at room temperature. The results are in qualitative agreement with the calculations of the energy levels of electrons in two coupled disks. It should be noted that a similar study done concurrently and independently has shown similar results.[184] It used a series of strain-induced QDs formed by locally straining a near surface double QW with InP self-assembled islands acting as the local stressors. The distance between the two QWs was varied and electronic coupling of the QD levels was observed. This demonstration opens possibilities of engineering

electronic and excitonic states at a molecular level and at room temperature for various quantum information processing applications.

Chapter 7

Conclusions and future work

The presence of a discrete energy spectrum distinguishes QDs from all other solid-state systems. That and the ability to manipulate their energy levels to tailor the number of confined states and their intersublevel energy spacing has caused them to be called "artificial atoms".[185] Results of single QD spectroscopy show that one of the most important consequences of strong carrier confinement in QDs is the prominent role of many-particle effects. The Coulomb interactions between carriers control carrier recombination dynamics as well as QD charging. As some of the results of this work shows the atom-QD analogy can not be carried too far. The carriers in GaAs-based self-assembled QDs, unlike electrons in an isolated atom, interact strongly with lattice vibrations and can be strongly influenced by defect, surface, or interface states.

State-filling spectroscopy of single $Al_{0.36}In_{0.64}As/Al_{0.33}Ga_{0.67}As$ QDs allowed us to measure the recombination spectrum of neutral and charged excitons populating the ground and first excited states of a QD. As well, magneto-PL measurements confirmed the spin degeneracy of the exciton and biexciton in this system. One way to increase the state filling to include all of the confined states of a QD, is to probe the QD with a smaller

diameter beam as discussed in section 5.1.5. To achieve this, the micro-PL scanning system is being upgraded with a 4.2 K variable temperature optical cryostat for microscopy. This type of cryostat offers a short working distance (a few mm), so that the microscope lens can be placed outside the cryostat to facilitate focussing. In addition, the cryostat is equipped with internal vibration isolation and a low thermal-expansion support structure to allow for low temperature mapping capabilities. The motorized translation stages are placed underneath the "flat" cryostat.

This setup could also allow the study of the effects of QD intermixing using single QD spectroscopy. The comparison of the emission from as-grown and intermixed samples could bring some information on the atom diffusion process during the thermal anneal and how the QD size and composition is affected.

An area that was not covered much but is of high interest, is the artificial ion. Occupancies with different numbers of electrons and holes result in charged exciton complexes. As the calculations presented in chapter 5 show the binding energies for charged QD excitons are on the order of a few meV. This allows for the controlled manipulation of energetically well-separated few-particle states under the action of an external gate electrode. The Coulomb blockade mechanism renders a discrete and stable number of extra charges in the QD. In future experiments and possible applications, the resonant optical absorption and emission of such systems is expected to be tunable between discrete and characteristic energies. Two recent papers demonstrate bias-controlled single-electron charging of a single QD.[186,187] This type of few-particle systems are expected to exhibit a variety of interesting spin configurations, which can be

controlled by an external magnetic field, gate-induced occupancy, and spin-selective optical excitation.

The results presented in chapter 6 on single coupled QDs show a strong dependence of exciton transitions in the QD molecules as a function of the distance between the two QDs. Magneto-PL experiments could bring additional understanding on the localisation and tunneling of electrons and holes in this structures as well as, experiments involving coupled QDs in p-i-n type-structures. The wavefunction coupling of the two QD energy levels and subsequent demonstration that some of the resultant levels can be called entangled states brings us to the next step towards the realization of a quantum gate. This is the demonstration that one can put contacts on a single pair of QDs and apply a vertical electric field to entangle/disentangle states.

Results of chapter 4 have shown that QD lasers can be tuned to lase in all of the QD confined energy levels. Widely tunable semiconductor lasers are essential components of high-capacity wavelength-division-multiplexed transmission and photonic switching systems.[188] QD lasers use the same growth and microfabrication technology of existing QW laser. External-cavity configurations employing a grating as a dispersive element have enabled tuning of QW lasers across 105 nm at λ = 800 nm,[189] and 240 nm at λ = 1500 nm,[190] for injection current densities of 21 and 33 kA/cm^2, respectively. This high bias is necessary to achieve lasing from the second quantised state of the QW and causes heating that somewhat restricts commercial applications of these sources with that wide of a tuning range. Stimulated emission from higher confined energy levels as been

reported for etched quantum wire lasers.[191] This type of laser is not used commercially since the fabrication techniques to obtain quantum wires are lengthy and multiple quantum wires are needed to achieve good gain properties. In contrast, QD emitters are well-suited for use as low-threshold, broadband tunable sources owing to two unique features of QD structures. First, the low QD DOS causes the QD ground state optical gain to saturate easily. This means that the higher-order energy levels are populated by carriers at fairly low current densities. Secondly, due to homogeneous and inhomogeneous broadening, continuous coverage of the wavelength spectrum is possible. The dot size variation, which is normally undesirable for low-threshold operation, can be exploited to extend the tuning range.

During the Stranski-Krastanow growth process on planar substrates, the QDs position themselves in a random manner on the surface. This renders single QD spectroscopy difficult since one does not know were each QD is exactly located and often when probing for single QDs, more then one will be detected if it happens that they are located very close one to the other at that position. As well, for QDs that are placed close one to the other, lateral wavefunction coupling can be strong. The control of the QD nucleation sites would remove these problems and would be advantageous for many device applications. For example, in laser applications, QD size control would result in a larger joint DOS at the lasing transition energy and a corresponding reduction in the threshold current density for lasing. Control of QD location would enable the production of integrated optoelectronic devices with varying functionality across the wafer and ultimately may be of interest in the production of photonic band gap structures based on

three dimensional arrays of band gap tailored QDs.[192]

References

[1] C. Weisbuch, and B. Vinter, *Quantum Semiconductor Structures: Fundamentals and Applications* (Academic Press, San Diego, 1991).

[2] R. V. Steele, "Review and forecast of laser markets: Part II," Laser Focus World, February, 84 (2001).

[3] Y. Arakawa, and H. Sakaki, "Multidimensional quantum well laser and temperature dependence of its threshold current," Appl. Phys. Lett. **40**, 939 (1982).

[4] Y. Arakawa, and A. Yariv, "Quantum well lasers – gain, spectra, dynamics," IEEE J. Quantum Electron. **QE-22**, 1887 (1986).

[5] H. Sakaki, "Quantum wires, quantum boxes and related structures: physics, device potentials and structural requirements," Surf. Science **267**, 623 (1992).

[6] M. Asada, Y. Miyamoto, and Y. Suematsu, "Gain and the threshold of three-dimensional quantum-box lasers," IEEE J. Quantum Electron. **QE-22**, 1915 (1986).

[7] Y. Miyamoto, M. Cao, Y. Shingai, K. Furuya, Y. Suematsue, K. G. Ravikumar, and S. Arai, "Light emission from quantum-box structure by current injection," J. Appl. Phys. **26**, L225 (1987).

[8] D. Leonard, M. Krishnamurthy, C. M. Reaves, S. P. Denbaars, and P. M. Petroff, "Direct formation of quantum-sized dots from uniform coherent islands of InGaAs on GaAs surfaces," Appl. Phys. Lett. **63**, 3203 (1993).

[9] S. Fafard, K. Hinzer, S. Raymond, M. Dion, J. McCaffrey, Y. Feng, and S. Charbonneau, "Red-emitting semiconductor quantum dot lasers," Science **274**, 1350 (1996).

[10] S. Fafard, "Quantum dots promise a new dimension for semiconductor lasers," Photonics Spectra **31** (May), 160 (1997).

[11] N. N. Ledentsov, V. M. Ustinov, V. A. Shchukin, P. S. Kop'ev, Zh. I. Alferov, and D. Bimberg, "Quantum dot heterostructures: fabrication, properties, lasers," Semiconductors **32**, 87 (1998).

[12] D. L. Huffaker, O. Baklenov, L. A. Graham, B. G. Streetman, and D. G. Deppe, "Quantum dot vertical-cavity surface-emitting laser with a dielectric aperture," Appl. Phys. Lett. **70**, 2356 (1997).

[13] R. Mirin, A. Gossard, and J. Bowers, "Room temperature lasing from InGaAs quantum dots," Electron. Lett. **32**, 1732 (1996).

[14] Q. Xie, A. Madhukar, P. Chen, and N. P. Kobayashi, "Vertical self-organized InAs quantum box islands on GaAs(100)," Phys. Rev. Lett. **75**, 2542 (1995).

[15] H. Shoji, K. Mukai, N. Ohtsuka, M. Sugawara, T. Uchida, and H. Ishikawa, "Lasing at three-dimensionally quantum-confined sublevel of self-organized $In_{0.5}Ga_{0.5}As$ quantum dots by current injection," IEEE Photonics Technol. Lett. **7** 1385 (1995).

[16] H. Shoji, Y. Nakata, K. Mukai, Y. Sugiyama, M. Sugawara, N. Yokoyama, and H. Ishikawa, "Self-formed InGaAs quantum dot lasers with multi-stacked dot layer," Jpn. J. Appl. Phys., Part 2, **35** L903 (1996).

[17] H. Saito, K. Nishi, I. Ogura, S. Sogou, and Y. Sugimoto, "Room-temperature lasing operation of a quantum-dot vertical-cavity surface-emitting laser," Appl. Phys. Lett. **69**, 3140 (1996).

[18] K. Kamath, P. Bhattacharya, T. Sosnowski, T. Norris, and J. Phillips, "Room-temperature operation on $In_{0.48}Ga_{0.52}As$/GaAs self-organised quantum dot lasers," Electron. Lett. **32**, 1374 (1996).

[19] K. Hinzer, S. Fafard, A. J. SpringThorpe, J. Arlett, E. M. Griswold, and Y. Feng, "Room temperature operation of AlInAs/AlGaAs quantum dot lasers," Physica E **2**, 729 (1998).

[20] M. Sugawara, ed. *Self-Assembled InGaAs/GaAs Quantum Dots* (Academic, San Diego, 1999).

[21] K. Hinzer, *Semiconductor Quantum Dot Lasers*, M.Sc. thesis (University of Ottawa, 1998).

[22] D. Bimberg, M. Grundmann, and N. N. Ledentsov, *Quantum Dot Heterostructures* (John Wiley & Sons, New York, 1998).

[23] R. Leon, P. M. Petroff, D. Leonard, and S. Fafard, "Spatially resolved visible luminescence of self-assembled semiconductor quantum dots," Science **267**, 1966 (1995).

[24] M. K. Zundel, N. Y. Jin-Phillipp, F. Phillip, K. Eberl, T. Riedl, E. Fehrenbacher, A. Hangleiter, "Red-light-emitting injection laser based on InP/GaInP self-assembled quantum dots," Appl. Phys. Lett. **73**, 1784 (1998).

[25] J. Phillips, P. Bhattacharya, and U. Venkateswaran, "Pressure-induced energy level crossings and narrowing of photoluminescence linewidth in self-assembled InAlAs/AlGaAs quantum dots," Appl. Phys. Lett. **74**, 1549 (1999).

[26] S. Anand, N. Carlsson, M.-E. Pistol, L. Samuelson, and W. Seifert, "Electrical characterization of InP/GaInP quantum dots by space-charge spectroscopy," J. Appl. Phys. **84**, 3747 (1998).

[27] S. Fafard, R. Leon, D. Leonard, J. L. Merz, and P. M. Petroff, "Visible photoluminescence from N-dot ensembles and the linewidth of ultrasmall $Al_yIn_{1-y}As/Al_xGa_{1-x}As$ quantum dots," Phys. Rev. B **50**, 8086 (1994).

[28] S. Raymond, S. Fafard, S. Charbonneau, R. Leon, D. Leonard, P. M. Petroff, and J. L. Merz, "Photocarrier recombination in $Al_yIn_{1-y}As/Al_xGa_{1-x}As$ self-assembled quantum dots," Phys. Rev. B **52**, 17238 (1995).

[29] S. Fafard, R. Leon, D. Leonard, J. L. Merz, and P. M. Petroff, "Phonons and radiative recombination in self-assembled quantum dots," Phys. Rev. B **52**, 5752 (1995).

[30] K. Mukai, N. Ohtsuka, H. Shoji, and M. Sugawara, "Emission from discrete levels in self-formed InGaAs/GaAs quantum dots by electric carrier injection: influence of phonon bottleneck," Appl. Phys. Lett. **68**, 3013 (1996).

[31] R. Leon, S. Fafard, P. G. Piva, S. Ruminov, Z. Liliental-Weber, "Tunable intersublevel transitions in self-forming semiconductor quantum dots," Phys. Rev. B **58**, R4262 (1998).

[32] G. Park, O. B. Shchekin, D. L. Huffaker, and D. G. Deppe, "Lasing from InGaAs/GaAs quantum dots with extended wavelength and well-defined harmonic-oscillator energy levels," Appl. Phys. Lett. **73**, 3351 (1998).

[33] Y. Sugiyama, Y. Nakata, T. Futatsugi, M. Sugawara, Y. Awano, and N. Yokoyama, "Narrow photoluminescence line width of closely stacked InAs self-assembled quantum dot structures," Jpn. J. Appl. Phys.. Part 2 **36**, L158 (1997).

[34] M. Grundmann, N. N. Ledentsov, O. Stier, D. Bimberg, V. M. Ustinov, P. S. Kop'ev, and Zh. I. Alferov, "Excited states in self-organized InAs/GaAs quantum dots: theory and experiments," Appl. Phys. Lett. **68**, 979 (1996).

[35] H. Lipsanen, M. Sopanen, and J. Ahopelto, "Luminescence from excited states in

strain-induced $In_xGa_{1-x}As$ quantum dots," Phys. Rev. B **51**, 13 868 (1995).

[36] S. Fafard, Z. R. Wasilewski, C. Ni. Allen, D. Picard, M. Spanner, J. P. McCaffrey, and P. G. Piva, "Manipulating the energy levels of semiconductor quantum dots," Phys. Rev. B **59**, 15368 (1999).

[37] J.-Y. Marzin, J. M. Gerard, A. Israel, D. Barrier, and G. Bastard, "Photoluminescence of single InAs quantum dots obtained by self-organized growth on GaAs," Phys. Rev. Lett. **73**, 716 (1994).

[38] A. Zrenner, L. V. Butov, M. Hagn, G. Abstreiter, G. Böhm, and G. Weimann, "Quantum dots formed by interface fluctuations in AlAs/GaAs coupled quantum well structures," Phys. Rev. Lett. **72**, 3382 (1994).

[39] M. Grundmann, J. Christen, N. N. Ledentsov, J. Böhrer, D. Bimberg, S. S. Ruvimov, P. Werner, U. Richter, U. Gösele, J. Heydenreich, V. M. Ustinov, A. Yu. Egorov, A. E. Zhukov, P. S. Kop'ev, and Zh. I. Alferov, "Ultranarrow luminescence lines from single quantum dots," Phys. Rev. Lett. **74**, 4043 (1995).

[40] D. Gammon, E. S. Snow, and D. S. Katzer, "Excited state spectroscopy of excitons in single quantum dots," Appl. Phys. Lett. **67**, 2391 (1995).

[41] A. Kuther, M. Bayer, A. Forchel, A. Gorbunov, V. B. Timoteev, F. Schäfer, and J. P. Reithmaier, "Zeeman splitting of excitons and biexcitons in single $In_{0.60}Ga_{0.40}As$/GaAs self-assembled quantum dots," Phys. Rev. B **58**, R7508 (1998).

[42] E. Dekel, D. Gershoni, E. Ehrenfreund, D. Spektor, J. M. Garcia, and P. M. Petroff, "Multiexciton spectroscopy of a single self-assembled quantum dot," Phys. Rev. Lett. **80**, 4991 (1998).

[43] F. Findeis, A. Zrenner, G. Böhm, G. Abstreiter, "Optical spectroscopy on a single InGaAs/GaAs quantum dot in the few-exciton limit," Solid State Commun. **114**, 227 (2000).

[44] M. Bayer, O. Stern, P. Hawrylak, S. Fafard, and A. Forchel, "Hidden symmetries in the energy levels of excitonic 'artificial atoms'," Nature **405**, 923 (2000).

[45] L. Landin, M.-E. Pistol, C. Pryor, M. Persson, L. Samuelson, and M. Miller, "Optical investigation of individual InAs quantum dots: Level splitting of exciton complexes," Phys. Rev. B **60**, 16640 (1999).

[46] Y. Toda, T. Sugimoto, M. Nishioka, and Y. Arakawa, "Near-field coherent excitation spectroscopy of InGaAs/GaAs self-assembled quantum dots," Appl. Phys. Lett. **76**, 3887 (2000).

[47] A. Gustafsson, M.-E. Pistol, L. Montelius, and L. Samuelson, "Local probe techniques for luminescence studies of low-dimensional semiconductor structures," J. Appl. Phys. **84**, 1715 (1998).

[48] S. Fafard, Z. R. Wasilewski, C. Ni. Allen, K. Hinzer, J. P. McCaffrey, Y. Feng, "Lasing in quantum dot ensemble with sharp adjustable electronic shells," Appl. Phys. Lett. **75**, 986 (1999).

[49] Z. R. Wasilewski, S. Fafard, and J. P. McCaffrey, "Size and shape engineering of vertically stacked self-assembled quantum dots," J. Crystal Gr. **201**, 1131 (1999).

[50] S. Fafard, M. Spanner, J. P. McCaffrey, Z. R. Wasilewski, "Coupled InAs/GaAs quantum dots with well-defined electronic shells," Appl. Phys. Lett. **76**, 2268 (2000).

[51] R. H. Blick, D. Pfannkuche, R. J. Haug, K. von Klitzing, K. Eberl, "Formation of a coherent mode in a double quantum dot," Phys. Rev. Lett. **80**, 4032 (1998).

[52] L. Kouwenhoven, "Coupled quantum dots as artificial molecules," Science **268**, 1440 (1995).

[53] T. Fujisawa, T. H. Oosterkamp, W. G. van der Wiel, B. W. Broer, R. Aguado, S. Tarucha, and L. P. Kouwenhoven, "Spontaneous emission spectrum in double quantum dot devices," Science **282**, 932 (1998).

[54] D. G. Austing, T. Honda, K. Muraki, Y. Tokura, and S. Tarucha, "Quantum dot molecules," Physica B **249**, 206 (1998).

[55] G. Schedelbeck, W. Wegschneider, M. Bichler, and G. Abstreiter, "Coupled quantum dots fabricated by cleaved edge overgrowth: from artificial molecules," Science **278**, 1792 (1997).

[56] R. J. Luyken, A. Lorken, M. Fricke, J. P. Kotthaus, G. Medeiros-Ribeiro, and P. M. Petroff, "Coulomb-coupling in vertically aligned self-assembled InAs quantum dots," Nanotechnology **10**, 14 (1999).

[57] Y. Tokura, D. G. Austing, and S. Tarucha, "Single-electron tunneling in two vertically coupled quantum dots," J. Phys.: Condens. Matter **11**, 6023 (1999).

[58] J. J. Palacios, and P. Hawrylak, "Correlated few-electron states in vertical double-quantum-dot systems," Phys. Rev. B **51**, 1769 (1995).

[59] C. Pryor, "Quantum wires formed from coupled InAs/GaAs strained quantum dots," Phys. Rev. Lett. **80**, 3579 (1998).

[60] L. R. C. Fonseca, J. L. Jimenez, and J. P. Leburton, "Electronic coupling in InAs/GaAs self-assembled stacked double-quantum-dot systems," Phys. Rev. B **58**, 9955 (1998).

[61] J. H. Davies, *The physics of low-dimensional semiconductors* (Cambridge University Press, Cambridge, 1997).

[62] S. Adachi, *GaAs and related materials: bulk semiconducting and superlattice properties* (World Scientific, Singapore, 1994).

[63] S. Adachi, *Physical properties of III-V semiconductor compounds: InP, InAs, GaAs, GaP, InGaAs, and InGaAsP* (John Wiley & Sons, New York, 1992).

[64] J. R. Chelikowski, and M. L. Cohen, "Nonlocal pseudopotential calculations for the electronic structure of eleven diamond and zinc-blende semiconductors," Phys. Rev. B **14**, 556 (1976).

[65] E. Hess, I. Topol, K.-R. Schulze, H. Neumann, and K. Unger, "Band structure and pseudopotential form factors for AlAs," Phys. Stat. Sol. B **55**, 187 (1973).

[66] K. Iga in *Handbook of Semiconductor Lasers and Photonic Integrated Circuits*, Y. Suematsu and A. R. Adams, eds, (Chapman and Hall, London, 1994).

[67] Y. P. Varshni, "Temperature dependence of the energy gap in semiconductors," Physica **34**, 149 (1967).

[68] Z. R. Wasilewski, M. M. Dion, D. J. Lockwood, P. Poole, R. W. Streater, and A. J. SpringThorpe, "Composition of AlGaAs," J. Appl. Phys. **81** 1683 (1997).

[69] S. Paul, J. B. Roy, and P. K. Basu, "Empirical expressions for the alloy composition and temperature dependence of the band gap and intrinsic carrier density in $Ga_xIn_{1-x}As$," J. Appl. Phys. **69**, 827 (1991).

[70] R. Nötzel, "Self-assembled growth of quantum-dot structures," Semicond. Sci. Technol. **11**, 1365 (1996).

[71] A.Wojs, P. Hawrylak, S. Fafard, and L. Jacak, "Electronic structure and magneto-optics of self-assembled quantum dots," Phys. Rev. B **54**, 5604 (1996).

[72] S. Raymond, *Zero-Dimensional Properties of Self-Assembled Islands*, Ph. D. thesis (University of Ottawa, 1997).

[73] U. Woggon, *Optical Properties of Semiconductor Quantum Dots* (Springer, Berlin, 1997).

[74] J. Singh, *Quantum Mechanics: Fundamentals and Applications to Technology*, (John Wiley and Sons, New York, 1996).

[75] M. Grundmann, O. Stier, and D. Bimberg, "InGaAs/GaAs pyramidal quantum dots: strain distribution, optical phonons, and electronic structure," Phys. Rev. B **52**, 11969 (1995).

[76] S. Fafard, E. Fortin, and A. P. Roth, "Sequential study of the component layers of a semiconductor quantum-well system," Can. J. Phys. **69**, 346 (1991).

[77] S. Fafard, S. Raymond, G. Wang, R. Leon, D. Leonard, S. Charbonneau, J. L. Merz, P. M. Petroff, and J. E. Bowers, "Temperature effects on the radiative recombination in self-assembled quantum dots," Surface Science **361/362**, 778 (1996).

[78] G. Bacher, H. Schweizer, J. Kovac, A. Forchel, H. Nickel, W. Schlapp, and R. Lösch, "Influence of barrier height on carrier dynamics in strained $In_xGa_{1-x}As/GaAs$ quantum wells," Phys. Rev. B **43**, 9312 (1991).

[79] G. Bastard, *Wave mechanics applied to semiconductor heterostructures*, (Les éditions de la physique, Paris, 1988).

[80] M. J. Kelly, *Low-Dimensional Semiconductors: Materials, Physics, Technology, Devices* (Oxford University Press, New York 1995).

[81] N. Peyghambarian, S. W. Koch, and A. Mysyrowicz, *Introduction to Semiconductor Optics* (Prentice Hall, Englewood Cliffs, New Jersey, 1993).

[82] K. Kash, "Optical properties of III-V semiconductor quantum wires and dots," J. Lumin. **46**, 69 (1990).

[83] P. D. Wang, C. M. Sotomayor Torres, H. Benisty, C. Weisbuch, and S. P. Beaumont, "Radiative recombination in GaAs-$Al_xGa_{1-x}As$ quantum dots," Appl. Phys. Lett. **61**, 946 (1992).

[84] C. M. Sotomayor Torres, W. E. Leicth, D. Lootens, P. D. Wang, G. M. Williams, S. Thoms, H. Wallace, P. Van Daele, A. G. Cullis, C. R. Stanley, P. Demeester, and S. P. Beaumont, "Wires and dots in GaAs-GaAlAs quantum wells: luminescence intensity studies," in *Nanostructures and Mesoscopic Systems* edited by W. P. Kirk, and M. A. Reed (Academic, San Diego, 1992).

[85] D. Heitmann, and J. P. Kotthaus, "The spectroscopy of quantum dot arrays," Physics Today **46**, #6 56 (1993).

[86] F. Daiminger, A. Schmidt, K. Peiger, F. Faller, and A. Forchel, "Thermalization and band renormalization in the zero-dimensional electron-hole system in InGaAs/GaAs

quantum dots," Semicond. Sci. Technol. **9**, 896 (1994).

[87] K. Brunner, U. Bockelmann, G. Abstreiter, M. Walther, G. Böhn, G. Tränkle, and G. Weimann, "Photoluminescence from a single GaAs/AlGaAs quantum dot," Phys. Rev. Lett. **69**, 3216 (1992).

[88] O. Klein, C. de C. Chamon, D. Tang, D. M. Abush-Magder, U. Meirav, X.-G. Wen, M. A. Kastner, and S. J. Wind, "Exchange effects in an artificial atom at high magnetic fields," Phys. Rev. Lett. **74**, 785 (1995).

[89] R. Leonelli, C. A. Tran, J. L. Brebner, J. T. Graham, R. Tabti, R. A. Masut, and S. Charbonneau, "Optical and structural properties of metalorganic-vapor-phase-epitaxy-grown InAs quantum wells and quantum dots in InP," Phys Rev B **48**, 11135 (1993).

[90] A. Hartmann, Y. Ducommun, E. Kapon, U. Hohenester, and E. Molinari, "Few-particle effects in semiconductor quantum dots: observation of multicharged excitons," Phys. Rev. Lett. **84**, 5648 (2000).

[91] V. I. Klimov, A. A. Mikhailovsky, Su Xu, A. Malko, J. A. Hollingsworth, C. A. Leatherdale, H.-J. Eisler, and M. G. Bawendi, "Optical gain and stimulated emission in nanocrystal quantum dots," Science 290, 314 (2000).

[92] D. Leonard, M. Krishnamurthy, S. Fafard, J. L. Merz, and P. M. Petroff. "Molecular-beam epitaxy growth of quantum dots from strained coherent uniform islands in InGaAs on GaAs," J. Vac. Sci. Technol. B **12**, 1063 (1994).

[93] D. Leonard, S. Fafard, K. Pond, Y. H. Zhang, J. L. Merz, and P. M. Petroff, "Structural and optical properties of self-assembled InGaAs quantum dots," J. Vac. Sci. Technol. B **12**, 2516 (1994).

[94] D. Leonard, K. Pond, and P. M. Petroff, "Critical layer thickness for self-assembled InAs islands on GaAs," Phys. Rev. B **50**, 11687 (1994).

[95] S. Fafard, Z. Wasilewski, J. McCaffrey, S. Raymond, and S. Charbonneau, "InAs self-assembled quantum dots on InP by molecular beam epitaxy," Appl. Phys. Lett. **68**, 991 (1996).

[96] H.-C. Ko, D.-C. Park, Y. Kawakami, S. Fujita and S. Fugita, "Self-organized CdSe quantum dots onto cleaved GaAs (110) originating from Stranski-Krastanow growth mode," Appl. Phys. Lett. **70**, 3278 (1997).

[97] D. J. Eaglesham, and M. Cerullo, "Dislocation-free Stranski-Krastanow growth of Ge on Si (100)," Phys. Rev. Lett. **64**, 1943 (1990).

[98] Y. Nakata, and Y. Sugiyama, in *Self-Assembled InGaAs/GaAs Quantum Dots*, edited by M. Sugawara (Academic, San Diego, 1999).

[99] F. C. Frank, and J. H. van der Merwe, "One-dimensional dislocations I. Static theory," Proc. R. Soc. London A **198**, 205 (1949).

[100] I. N. Stranski, and L. Krastanow, "Zur Theorie der orientierten Ausscheidung von Ionenkristallen aufeinander," Akad. Wiss. Wien Ber. Math. Naturwiss. Kl. **146**, 797 (1937).

[101] M. Volmer, and A. Weber, "Keimbildung in übersättigten Gebilden," Z. Phys. Chem. **119**, 277 (1926).

[102] I. V. Markov, *Crystal Growth for Beginners, Fundamentals of Nucleation, Crystal Growth and Epitaxy* (World Scientific, Singapore, 1995).

[103] S.-Z. Chang, T.-C. Chang, and S.-C. Li, "The growth of highly mismatched $In_xGa_{1-x}As$ ($0.28 \leq z \leq 1$) on GaAs by molecular-beam epitaxy," J. Appl. Phys. **73**, 4916 (1993).

[104] R. Leon, C. Lobo, A. Clark, R. Bozek, A. Wysmolek, A. Kurpiewski, and M. Kaminska, "Different paths to tunability in III-V quantum dots," J. Appl. Phys. **84**, 248 (1998).

[105] R. Leon, and S. Fafard, "Structural and radiative evolution in quantum dots near the $In_xGa_{1-x}As$/GaAs Stranski-Krastanow transformation," Phys. Rev. B **58**, R1726 (1998).

[106] B. J. Riel, K. Hinzer, S. Moisa, J. Fraser, K. St-Jean, P. Piercy, S. Fafard, and Z. R. Wasilewski, "Tuning self-assembled quantum dots using the arsenic pressure," *submitted 2001*.

[107] P. B. Joyce, T. J. Krzyzewski, G. R. Bell, T. S. Jones, S. Malik, D. Childs, and R. Murray, "Effect of growth rate on the size, composition, and optical properties of InAs/GaAs quantum dots grown by molecular beam epitaxy," Phys. Rev. B **62**, 10891 (2000).

[108] S. Raymond, S. Fafard, P. J. Poole, A. Wojs, P. Hawrylak, C. Gould, A. Sachrajda, S. Charbonneau, D. Leonard, R. Leon, P. M. Petroff, and J. L. Merz, "State-filling and magneto-photoluminescence of excited states in InGaAs/GaAs self-assembled quantum dots," Superlattices Microstruct. **21**, 541 (1997).

[109] S. Raymond, X. Guo, J. L. Merz, and S. Fafard, "Excited-state radiative lifetime in self-assembled quantum dots obtained from state-filling spectroscopy," Phys. Rev. B **59**, 7624 (1999).

[110] D. Morris, N. Perret, and S. Fafard, "Carrier energy relaxation by means of Auger processes in InAs/GaAs self-assembled quantum dots," Appl. Phys. Lett. **75**, 3593 (1999).

[111] S. Marcinkevičius, and R. Leon, "Photoexcited carrier transfer in InGaAs quantum dot structures: Dependence on the dot density," Appl. Phys. Lett. **76**, 2406 (2000).

[112] A. Pimpinelli, and J. Villain, *Physics of Crystal Growth* (Cambridge University, Cambridge, 1998)

[113] R. Steffen, Th. Koch, J. Oshinowo, F. Faller, and A. Forchel, "Photoluminescence study of deep etched InGaAs/GaAs quantum wires and dots by low-voltage electron beam lithography," Appl. Phys. Lett. **68**, 223 (1996).

[114] A. Forchel, H. Leier, B. E. Maile, and R. Germann, "Fabrication and optical spectroscopy of ultra small III-V compound semiconductor structures," Festkörperprobleme **28**, 99 (1988).

[115] M. Bayer, T. Gutbrod, A. Forchel, V. D. Kulakovskii, A. Garbunov, M. Michel, R. Steffen, and K. H. Wang, "Exciton complexes in $In_xGa_{1-x}As$/GaAs quantum dots," Phys. Rev. B **58**, 4740 (1998).

[116] See P. W. M. Blom, P. J. van Hall, C. Smit, J. P. Cuypers, and J. H. Wolter, "Selective exciton formation in thin GaAs/$Al_xGa_{1-x}As$ quantum wells," Phys. Rev. Lett. 71, 3878 (1993), and references therein.

[117] M. Young, *Optics and Lasers: Including Fibers and Optical Waveguides* (Springer, Berlin, 2000).

[118] P. Edelman, W. Henley, and J. Lagowski, "Photoluminescence and minority carrier diffusion length imaging in silicon and GaAs," Semicond. Sci. Technol. **7**, A22 (1992).

[119] H. D. Robinson, and B. B. Goldberg, "Light-induced spectral diffusion in single self-assembled quantum dots," Phys. Rev. B **61**, R5086 (2000).

[120] A. Gustafsson, M.-E. Pistol, L. Montellius, and L. Samuelson, "Local probe technique for luminescence studies of low dimensional semiconductor structures," Appl. Phys. Lett. **84**, 1715 (1998).

[121] P. G. Piva, S. Fafard, M. Dion, M. Buchanan, S. Charbonneau, R. D. Goldberg, and I. V. Mitchell, "Reduction of InGaAs/GaAs laser facet temperatures by band gap shifted extended cavities," Appl. Phys. Lett. **70**, 1662 (1997).

[122] M. Asada in *Handbook of Semiconductor Lasers and Photonic Integrated Circuits*, edited by Y. Suematsu and A. R. Adams (Chapman and Hall, London, 1994) Chap. 7.

[123] H. Kawanishi in *Handbook of Semiconductor Lasers and Photonic Integrated Circuits*, edited by Y. Suematsu and A. R. Adams (Chapman and Hall, London, 1994) Chap. 10, p. 334.

[124] S. Fafard, K. Hinzer, A. J. SpringThorpe, Y. Feng, J. McCaffrey, S. Charbonneau, and E. M. Griswold, "Temperature effects in semiconductor quantum dot lasers," Mat. Science and Eng. B **51**, 114 (1998).

[125] G. J. Davies, T. Kerr, C. G. Tuppen, B. Wakefield, and D.A. Andrews, "The growth and characterization of nominally undoped $Al_{1-x}In_xAs$ grown by molecular beam epitaxy," J. Vac. Sci. Technol. **B 2**, 219-223 (1984).

[126] In *Numerical Data and Functional Relationships in Science and Technology*, Landolt-Börnstein Series, edited by O. Mandelung and H. Schulz, Vol. 22 (Springer, Berlin, 1987).

[127] J. Brübach, A. Yu. Silov, J. E. M. Haverkort, W. v. d. Vleuten, and J. H. Wolter, "Coupling of ultrathin InAs layers as a tool for band-offset determination," Phys. Rev. B **59**, 10 315 (1999).

[128] S. H. Pan, H. Shen, Z. Hang, F. H. Pollack, W. Zhuang, Q. Xu, A. P. Roth, R. A. Masut, C. Lacelle, and D. Morris, "Photoreflectance study of narrow-well strained-layer $In_xGa_{1-x}As$/GaAs coupled multiple-quantum-well structures," Phys. Rev B **38**, 3375 (1988).

[129] J. Y. Marzin, M. N. Charasse, B. Sermage, "Optical investigation of a new type of valence-band configuration in $In_xGa_{1-x}As$-GaAs strained superlattices," Phys. Rev. B **31**, 8298 (1985).

[130] O. J. Glembocki, and K. Takarabe in *Handbook of optical constants of solids II*, E.D. Palik ed. (Academic Press, Boston, 1991).

[131] R. Leon, S. Fafard, D. Leonard, J. L. Merz, and P. M. Petroff, "Visible luminescence from semiconductor quantum dots in large ensembles," Appl. Phys. Lett. **67**, 521 (1995).

[132] H. Kogelnik, in *Guided-Wave Optoelectronics*, edited by T. Tamir (Springer, Heidelberg, 1990).

[133] K. Gamo, T. Tanbun-Ek, and K. G. Ravikumar in *Handbook of Semiconductor Lasers and Photonic Integrated Circuits*, edited by Y. Suematsu and A. R. Adams (Chapman and Hall, London, 1994) Chap. 15, p. 493.

[134] H. Kawanishi in *Handbook of Semiconductor Lasers and Photonic Integrated Circuits*, edited by Y. Suematsu and A. R. Adams (Chapman and Hall, London, 1994)

Chap. 10, p. 334.

[135] S. Fafard, Z. R. Wasilewski, and M. Spanner, "Evolution of the energy levels in quantum dot ensembles with different densities," Appl. Phys. Lett. **75**, 1866 (1999).

[136] G. H. B. Thompson, *Physics of semiconductor Laser Devices* (Wiley, Chichester, 1980).

[137] N. Kirstaedter, O. G. Schmidt, N. N. Ledentsov, D. Bimberg, V. M. Ustinov, A. Yu. Egorov, A. E. Zhukov, M. V. Maximov, P. S. Kop'ev, Zh. I. Alferov, "Gain and differential gain of single layer InAs/GaAs quantum dot injection lasers," Appl. Phys. Lett. **69**, 1226 (1996).

[138] Q. Xie, A. Kalburge, P. Chen, and A. Madhukar, "Observation of lasing from vertically self-organized InAs three dimensional island quantum boxes on GaAs (001)," IEEE Photonics Technol. Lett. **8**, 965 (1996).

[139] Z. Zou, O. B. Shchekin, G. Park, D. L. Huffaker, and D. G. Deppe, "Threshold temperature dependence of lateral-cavity quantum-dot lasers," IEEE Photonics Technol. Lett. **10** 1673 (1998).

[140] A. E. Zhukov, V. M. Ustinov, A. Yu. Egorov, A. R. Kovsh, A. F. Tsatsul'nikov, M. V. Maximov, N. N. Ledentsov, S. V. Zaitsev, N. Yu. Gordeev, P. S. Kopev,and Zh. I. Alferov, "Negative characteristic temperature in InGaAs quantum dot injection laser," Jpn. J. Appl. Phys. **36**, 4216 (1997).

[141] C. Lobo, R. Leon, S. Marcinkevičius, W. Yang, P. C. Sercel, X. Y. Liao, J. Zou, and D. J. H. Cockayne, "Inhibited carrier transfer in ensembles of isolated quantum dots," Phys. Rev. **B** 60, 16 647 (1999).

[142] Optics Reference in Newport Instruments Optics 1997-1998 catalog, p. 12-11.

[143] In *Handbook of Optical Constants of Solids II*, edited by E. D. Palik (Academic, 1991).

[144] S. Perkowiz, *Optical Characterization of Semiconductors: Infrared, Raman, and Photoluminescence Spectroscopy* (Academic, London, 1993).

[145] S. Fafard, "Near-surface InAs/GaAs quantum dots with sharp electronic shells," Appl. Phys. Lett. **76**, 2707 (2000).

[146] D. D. Pollock, *Physics of Engineering Materials* (Prentice Hall, Englewood Cliffs, 1990).

[147] H. A. Zarem, P. C. Sercel, J. A. Lebens, L. E. Eng, A. Yariv, and K. J. Vahala, "Direct

determination of the ambipolar diffusion length in GaAs/AlGaAs heterostructures by cathodoluminescence," Appl. Phys. Lett. **55**, 1647 (1999).

[148] K. Kishino, and S. Arai in *Handbook of Semiconductor Lasers and Photonic Integrated Circuits*, edited by Y. Suematsu and A. R. Adams (Chapman and Hall, London, 1994) Chap. 11, p. 374.

[149] H. Shoji, Y. Nakata, K. Mukai, Y. Sugiyawa, M. Sugawara, N. Yokoyama, and H. Ishikawa, "Temperature dependent lasing characteristics of multi-stacked quantum dot lasers," Appl. Phys. Lett. **71**, 193 (1997).

[150] L. Harris, D. J. Mowbray, M. S. Skolnick, M. Hopkinson, and G. Hill, "Emission spectra and mode structure of InAs/GaAs self-organized quantum dot lasers," Appl. Phys. Lett. **73**, 969 (1998).

[151] S. V. Zaitsev, N. Yu. Gordeev, V. M. Ustinov, A. E. Zhokov, A. Yu. Egorov, M. V. Maksimov, A. F. Tsatsul'nikov, N. N. Ledentsov, P. S. Kop'ev, Zh. I. Alferov, and D. Bimberg, "The properties of low-threshold heterolasers with clusters of quantum dots," Semiconductors **31**, 455 (1997).

[152] L. V. Asryan, and R. A. Suris, "Spatial hole burning and multimode generation threshold in quantum-dot lasers," Appl. Phys. Lett. **74**, 1215 (1999).

[153] H. Jiang, and J. Singh, " Nonequilibrium distribution in quantum dot lasers and influence on laser spectral output," J. Appl. Phys. **85**, 7438 (1999).

[154] Y. L. Chang, I. H. Tan, Y. H. Zhang, D. Bimberg, J. L. Merz, and E. Hu, "Reduced quantum efficiency of a near-surface quantum well," J. Appl. Phys. **74**, 5144 (1993).

[155] L. Jacak, P. Hawrylak, and A. Wojs, *Quantum dots* (Springer Verlag, Berlin, 1998)

[156] P. Hawrylak, "Excitonic artificial atoms: Engineering optical properties of quantum dots," Phys. Rev. B **60**, 5597 (1999).

[157] A. Wojs, and P. Hawrylak, "Exciton-exciton interactions in highly excited quantum dots in a magnetic field," Solid State Commun. **100**, 2487 (1996).

[158] O. Stier, M. Grundmann, and D. Bimberg, "Electronic and optical properties of strained quantum dots modeled by 8-band k.p theory," Phys. Rev. B **59**, 5688 (1999).

[159] H. Jiang, and J. Singh, "Conduction band spectra in self-assembled InAs/GaAs dots: a comparaison of effective mass and an eight-band approach," Appl. Phys. Lett. **71**, 3239 (1997).

[160] L. W. Wang, A. J. Williamson, A. Zunger, H. Jiang, and J. Singh, "Comparison of the

k.p and direct diagonalization approaches to the electronic structure of InAs/GaAs quantum dots," Appl. Phys. Lett. **76**, 339 (2000).

[161] K. Hinzer, P. Hawrylak, M. Korkusinski, S. Fafard, M. Bayer, O. Stern, A. Gorbunov, and A. Forchel, "Optical Spectroscopy of a single AlInAs/AlGaAs quantum dot", Phys. Rev. B **63**, 075314 (2001).

[162] P. D. Wang, J. L. Merz, S. Fafard, R. Leon, D. Leonard, G. Medeiros-Ribeiro, M. Oestreich, P. M. Petroff, K. Uchida, N. Miura, H. Akiyama, and H. Sakaki, "Magnetoluminescence studies of $In_yAl_{1-y}As$ self-assembled quantum dots in $Al_xGa_{1-x}As$ matrices," Phys. Rev. B **53**, 16458 (1996).

[163] S. N. Walck and T. L. Reinecke, "Exciton diamagnetic shift in semiconductor nanostructures," Phys. Rev. B **57**, 9088 (1998).

[164] M. Bayer, A. Kuther, A. Forchel, A.A. Gorbunov, V. B. Timofeev, F.Schafer, j. P. Reithmaier, T. L. Reneicke, and S. N. Walck, "Electron and hole g-factors and exchange interaction from studies of the exciton fine structure in $In_{0.60}Ga_{0.40}As$ quantum dots," Phys. Rev. Lett. **82**, 1748 (1999).

[165] K. H. Schmidt, G. Medeiros-Ribeiro, J. Garcia, and P. M. Petroff, " Size quantization effects in InAs self-assembled quantum dots," Appl. Phys. Lett. **71**, 2014 (1997).

[166] J. L. Spithoven, J. Lorbacher, I. Manke, F. Heinrichsdorff, A. Krost, D. Bimberg, and M. Dähne-Prietsch, "Finite linewidth observed in photoluminescence spectra of individual $In_{0.4}Ga_{0.6}As$ quantum dots," J. Vac. Sci. Technol. B **17**, 1632 (1999).

[167] K. Matsuda, T. Saiki, H. Saito, and K. Nishi, "Room–temperature photoluminescence spectroscopy of self- assembled InGaAs single quantum dots by using highly sensitive near-field scanning optical microscope," Appl. Phys. Lett. **76**, 73 (2000).

[168] S. Fafard, and C. Ni. Allen, "Intermixing in quantum-dot ensembles with sharp adjustable shells," Appl. Phys. Lett. **75**, 2374 (1999).

[169] A. Zrenner, M. Markmann, E. Beham, F. Findeis, G. Böhm, and G. Abstreiter, " Spatially resolved spectroscopy on single self-assembled quantum dots," J. Electron. Mat. **28**, 542 (1999).

[170] C. H. Bennett, "Quantum information and computation," Phys. Today, **48** (no. 10), 24 (1995).

[171] D. P. DiVincenzo, "Quantum computation," Science **270**, 255 (1995).

[172] D. Loss, and D. P. DiVincenzo, "Quantum computation with quantum dots," Phys.

Rev. A **57**, 120 (1998).

[173] A. Steane, "Quantum Computing," Rep. Prog. Phys. **61**, 117 (1998).

[174] A. Barenco, D. Deutsch, A. Ekert, and R. Jozsa, "Conditional quantum dynamics and logic gates," Phys. Rev. Lett. **74**, 4083 (1995).

[175] J. A. Brum, and P. Hawrylak, "Coupled quantum dots as quantum exclusive-OR gate," Superlattices Microstruct. **22**, 431 (1997).

[176] P. Zanardi, and F. Rossi, "Quantum information in semiconductors: noiseless encoding in a semiconductor array," Phys. Rev. Lett. **81**, 4752 (1998).

[177] S. Fafard, E. M. Griswold et al. *unpublished.*

[178] P. Harrison, *Quantum Wells, Wires and Dots: Theoretical and Computational Physics* (John Wiley & Sons, Chichester, 2000).

[179] K. Hinzer, M. Bayer, J. P. McCaffrey, P. Hawrylak, M. Korkusinski, O. Stern, Z. R. Wasilewski, S. Fafard, and A. Forchel, "Optical spectroscopy of electronic etates in a single pair of vertically coupled self-assembled quantum dots," Phys. Status Sol. (b) **224**, 385 (2001).

[180] M. Korkusinski, and P. Hawrylak, "Electronic structure of vertically stacked self-assembled quantum disks," Phys. Rev. B **63**, 195311 (2001).

[181] P. Hawrylak, S. Fafard, and Z. R. Wasilewski, "Engineering quantum states in self-assembled quantum dots for quantum information processing," Cond. Mat. News **7**, 16 (1999).

[182] J. Preskill, *Lecture Notes for Physics 229: Quantum Information and Computation*, (California Institute of Technology, California, 1998).

[183] M. Bayer, P. Hawrylak, K. Hinzer, S. Fafard, M. Korkusinski, Z. R. Wasilewski, O. Stern, and A. Forchel, "Coupling and entangling of quantum states in quantum dot molecules," Science **297**, 451 (2001).

[184] H.-W. Ren, S. V. Nair, J.-S. Lee, S. Sugou, and Y. Matsumoto, "Photoluminescence of strain-induced coupled InGaAs/GaAs quantum-dot pairs," J. Electron. Materials **29**, 520 (2000).

[185] P. M. Petroff, A. Lorke, and A. Imamoglu, "Epitaxially self-assembled quantum dots," Physics Today **54** (no. 5), 46 (2001).

[186] R. J. Warburton, C. Schaflein, D. Haft, F. Bickel, A. Lorke, K. Karrai, J. M. Garcia, W. Schoenfeld, and P. M. Petroff, "Optical emission from a charge-tunable quantum ring," Nature, **405**, 926 (2000).

[187] F. Findeis, M. Baier, A. Zrenner, M. Bichler, G. Abstreiter, U. Hohenester, and E. Molinari, "Optical excitations of a self-assembled artificial ion," Phys. Rev. B **63**, 121309 (2001).

[188] Y. Hardy, "Tunable lasers hit the right note for DWDM," Photonics Spectra, September, 133 (2000).

[189] D. Mehuys, M. Mittelstein, A. Yariv, R. Sarfaty, and J. E. Ungar, "Optimised Fabry-Perot (AlGa)As quantum-well lasers tunable over 105 nm," Electronics Lett. **25**, 143 (1989).

[190] H. Tabuchi, and H. Ishikawa, "External grating tunable MQW laser with wide tuning range of 240 nm," Electronics Lett. **26**, 742 (1990).

[191] E. Kapon, S. Simhony, R. Bhat, and D. M. Hwang, "Single quantum wire semiconductor lasers," Appl. Phys. Lett. **55**, 2715 (1989).

[192] R. L. Williams, G. C. Aers, P. J. Poole, D. Chithrani, and B. Lamontagne, "Controlling the self-assembly of InAs/InP quantum dots," J. Crystal Gr. **223**, 321 (2001).